

# Incremental nonlinear flight control synthesis for a flexible and high aspect ratio aircraft

T.J. Plasmeijer

Master of Science Thesis





# **Incremental nonlinear flight control synthesis for a flexible and high aspect ratio aircraft**

MASTER OF SCIENCE THESIS

For the degree of Master of Science in Systems and Control at Delft  
University of Technology

T.J. Plasmeijer

July 8, 2021

Faculty of Mechanical, Maritime and Materials Engineering (3mE) · Delft University of  
Technology



The work in this thesis was supported by Netherlands Aerospace Centre (NLR). Their cooperation is hereby gratefully acknowledged.



Copyright © Delft Center for Systems and Control (DCSC)  
All rights reserved.



---

# Abstract

Aircraft efficiency has over the last decades increasingly improved by a large-scale usage of lightweight composite materials in high aspect ratio airframes. A tedious property of this advancement is that the increased structural flexibility produces unfavourable interactions between aerodynamics and structural dynamics. Existing literature has already shown the advantages of active feedback control to alleviate these adverse coupling effects. However, limited attention has been paid to the practical implementation of these flight control systems. This thesis, therefore, presents a robust control synthesis method for obtaining a real-time implementable flight control system for a high aspect ratio and flexible aircraft.

The presented controller synthesis method combines techniques from Incremental Nonlinear Dynamic Inversion (INDI) with linear  $\mathcal{H}_\infty$ -norm minimization to achieve simultaneous reference tracking performance and structural motion alleviation. With focusing on acquiring a real-time implementable flight controller, this work emphasizes the importance of taking hardware events such as sensor noise and time delays into account. The goal of this thesis is, therefore, threefold. Firstly, the limitation of INDI control regarding its applicability to flexible aircraft is addressed. Secondly, the INDI- $\mathcal{H}_\infty$  synthesis formulation is derived and verified using simulations performed on a full-scale SB-10 glider model. Thirdly, the INDI controller is implemented on a real 1:3 scaled Diana-2 demonstrator to compare it against a similarly tuned PID controller in flight. Tracking accuracy and structural motion alleviation are tested on a doublet reference signal for pitch angle. The simulations show that the INDI- $\mathcal{H}_\infty$  controller outperforms the conventional INDI both in responsiveness and robustness performance. While not affecting tracking accuracy, the INDI- $\mathcal{H}_\infty$  controller can reduce the oscillations in pitch angle by 6.4% and the elevator control input by 5.9%. Furthermore, the INDI controller's real-time capability is verified in a developed hardware-in-the-loop simulation and validated through conducted ground tests.



---

# Table of Contents

<b>Acknowledgements</b>	<b>xiii</b>
<b>1 Introduction</b>	<b>1</b>
1-1 Motivation and problem formulation . . . . .	1
1-2 Related work . . . . .	3
1-3 Research objective . . . . .	4
1-4 Challenges and thesis contributions . . . . .	5
1-5 Outline of this thesis . . . . .	6
<b>2 Incremental NDI and <math>\mathcal{H}_\infty</math> control synthesis theory</b>	<b>7</b>
2-1 Nonlinear Dynamic Inversion . . . . .	7
2-2 Incremental Nonlinear Dynamic Inversion . . . . .	9
2-2-1 Time scale separation principle . . . . .	10
2-2-2 Pseudo Control Hedging . . . . .	10
2-2-3 Similar PID controller . . . . .	11
2-3 $\mathcal{H}_\infty$ control synthesis . . . . .	12
2-3-1 General $\mathcal{H}_\infty$ optimization . . . . .	12
2-3-2 Mixed sensitivity . . . . .	13
2-4 Quantitative assessment criteria . . . . .	14
2-4-1 Control performance metric . . . . .	14
2-4-2 Control robustness metrics . . . . .	15
<b>3 Aeroservoelastic modelling of a fixed-wing aircraft</b>	<b>17</b>
3-1 Assumptions and reference frames . . . . .	17
3-2 Aeroservoelastic model . . . . .	19
3-2-1 Equations of motion . . . . .	20
3-2-2 Aerodynamical forces and moments . . . . .	20

3-2-3	Virtual sensor modelling . . . . .	23
3-3	Actuator modelling . . . . .	23
3-3-1	Available control surfaces . . . . .	24
3-3-2	Actuator identification . . . . .	25
3-4	Aerodynamic damping . . . . .	26
3-5	Conclusive remarks . . . . .	27
<b>4</b>	<b>Incremental NDI and <math>\mathcal{H}_\infty</math> control synthesis for aeroservoelastic aircraft</b>	<b>29</b>
4-1	Incremental Nonlinear Dynamic Inversion control . . . . .	29
4-1-1	INDI angular rate controller . . . . .	30
4-1-2	Incremental time delays . . . . .	32
4-1-3	System dynamics increment compensation . . . . .	33
4-1-4	Incremental Control Allocation . . . . .	34
4-1-5	Intermediate conclusions . . . . .	37
4-2	Symmetric wing bending alleviation using $\mathcal{H}_\infty$ synthesis . . . . .	38
4-2-1	Synthesis model . . . . .	39
4-2-2	Mixed sensitivity framework with INDI . . . . .	41
4-2-3	Synthesis with Pseudo Control Hedging . . . . .	45
4-2-4	Scheduled structural motion alleviation controller . . . . .	46
4-2-5	Intermediate conclusions . . . . .	47
4-3	Attitude control . . . . .	48
4-3-1	Direct side-slip control . . . . .	48
4-3-2	Indirect side-slip control . . . . .	49
4-4	Conclusive remarks . . . . .	49
<b>5</b>	<b>Simulation and implementation results</b>	<b>51</b>
5-1	Simulation results . . . . .	51
5-1-1	Baseline control design . . . . .	51
5-1-2	Controller performance comparison . . . . .	52
5-1-3	Controller robustness comparison . . . . .	55
5-2	Implementation results . . . . .	57
5-2-1	Available hardware platform of the Diana-2 demonstrator . . . . .	57
5-2-2	Hardware-in-the-loop simulation . . . . .	58
5-2-3	Ground test experiments . . . . .	60
5-3	Discussion . . . . .	60
<b>6</b>	<b>Conclusions and recommendations</b>	<b>63</b>
6-1	Conclusions . . . . .	63
6-2	Recommendations . . . . .	64

---

<b>A</b>	<b>Aeroservoelastic model</b>	<b>67</b>
A-1	The SB-10 and Diana-2 glider model . . . . .	67
A-2	Linearization algorithm . . . . .	68
A-2-1	Jacobian linearization . . . . .	68
A-2-2	Trim point algorithm . . . . .	69
<b>B</b>	<b><math>\mathcal{H}_\infty</math> algorithm and control design formulation with INDI-PCH</b>	<b>71</b>
B-1	General $\mathcal{H}_\infty$ algorithm . . . . .	71
B-2	Synthesis formulation for the INDI-PCH controller . . . . .	72
<b>C</b>	<b>Simulated tracking and structural motion alleviation results</b>	<b>75</b>
<b>D</b>	<b>Actuator dynamics and time delay identification</b>	<b>77</b>
D-0-1	Actuator identification . . . . .	77
D-0-2	Time delay identification . . . . .	78
	<b>Bibliography</b>	<b>81</b>
	<b>Glossary</b>	<b>85</b>
	List of Acronyms . . . . .	85



---

# List of Figures

1-1	Sufficient frequency separation for classical control in the left figure. Frequency overlap in aeroservoelastic control in the right figure [1] . . . . .	2
2-1	Generalized interconnection for $\mathcal{H}_\infty$ control synthesis . . . . .	12
3-1	Inertial and body reference frame of an undeformed or rigid glider [2] . . . . .	19
3-2	Mean axes reference frame of a deformed glider [2] . . . . .	19
3-3	The first three symmetric wing bending modes of the full scale SB-10 glider . . . . .	21
3-4	The two asymmetric structural modes of the full scale SB-10 glider . . . . .	21
3-5	Available control surfaces deflections for both the Diana2 and SB-10 glider . . . . .	24
3-6	Open loop rigid poles (in blue) and structural poles (in red) of multiple linear systems, trimmed at 5 horizontal steady flight conditions between 20 m/s and 40 m/s . . . . .	26
3-7	Change in natural frequency and damping of the first two structural modes and the rigid body short period at different flying velocities . . . . .	27
4-1	The resulting INDI control scheme including actuator dynamics $A(s)$ , a discrete-time equivalent of the filter (4-8) denoted by $H(z)$ and a discrete time finite difference operator $D(z)$ . . . . .	31
4-2	Simulated pitch rate response of (4-9) on the left, and corresponding elevator input on the right. Here, the ideal response is indicated in blue and the nominal response in red . . . . .	31
4-3	Doublet response of the angular rates in Figure 4-3a with corresponding rigid-body and structural dynamics increments in Figure 4-3b. The nominal and ideal case are described in Table 4-1 . . . . .	33
4-4	The incremental control allocation method compared against the nominal INDI control case for a time delay with $n = 5$ . . . . .	35
4-5	The Adaptive Incremental Control Allocation (AICA) method compared against previously discussed ICA and the nominal INDI controller with a time delay of $n = 5$ . . . . .	36

4-6	Overall pitch rate control structure with INDI angular rate control and linear $\mathcal{H}_\infty$ control . . . . .	38
4-7	INDI control scheme with a discrete-time finite difference approximation, second order washout filter, actuator model and a proportional linear control gain $K_p$ . . . . .	40
4-8	INDI control scheme in which the continuous time transfer functions are separated from the discrete time functions using samplers . . . . .	40
4-9	Stability margins for various sampling times, proportional gains and actuator bandwidths when subjected to different incremental time delays . . . . .	41
4-10	Generalized interconnection for synthesising the linear controller $K$ in the INDI control scheme using a mixed sensitivity $\mathcal{H}_\infty$ -norm minimization. The blue, green and red dots indicate the process, transport and measurement delay respectively. . . . .	42
4-11	Frequency response of the weighted output function $W_u(z)$ on the left and the closed loop pitch rate response on the right . . . . .	45
4-12	Doublet response of $q$ for both the INDI and INDI- $\mathcal{H}_\infty$ controller in the left figure and corresponding control surfaces deflections in the right figure . . . . .	45
4-13	Generalized interconnection for synthesising the linear controller $K(z)$ with the INDI-PCH control included using a mixed sensitivity $\mathcal{H}_\infty$ -norm minimization. Similar as in 4-10 the blue, green and red dots indicate the process, transport and measurement delay respectively. . . . .	46
4-14	The overall control architecture with PCH, INDI and the augmented $\mathcal{H}_\infty$ controller for tracking references of pitch and roll angles. Here, $R(z)$ denotes the discrete-time integrator . . . . .	50
5-1	The baseline control architecture with the kinematic nonlinear inversion controller in the outer-loop and baseline PID controller in the inner-loop . . . . .	52
5-2	Pitch rate and pitch angle responses of the INDI controller and the baseline PID controller for the nominal simulation condition described in Table 4-1 . . . . .	52
5-3	The left figure shows the simulations for a grid of inner and outer loop control gains that is evaluated by the integrated pitch angle error and the elevator deflection. The right figure displays the pitch angle and elevator response of the selected design point. Here, the shaded represents the integrated pitch angle error and elevator deflection. . . . .	53
5-4	Vertical wingtip velocity on the left with corresponding strain measurements at the wing root at the right. Note that these responses correspond to the same disturbance conditions as in Table 5-2. . . . .	54
5-5	The reference signal of pitch angle in blue, with upper and lower stability limits marked in red, used in TDM simulations . . . . .	55
5-6	Robustness comparison between the INDI controller and the INDI- $\mathcal{H}_\infty$ controller for various parametric uncertainty configurations of the structural dynamics. . . . .	57
5-7	Data flow through the different available hardware component on the Diana-2 demonstrator . . . . .	58
5-8	Developed hardware-in-the-loop simulation in which the the simulation on the computer runs at 200 Hz, the visualization receives data at 20 Hz, the controller on the Pixhawk runs at 100 Hz and the simulation receives the PWM signals at around 70 Hz. . . . .	59
5-9	HIL setup for the Diana-2 demonstrator. . . . .	59
5-10	Simulated and measured roll rate response in the left figure with corresponding PWM outputs in the right figure. The used true airspeed in simulation is set to the mean of the measured ground speed plus an estimate of the wind speed. This resulted in a value of 5.65 m/s. . . . .	60

---

B-1	Generalized interconnection for synthesising the linear controller $K$ , for the INDI-PCH control structure, using a mixed sensitivity $\mathcal{H}_\infty$ -norm minimization . . . . .	72
C-1	Pitch angle response with corresponding control surface deflections of the INDI and INDI- $\mathcal{H}_\infty$ controller. . . . .	75
C-2	Structural motion response, depicted by the first and second modal velocities, of the INDI and INDI- $\mathcal{H}_\infty$ controller . . . . .	75
C-3	Pitch angle response with corresponding control surface deflections of the baseline PID controller. . . . .	76
C-4	Structural motion response, depicted by the first and second modal velocities, of the baseline PID controller . . . . .	76
D-1	The resulting fit of the identified second-order actuator model for the left outer aileron. Here, the measured control surface deflection is indicated in blue while the modelled response is marked in red. . . . .	77
D-2	Process delay test using the HIL simulation. Blue line is the signal out, red line is the echoed signal from the Pixhawk . . . . .	79



---

## List of Tables

3-1	Identified second order actuator model parameters of all 8 control surfaces installed on the Diana-2 demonstrator . . . . .	25
4-1	The simulation conditions for the ideal and nominal case of the INDI angular rate controller . . . . .	31
5-1	The three different time delay configurations that are used for evaluating control performance and control robustness . . . . .	53
5-2	Comparison table between the PID, INDI and INDI- $\mathcal{H}_\infty$ controllers. The controllers are simulated with the same NDI outer-loop and a worst-case time delay configuration at 40 m/s . . . . .	54
5-3	Computed TDM of the PID, INDI-ICA, INDI and INDI- $\mathcal{H}_\infty$ controllers for different time delay configurations at an operating condition with 40 m/s. . . . .	56
A-1	Basic aircraft parameters of the full-scale SB-10 and the 1:3 scaled Diana-2 demonstrator . . . . .	67
A-2	Undamped natural frequencies of the structural dynamics for both the full scale SB-10 and 1:3 scaled Diana-2 demonstrator . . . . .	68
D-1	Identified second-order actuator dynamics of the control surfaces installed on the Diana-2 demonstrator . . . . .	78
D-2	Identified (mean) time delays of the additional measurements with corresponding standard deviations . . . . .	79
D-3	Identified time delays of the additional measurements with corresponding standard deviations (sampled at 50 Hz) . . . . .	79



---

# Acknowledgements

First, I would like to thank Tamás Keviczky for his supervision and setting up this thesis project with the Netherlands Aerospace Centre (NLR).

Second, I would like to thank my daily supervisor Andres Jürisson for always being supportive and critical throughout writing this thesis. I highly value your open attitude and I am very grateful for the practical implementation experiences you gave me. Furthermore, I would like express my appreciation to Bart Eussen and Kees Wijnberg for asking the right questions and providing a pleasant working environment at NLR.

Apart from my supervisors, I want to thank, my roommates Pepijn and Daan, my friends from S&C and my buddies from Hilversum for making the best out of the pandemic and supporting me whenever I faced difficulties during this thesis project.

Lastly, I would like to thank my brother for always assisting me with good advice and my parents for encouraging my passion in aviation. Nailing it down to one of my favourite childhood books, "Bored – Nothing to do!", this thesis is a tribute to the curiosity and ingenuity that was fostered inside me from a young age.

Delft, University of Technology  
July 8, 2021

T.J. Plasmeijer



“Bored – Nothing to do!”

— *Peter Spier*



---

# Chapter 1

---

## Introduction

### 1-1 Motivation and problem formulation

The expected growth in flight activities and the increase in regulations to protect the environment is pushing the aerospace industry to develop highly efficient aircraft. To that aim, long and slender high aspect ratio wings, that produce less lift-induced drag, are used in fixed-wing airframes to improve aerodynamic efficiency. In the last decades, the large-scale usage of lightweight composite materials in high aspect ratio wings intensified to meet the increasingly demanding efficiency requirements of High Altitude Long Endurance (HALE) aircraft and Unmanned Aerial Systems (UAS) [3].

One tedious property of using composite materials in these high aspect ratio aircraft is that it comes with a decreased structural rigidity and an increase in flexibility. As a consequence, higher in-flight deformations occur and more interactions between the aerodynamic, elastic and inertial forces develop. At a critical airspeed, these aeroelastic interactions can even lead to an unstable and self-exciting and destructive structural oscillation called flutter. To alleviate these effects and to improve flight dynamic responses accordingly, the aid of active control systems are investigated in the field of aeroservoelasticity. This research field has become an increasingly more important in the last decades and focuses on describing the interactional behaviour between flight control systems, aircraft aeroelasticity and aircraft stability [4].

In this research area, various different projects are focused on acquiring aeroservoelastic modelling and control techniques to improve aircraft performance. One research project, funded by Europe, is the FLEXOP (Flutter Free FLight Envelope eXpansion for ecOnomical Performance improvement) project. This project aims to stimulate competitiveness by developing and demonstrating concepts that improve flight performance of high-aspect-ratio aircraft[5]. Another recent project is the X-56A project [6]. Here, NASA conducted multiple flight tests with the aim to investigate how system identification can aid in the development of more accurate aeroservoelastic models.

In this trend, the Netherlands Aerospace Centre (NLR) has set up a project to accurately construct aeroservoelastic models through system identification of real flight-test data. To

gain more experience in this field, a 1 to 3 scaled flexible Unmanned Aerial Vehicle (UAV) is instrumented with multiple sensors to measure the structural flexibility during flight. By flying specific manoeuvres and gathering the structural flexibility measurements, the goal is to acquire an accurate aeroservoelastic model. The main benefit of acquiring an aeroservoelastic model through this approach is that it does not require specific knowledge about the aircraft's internal and structural properties. Since these characteristics are often not provided by aircraft manufactures, aircraft operators are keen to utilize such system identification methods to understand and improve their aeroservoelastic aircraft performance.

Despite this benefit, challenges arise when considering that an autopilot needs to be designed for automating the corresponding flight testing and data gathering processes. Usually, accurate aeroservoelastic models are used for the control synthesis to guarantee both stability and performance. With regards to the flexible and high aspect ratio drone of NLR, these models are not yet available and a robust flight controller against these aeroservoelastic effects has to be developed. This requirement opens up the following interesting research opportunity:

**Design and implement a reference tracking controller that is robust against the aeroservoelastic effects of a high aspect ratio and flexible aircraft.**

The aim of this thesis is thus to constitute an important step in the development and application of a robust and real-time implementable control system for a flexible and high aspect ratio aircraft. Looking at this goal, the idea is to develop a control synthesis method that does not necessarily require high fidelity aeroservoelastic models. This synthesis method may, therefore, aid in the development of robust control systems for future HALE aircraft and UAS. This is especially relevant when considering that aeroservoelastic system identification campaigns and high fidelity modelling approaches are often costly and computationally intensive.

The problem of developing a controller with an uncertain aeroservoelastic model is that the undesired interactions are described by various types of rigid and structural modes in the system. In traditional flight control, the structural modes are often outside the control activity bandwidth and the control of the rigid-body motions can be isolated from the structural motions. This is illustrated in the left of Figure 1-1. In this thesis, the structural modes

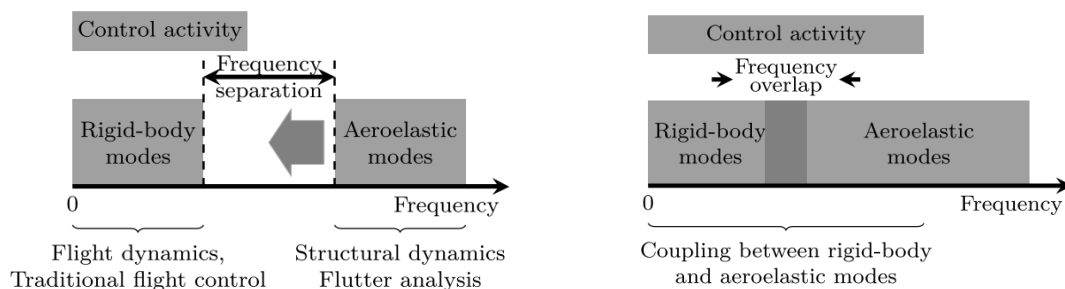


**Figure 1-1:** Sufficient frequency separation for classical control in the left figure. Frequency overlap in aeroservoelastic control in the right figure [1]

are considered to be inside this control activity bandwidth and close to the rigid-body modes in terms of frequency. As such, accurate models are commonly required to emulate these aeroservoelastic coupling effects. Although an accurate model of these coupled dynamics

is initially unavailable for the flexible and gliding drone of NLR, an already identified and validated model of a comparable full-scale glider with a similar aspect ratio will be considered for evaluating the aeroservoelastic interactions of the developed controllers.

## 1-2 Related work

In literature, several types of control design methodologies are proposed that can cope with the earlier introduced coupling effects of aeroservoelasticity. In the FLEXOP project [7] a family of airspeed scheduled Proportional-Integral-Derivative (PID) controllers are used to control the rigid-body motions of a flexible demonstrator aircraft. Here, passive roll-off filters are used to isolate the rigid-body controller from the flutter suppression controller proposed in [8]. Although these isolated controllers can have good robustness properties when the frequency separation is large, they may induce reduced phase and stability margins when applied to systems with smaller frequency separations. To overcome this undesired effect of passive solutions, active controllers are developed.

Among those active solutions, the flutter suppression controllers in [8] and [9] are providing a systematic way to extend the flight envelope. Despite flutter being of no concern in this thesis, the used  $\mathcal{H}_\infty$  control methods can still be promising for various aeroservoelastic control applications. For instance, in [10] a  $\mathcal{H}_\infty$  design approach for a large flexible blended wing body is developed to achieve reference tracking, manoeuvring load alleviation and control effort reduction. Furthermore, a  $\mathcal{H}_\infty$  controller for gust rejection on large and very flexible aircraft is investigated and reported in [11]. Note that these control synthesis methods are relying on linear representations of the coupled aeroservoelastic dynamics. As high order systems are typically required to describe these dynamics, model reduction techniques in [12] are often utilized to capture the most dominant aeroservoelastic effects for control. These model reduction method in particular find their application in an extension of  $\mathcal{H}_\infty$  control known as Linear Parameter Varying (LPV) control that to establish smooth scheduling in between the linear design operating points. LPV control has recently been demonstrated on a passenger aircraft in [13] and has extensively been investigated for suppressing flutter on the X-56A aircraft in [14] and [9]. Although these types of control methods can be synthesized with known parametric and robustness characteristics, research is also focused on developing nonlinear control strategies that can compensate for unbounded parametric uncertainties.

Risk-averse adaptive control is a commonly used terminology of an adaptive control strategy in aeroservoelastic control applications. This technique is designed for the X-56A aircraft and is proposed in [15]. Here, a non-adaptive control law, that guarantees nominal performance, is extended with an independent Model Reference Adaptive Control (MRAC) law to achieve better robust performance. Similar in [16], this non-adaptive Linear Quadratic Gaussian Proportional Integral (LQG-PI) controller is accommodated with a closed-loop reference model to also establish output feedback with the extended adaptive component. However, for translating this to Multi-Input-Multi-Output (MIMO) systems, a high frequency gain has to be competed which often requires specific knowledge about the system. Furthermore, not all uncertainties and external disturbances can get parameterized and adapted using this framework.

As an alternative, Nonlinear Dynamic Inversion (NDI) or Feedback Linearization (FBL) controllers are used to control the nonlinear behaviour of flight dynamics without requiring

classical linear gain scheduling techniques. In this trend, the application of NDI to a flexible HALE aircraft is explored under ideal simulations conditions in [17]. When considering model mismatches and noisy measurements, a version of NDI that is less model-dependent and more sensor-based was developed to increase robust performance. This variation is known as Incremental Nonlinear Dynamic Inversion (INDI) control and has been applied to a free-flying flexible aircraft in [18] to regulate rigid-body motions, alleviate gust loads and reduce the wing root bending moments. Although this control method tends to be promising for the control problem at hand, it is limited in its practical implementation due to its dependency on load models and elastic state information. Recently, this method has been extended to a multi-loop control architecture in [19] with NDI and incremental backstepping sliding mode controllers to account for position control, flight path control, attitude control and load alleviation. Similar as in [18], this reported method is limited in its practical implementation as the effects of sensor noise, time delays and biases were not considered.

### 1-3 Research objective

As no accurate model of the flexible demonstrator is available yet, INDI control is chosen for robustly handling its rigid-body motions. However, at the moment, literature seems to be lacking the practical implementation of an INDI controller to flexible aircraft structures. This thesis work will, therefore, focus on how INDI control can aid in improving reference tracking performance and structural motion relaxation. By taking into account the presence of sensor noise and time delays, this work will identify the unfavourable aeroservoelastic effects and aims to compensate for them accordingly. Consequently, the objective mentioned in the previous section can be refined to the following main research question:

**How can an incremental nonlinear dynamic inversion flight controller be synthesized and implemented for a flexible and gliding demonstrator to achieve reference tracking of attitude angles and structural motion alleviation?**

Looking at this research question it should be noticed that the structural motion alleviation inherently implies a more relaxed structural response and less unfavourable aeroservoelastic interactions. To evaluate this relaxation and to design, verify and validate the synthesis method for it accordingly, the following sub-questions are formulated:

- *What synthesis method can be developed to simultaneously achieve reference tracking and structural motion alleviation in the presence of sensor noise and time delays?*

Devising a synthesis method for obtaining a real-time implementable controller for aeroservoelastic systems, will be the cornerstone challenge that needs to be addressed. The new method should embrace the scalability to flexible aircraft with little prior information about aeroservoelastic coupling.

- *How does the performance and robustness of the synthesized INDI control structure compare to the conventional INDI controller and a comparable baseline controller?*

For the applicability to various aeroservoelastic systems across different domains, the resulting synthesized controller should be robust against the uncertain coupling effects of aeroservoelasticity.

- ***How can the developed controllers be implemented and validated on the flexible and gliding UAV of NLR?***

To date, the implementation and validation of an INDI controller on an aeroelastic aircraft has not been investigated. Hence, there is no validation data of INDI showing its added value in aeroservoelastic control applications.

These sub-questions suggest that three different controllers are used for evaluating tracking and structural motion alleviation. In this context, the conventional INDI controller solely refers to the validated and working controller proposed in literature. The baseline controller is a linear PID controller that is tuned to similar response characteristics as the INDI controller. The synthesized INDI controller accommodates an additional linear controller that is obtained through a multi-objective  $\mathcal{H}_\infty$ -norm minimization. A substantial part of this research is thus the development, implementation and comparison of these three latter controllers.

## 1-4 Challenges and thesis contributions

The challenges that are concerned with the design, implementation and comparison of these latter controllers are best described in terms of their corresponding research contributions. Among others, the main challenge of this thesis is to validate the controllers through implementing them on existing hard-and-software platforms. For acquiring a modular tuning and testing platform the controllers are simulated and implemented using MATLAB/Simulink. Accordingly, a corresponding Hardware-in-the-loop (HIL) simulation with Simulink and the existing hard-and-software platform has to be developed. Although this challenge does not contribute to research results directly, the development of this HIL platform can still aid in accelerating the implementation and verification of controllers in future research projects. The reason for this is that it is open-source, low in cost and modular to the various types of airframe simulations and controllers build in Simulink. For this research particularly, the following three research contributions are formulated:

- ***Showing the limitations that are concerned with implementing an INDI controller on an aeroservoelastic aircraft***

Although several INDI based control strategies are developed to improve aeroservoelastic flight dynamic responses, their performance degradation due to hardware events has only received limited attention in literature. In this work, these hardware events will be identified and included to address the limitations of various INDI controllers in their applicability to aeroelastic aircraft.

- ***Development of a synthesis method for alleviating the, by the INDI controller introduced, adverse aeroservoelastic interactions.***

With aeroservoelastic interaction being heavily dependent on the configured control gain, the tuning of the INDI controller can become challenging. While in [20] a Multi-Objective-Parameter-Optimization (MOPS) tool is used to find the INDI control gains,

this work proposes the development of a complete synthesis formulation to achieve the desired response fastness, disturbance rejection and structural motions alleviation.

- ***Implementation and validation of the INDI controller on the flexible demonstrator of NLR.***

An important challenge is to successfully implement and validate the conventional INDI. Despite INDI control laws having already been validated on quad-rotor UAVs and fixed-wing aircraft in [21] and [22], its implementation and applicability to aeroservoelastic aircraft has never officially been investigated and published.

## 1-5 Outline of this thesis

This chapter gave an overview of the project background and introduced the reader to the problematic coupling effects in aeroservoelastic control. The remainder of the thesis is structured as follows. The preliminary theory used in this thesis is given in Chapter 2. In here, the incremental nonlinear control techniques together with the linear  $\mathcal{H}_\infty$  control synthesis and relevant performance and robustness criteria are discussed. In Chapter 3, an aeroservoelastic model will be derived based on the aircraft's equations of motion in an aeroelastic reference frame. This obtained model is then used to verify the various types of INDI and  $\mathcal{H}_\infty$  controllers in Chapter 4. The resulting synthesised controllers are then compared both in simulation and through real flight tests in Chapter 5. Lastly, this thesis is concluded with an overall conclusion and discussion in Chapter 6.

# Incremental NDI and $\mathcal{H}_\infty$ control synthesis theory

This chapter presents an introduction of the basic theory and principles of incremental nonlinear dynamic inversion and  $\mathcal{H}_\infty$  control synthesis. The introduction in Chapter 1 already noted that INDI is a variation on Nonlinear Dynamic Inversion (NDI). Moreover, the INDI controller developed uses an INDI inner loop combined with an NDI outer loop. Hence, also an understanding of the basic theory and principles of NDI are considered important for this report. Furthermore, not all aeroservoelastic interaction can be decoupled or controlled by INDI. Therefore,  $\mathcal{H}_\infty$  control synthesis is introduced to reduce the closed-loop frequency peaks with guaranteed local linear stability. Lastly, relevant metrics for assessing the control performance and robustness are presented.

## 2-1 Nonlinear Dynamic Inversion

Nonlinear Dynamic Inversion aims to make the closed-loop nonlinear system, fully or partially, linear controllable by cancelling the nonlinearities using exact state transformations and feedback. This technique employs the concept of input-output feedback linearization which is conceptually different from Jacobian linearization presented in A-2-1. To introduce the concept of input-output feedback linearization, consider the following nonlinear function for a Multi-Input-Multi-Output (MIMO) dynamical system with  $m$  equal number of outputs as inputs

$$\begin{aligned}\dot{\mathbf{x}} &= \mathbf{f}(\mathbf{x}) + \mathbf{g}(\mathbf{x})\mathbf{u} \\ \mathbf{y} &= \mathbf{h}(\mathbf{x}).\end{aligned}\tag{2-1}$$

Where,  $\mathbf{f}(\mathbf{x})$  and  $\mathbf{g}(\mathbf{x})$  are denoted as nonlinear function mappings of the state vector  $\mathbf{x} \in \mathbb{R}^n$ . Note that this can be also be written in terms of single input entities as

$$\dot{\mathbf{x}} = \mathbf{f}(\mathbf{x}) + \sum_{i=1}^m g_i(\mathbf{x})u_i,\tag{2-2}$$

with  $g_k(\mathbf{x}) \in \mathbb{R}^n$  and  $u_k$  being the input scalars in  $\mathbf{u} \in \mathbb{R}^m$ . Similarly, the output vector  $\mathbf{y} \in \mathbb{R}^m$  can also be expressed in terms of scalar functions through  $\mathbf{y} = [h_1(\mathbf{x}) \dots h_m(\mathbf{x})]^T$ .

The principle of input-output feedback linearization is to differentiate the output  $r^d$  times until a linear relation between the input and output is found. Here,  $r^d$  represents the relative degree of the system. If  $r^d$  is less than the system order  $n$ , part of the system dynamics are unobservable and thus unstabilizable by the controller. These dynamics are referred to as internal dynamics and should be stable for the control design to work. For the derivation of this NDI control design, consider that the first derivative of the  $k_{th}$  output can be calculated using:

$$\dot{y}_k = \frac{\partial h_k(\mathbf{x})}{\partial t} = \frac{\partial h_k(\mathbf{x})}{\partial \mathbf{x}} \underbrace{\frac{\partial \mathbf{x}}{\partial t}}_{\dot{\mathbf{x}}} = \underbrace{\frac{\partial h_k(\mathbf{x})}{\partial \mathbf{x}} \mathbf{f}(\mathbf{x})}_{L_f h_k(\mathbf{x})} + \sum_{i=1}^m \underbrace{\frac{\partial h_k(\mathbf{x})}{\partial \mathbf{x}} g_i(\mathbf{x})}_{L_{g_i} h_k(\mathbf{x})} u_i, \quad (2-3)$$

Where  $L_f h_k = \nabla h_k(\mathbf{x}) \cdot \mathbf{f}(\mathbf{x})$  and  $L_{g_i} h_k = \nabla h_k(\mathbf{x}) \cdot g_i(\mathbf{x})$  are the Lie derivatives of the  $k_{th}$  component. In case the relative degree  $r_k$  is equal to 1, an input can be observed after differentiating the output only once. This implies that the Lie derivative  $L_{g_i} h_k \neq 0$ , *i.e.*  $\forall i = 1, \dots, m$ . When the relative degree is larger than 1 and  $L_{g_i} h_k = 0$ , the differentiation should be continued until one of the inputs appear. This implies that the following differentiating is performed up until  $L_{g_i} L_f^{r_k^d - 1} h_k(x) u_i = 0, \forall i = 1, \dots, m$ :

$$\begin{aligned} \ddot{y}_k &= L_f^2 h_k(\mathbf{x}) + \sum_{i=1}^m L_{g_i} L_f h_k(\mathbf{x}) u_i = \frac{\partial L_f h_k(\mathbf{x})}{\partial \mathbf{x}} \mathbf{f}(\mathbf{x}) + \sum_{i=1}^m \frac{\partial L_f h_k(\mathbf{x})}{\partial \mathbf{x}} g_i(\mathbf{x}) u_i \\ &\vdots \\ \ddot{y}_k^{(r_k^d)} &= L_f^{r_k^d} h_k(x) + \sum_{i=1}^m L_{g_i} L_f^{r_k^d - 1} h_k(x) u_i \end{aligned} \quad (2-4)$$

Summarizing this for all outputs  $m$  in a compact set of equation results in the following linear expression:

$$\underbrace{\begin{bmatrix} y_1^{(r_1^d)} \\ \vdots \\ y_m^{(r_m^d)} \end{bmatrix}}_{\mathbf{y}^{r^d}} = \underbrace{\begin{bmatrix} L_f^{(r_1^d)} h_1 \\ \vdots \\ L_f^{(r_m^d)} h_m \end{bmatrix}}_{\mathbf{a}(\mathbf{x})} + \underbrace{\begin{bmatrix} L_{g_1} L_f^{(r_1^d - 1)} h_1 & \dots & L_{g_m} L_f^{(r_1^d - 1)} h_1 \\ \vdots & \ddots & \vdots \\ L_{g_1} L_f^{(r_m^d - 1)} h_m & \dots & L_{g_m} L_f^{(r_m^d - 1)} h_m \end{bmatrix}}_{\mathbf{b}(\mathbf{x})} \mathbf{u}. \quad (2-5)$$

By introducing the new virtual control variable  $\boldsymbol{\nu} = \mathbf{y}^{r^d}$ , the above expression can be rewritten as:  $\boldsymbol{\nu} = \mathbf{a}(\mathbf{x}) + \mathbf{b}(\mathbf{x})\mathbf{u}$ . Assuming that the partial relative degrees in  $\mathbf{b}(\mathbf{x})$  are well defined and that  $\mathbf{b}(\mathbf{x})$  is invertible, the following control law can be specified to cancel the nonlinearities

$$\mathbf{u} = \mathbf{b}^{-1}(\mathbf{x})(\boldsymbol{\nu} - \mathbf{a}(\mathbf{x})). \quad (2-6)$$

Where  $\boldsymbol{\nu} = \mathbf{y}^{r^d}$  can be defined by a linear controller to control the output towards a desired reference. Important to realize is that the NDI method has limitations. The full state vector needs to be known and the relative degree of the system needs to be defined. Furthermore, as this method depends completely on the model of the system, robustness against modelling errors and external disturbances is not guaranteed [23]. The next section, therefore, derives a more robust variation of this NDI controller.

## 2-2 Incremental Nonlinear Dynamic Inversion

To overcome the robustness issues of the NDI controller a more robust variation known as Incremental Nonlinear Dynamic Inversion (INDI) has been developed in [24]. This INDI controller retains the nonlinearity cancelation advantages of NDI but decreases the dependency on the model by measuring or estimating the state derivatives from sensor data. The derivation of this INDI controller starts from the general system:

$$\begin{aligned}\dot{\mathbf{x}} &= \mathbf{f}(\mathbf{x}) + \mathbf{g}(\mathbf{x}, \mathbf{u}) \\ \mathbf{y} &= \mathbf{h}(\mathbf{x}).\end{aligned}\quad (2-7)$$

By performing the first Taylor series expansion of  $\dot{\mathbf{x}}$  with respect to previous time instance  $t_0$ , the following can be obtained:

$$\dot{\mathbf{x}} = \dot{\mathbf{x}}_0 + \underbrace{\left( \frac{\partial \mathbf{f}(\mathbf{x})}{\partial \mathbf{x}} + \frac{\partial \mathbf{g}(\mathbf{x}, \mathbf{u})}{\partial \mathbf{x}} \right)}_{A_0} \Big|_{\mathbf{x}_0} (\mathbf{x} - \mathbf{x}_0) + \underbrace{\frac{\partial \mathbf{g}(\mathbf{x}, \mathbf{u})}{\partial \mathbf{u}}}_{B_0} \Big|_{\mathbf{x}_0, \mathbf{u}_0} (\mathbf{u} - \mathbf{u}_0) + \underbrace{\mathcal{O}(\Delta \mathbf{x}^2, \Delta \mathbf{u}^2)}_{\epsilon}. \quad (2-8)$$

Here, the difference in state and input between time instances  $t$  and  $t_0$  can be defined by  $\Delta \mathbf{x} = \mathbf{x} - \mathbf{x}_0$  and  $\Delta \mathbf{u} = \mathbf{u} - \mathbf{u}_0$ . Using this, (2-8) can be rewritten as

$$\dot{\mathbf{x}} = \dot{\mathbf{x}}_0 + A_0 \Delta \mathbf{x} + B_0 \Delta \mathbf{u} + \epsilon. \quad (2-9)$$

Through considering a local affine relation between the system output and the control input, the higher terms contained in  $\epsilon$  can be discarded and the following control input increment can be defined:

$$\Delta \mathbf{u} = B_0^{-1}(\boldsymbol{\nu} - \dot{\mathbf{x}}_0 - A_0 \Delta \mathbf{x}). \quad (2-10)$$

Where the virtual input  $\boldsymbol{\nu}$  is represented by a linear input-output mapping through assuming full state feedback measurement meaning:

$$\begin{aligned}\mathbf{y} &= \mathbf{h}(\mathbf{x}), \\ \dot{\mathbf{y}} &= \boldsymbol{\nu}.\end{aligned}\quad (2-11)$$

Subsequently, by denoting the desired reference by  $\mathbf{y}_{\text{ref}}$  and linearly controlling  $\mathbf{y}$  towards it, a virtual control input can be defined and substituted in (2-10) to obtain the following control input increment:

$$\Delta \mathbf{u} = B_0^{-1}(K_p(\mathbf{y}_{\text{ref}} - \mathbf{y}) - \dot{\mathbf{x}}_0 - A_0 \Delta \mathbf{x}). \quad (2-12)$$

Instead of using only a proportional gain  $K_p$  for defining the virtual control, an integral gain or a feed-forward of  $\dot{\mathbf{y}}_{\text{ref}}$  can also be included to improve tracking performance [25]. By simply adding (2-12) to the previous or measured control input  $\mathbf{u}_0$  the total control input can be obtained:

$$\mathbf{u} = \mathbf{u}_0 + B_0^{-1}(K_p(\mathbf{y}_{\text{ref}} - \mathbf{y}) - \dot{\mathbf{x}}_0 - A_0 \Delta \mathbf{x}). \quad (2-13)$$

To reduce the model dependency from this control law, the system dynamics increment denoted by  $A_0 \Delta \mathbf{x}$ , can be neglected by selecting a high sampling frequency and relying on the time-scale separation assumption. This permits the following simplification of (2-12):

$$\mathbf{u} = \mathbf{u}_0 + B_0^{-1}(K_p(\mathbf{y}_{\text{ref}} - \mathbf{y}) - \dot{\mathbf{x}}_0). \quad (2-14)$$

The next subsection will further elaborate upon this time-scale separation assumption through discussing its application to multi-loop control structures and INDI control strategies. Subsequently, a similar PID controller will be derived for comparison later on. Finally, the concept of pseudo control hedging will be introduced to alleviate the performance degradation due to control saturation, biases and time delays.

### 2-2-1 Time scale separation principle

The time scale separation principle assumes that slow states are regarded invariant with respect to the fast states and the fast states change instantly with respect to the slow states. In flight control applications, this principle is explained by considering the pitch dynamics of a fixed-wing aircraft. Here, the effect of an elevator deflection appears quicker in the pitch rate response than in the response of the pitch angle. As such, these dynamics are different in time scales and can be controlled separately in cascaded loops.

For INDI control this principle can be applied to a local time increment  $\Delta t$  by assuming that the change in state vector  $\Delta \mathbf{x}$  is much smaller the change in the control input vector  $\Delta \mathbf{u}$ . By translating this to the mathematical definition

$$A_0(\mathbf{x}_0, \mathbf{u}_0) \Delta \mathbf{x} \ll B_0(\mathbf{x}_0, \mathbf{u}_0) \Delta \mathbf{u}, \quad (2-15)$$

and selecting a fast update rate for the controller, the system dynamics increment  $A_0 \Delta \mathbf{x}$  term in (2-13) can be neglected.

### 2-2-2 Pseudo Control Hedging

Pseudo Control Hedging (PCH) was first introduced to INDI in [26]. The benefit of PCH applied to INDI is that it can act as an anti-windup technique for the linear controller inside the INDI control loop. This allows PCH to alleviate the performance degradation due to control saturation, biases and time delays. PCH changes the reference for the incremental control loop when the commanded control input  $\mathbf{u}_c$  is not identical to the measurable actual actuator displacement  $\mathbf{u}_a$ . For the derivation of PCH, let the pseudo-control hedge being defined by

$$\boldsymbol{\nu}_h = \boldsymbol{\nu}_c - \hat{\boldsymbol{\nu}}. \quad (2-16)$$

Here, the commanded virtual control input is  $\boldsymbol{\nu}_c$  and the estimated virtual control input is denoted by  $\hat{\boldsymbol{\nu}}$ . This estimate is obtained through the difference between the commanded control input  $\mathbf{u}_c$  and the actual measured control input:

$$\hat{\boldsymbol{\nu}} = B_0(\mathbf{u}_a - \mathbf{u}_c). \quad (2-17)$$

To implement the virtual hedging accordingly, a reference model that imposes the desired dynamics  $\mathbf{x}_{I,c}$  on the measured output will be designed. This reference model is defined through:

$$\mathbf{x}_{I,rm} = \frac{1}{s}(\boldsymbol{\nu}_{rm} - \boldsymbol{\nu}_h) \quad \text{with} \quad \boldsymbol{\nu}_{rm} = K_{rm}(\mathbf{x}_{I,c} - \mathbf{x}_{I,rm}). \quad (2-18)$$

Where  $K_{rm}$  is a diagonal gain matrix and  $\mathbf{x}_{I,rm}$  is sent to the linear controller in the INDI control loop. Note that this reference model will act as a low-pass filter for cases where the

commanded control input is equal to the measured control input. In cases where control saturation occurs, it holds that  $v_h \neq 0$  and the commanded  $\mathbf{x}_{I,rm}$  reference is adjusted.

Recently, in [27], this PCH method is applied to an INDI controller that is subjected to unsynchronized time delays of  $\mathbf{u}_a$  and  $\dot{\mathbf{x}}_0$ . Here, it is shown that PCH can shift the region of adequate performance towards a surplus of delays  $\dot{\mathbf{x}}_0$  when instead of  $K_{rm}$  a PI controller is used in combination with P-control for defining virtual control input. An advantage of this structure is that a bias on the actuator position measurements will not result in a steady-state error in the closed-loop response. This, however, comes at the cost of losing the anti-windup benefit.

### 2-2-3 Similar PID controller

In [28], it is shown that there exist similarities between the INDI controller and the well-known proportional-integral controller. As PID controllers are often easy to tune on-site, this similar controller will be derived in this section for comparison purposes later on. For the derivation of this controller, a system with a first-order actuator model will be considered. This actuator model can be defined in the time domain through:

$$\dot{u}_a = -\frac{1}{\tau_a}u_a + \frac{1}{\tau_a}u_c. \quad (2-19)$$

With  $u_c$  denoting the commanded control input,  $u_a$  representing the actual control input and  $\tau_a$  being time constant specified as one over the actuator bandwidth  $\tau_a = \frac{1}{\omega_a}$ . By substituting in the the incremental control input  $u_c = u_a + \Delta u$  the following relation can be obtained:

$$\begin{aligned} \dot{u}_a &= -\frac{1}{\tau_a}u_a + \frac{1}{\tau_a}(u_a + \Delta u) \\ &= \frac{1}{\tau_a}\Delta u. \end{aligned} \quad (2-20)$$

Integrating this relation will reveal a expression for the actual control input  $u_a$ . By adding the result to the incremental input  $\Delta u$  the commanded control input can be found:

$$u_c = \frac{1}{\tau_a} \int_0^t \Delta u d\tau + \Delta u. \quad (2-21)$$

By recalling the control law of INDI in 2-14 and considering  $x = y$  with a feed-forward derivative term  $\dot{x}_{ref}$ , the incremental control input is defined through

$$\Delta u = B_0^{-1} (K_p(x_{ref} - x) - \dot{x}_0 + \dot{x}_{ref}). \quad (2-22)$$

When considering small sampling times with respect to the change in state, the tracking error can be approximated using  $z(t) \approx x_{ref}(t) - x(t - T_s)$ . Now the commanded input can be obtained by substituting 2-22 in 2-21:

$$\begin{aligned} u_c(t) &= \int_0^t \frac{B_0^{-1}}{\tau_a} (K_p z(\tau) - \dot{x}_0(\tau - \tau_a) + \dot{x}_{ref}(\tau)) d\tau + B_0^{-1} (K_p z(t) - \dot{x}_0(t - T_s) + \dot{x}_{ref}(t)) \\ &= \frac{B_0^{-1}}{\tau_a} \left( K_p \int_0^t z(\tau) d\tau + z(t) \right) + B_0^{-1}(x)(K_p z(t) + \dot{z}) \\ &= B_0^{-1} \left( \frac{K_p}{\tau_a} \int_0^t z(\tau) d\tau + \left( \frac{1}{\tau_a} + K_p \right) z(t) + \dot{z} \right). \end{aligned} \quad (2-23)$$

Accordingly, similarities to PID control can be observed when rewriting 2-23 as

$$u(t) = \underbrace{B_0^{-1} \left( \frac{1}{\tau_a} + K_p \right)}_{K_p^{PID}} z(t) + \underbrace{B_0^{-1} \frac{K_p}{\tau_a}}_{K_i^{PID}} \int_0^t z(t) dt + \underbrace{B_0^{-1}}_{K_d^{PID}} \dot{z}(t). \quad (2-24)$$

A benefit of this PID controller is that the actuator dynamics are directly incorporated in the controller gains and that thus no additional actuator feedback measurement is required. Contrary, it is important to realize that the  $z(t)$  approximation is not always valid in practical implementations when time delays cannot be neglected. Nonetheless, the results obtained in (2-24) are still considered to be useful for acquiring a comparable INDI response in simulation.

## 2-3 $\mathcal{H}_\infty$ control synthesis

The use of  $\mathcal{H}_\infty$  design is found in a variety of aeroservoelastic flight control applications to damp or reduce the closed-loop frequency response peaks of the flexible and structural modes. As such,  $\mathcal{H}_\infty$  control techniques are utilized to suppress flutter [], to alleviate gust loads [11] or to reduce both manoeuvring loads and control activity while tracking [10]. Two main benefits of  $\mathcal{H}_\infty$  control synthesis can be observed in this context. First,  $\mathcal{H}_\infty$  is a multivariable control method technique that can find a stable controller with its activity confined to the desired frequency range. Second, good robustness can be achieved by minimizing the frequency response peaks at specific locations in control loop. For these two main reasons, the design formulations of  $\mathcal{H}_\infty$  will be detailed in this section. To elaborate on the  $\mathcal{H}_\infty$  synthesis method, first the general  $\mathcal{H}_\infty$  design optimization is introduced where thereafter its application to multi-objective requirements is introduced by means of a mixed-sensitivity description.

### 2-3-1 General $\mathcal{H}_\infty$ optimization

The optimization is formulated using the general configuration as presented in Figure 2-1. Here, the generalized plant  $P$  has two inputs and two outputs. The exogenous input  $\mathbf{w} \in \mathbb{R}^{n_d}$  includes references and disturbances signals while the manipulated input  $\mathbf{u} \in \mathbb{R}^m$  is calculated by the controller  $K$  based on measured output in  $\mathbf{v} \in \mathbb{R}^\ell$ .

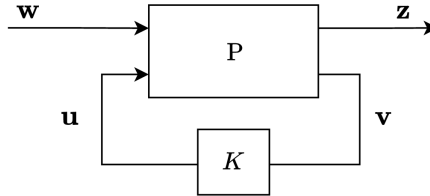


**Figure 2-1:** Generalized interconnection for  $\mathcal{H}_\infty$  control synthesis

In transfer function formulae, the system is

$$\begin{bmatrix} \mathbf{z} \\ \mathbf{v} \end{bmatrix} = P(s) \begin{bmatrix} \mathbf{w} \\ \mathbf{u} \end{bmatrix} = \begin{bmatrix} P_{11}(s) & P_{12}(s) \\ P_{21}(s) & P_{22}(s) \end{bmatrix} \begin{bmatrix} \mathbf{w} \\ \mathbf{u} \end{bmatrix}, \quad \mathbf{u} = K(s)\mathbf{v}. \quad (2-25)$$

The goal is to find a stabilizing controller  $K(s)$  that minimizes the maximum closed-loop gain from  $\mathbf{w}$  to the performance channels  $\mathbf{z} \in \mathbb{R}^{n_z}$  over all frequencies  $\omega$  and input/output directions using the  $\mathcal{H}_\infty$ -norm, or the induced  $\mathcal{L}_2$ -norm:

$$\|G(s)\| = \sup_{\omega} \bar{\sigma}(G(j\omega)) = \sup_{d \in \mathcal{L}_2 \setminus \{0\}} \frac{\|\mathbf{z}\|_2}{\|\mathbf{w}\|_2}. \quad (2-26)$$

Here,  $\bar{\sigma}$  denotes the largest singular value and  $G(s) = \mathcal{F}_L(P, K)$  is the closed loop transfer function given by the linear fractional transformation:

$$\mathcal{F}_L(P, K) = P_{11} + P_{12}K(I - P_{22})^{-1}P_{21}. \quad (2-27)$$

It can sometimes useful to express  $P$  in terms of its state-space representation,

$$P \stackrel{s}{=} \left[ \begin{array}{c|cc} A & B_1 & B_2 \\ \hline C_1 & D_{11} & D_{12} \\ C_2 & D_{21} & D_{22} \end{array} \right], \quad (2-28)$$

to add non-physical performance channels  $\mathbf{z}$  and to ensure that the conditions for finding a controller  $K$  are satisfied. These solvability conditions are relying on the following assumptions that are obtained from [29]:

- (A1) For the existence of a stabilizing controller,  $(A, B_2, C_2)$  is be stabilizable and detectable.
- (A2) To ensure that the controller is proper, and hence, realizable,  $D_{12}$  and  $D_{21}$  have to be full rank.
- (A3) To prevent zero pole cancellation on the imaginary axis:

$$\left[ \begin{array}{cc} A - j\omega I & B_2 \\ C_1 & D_{12} \end{array} \right] \quad \text{and} \quad \left[ \begin{array}{cc} A - j\omega I & B_1 \\ C_2 & D_{21} \end{array} \right] \quad \text{have full column rank for all } \omega$$

- (A4)  $D_{11} = 0$  and  $D_{22} = 0$  to make  $P_{11}$  and  $P_{22}$  strictly proper, respectively.
- (A5) For simplicity it is sometimes assumed that  $D_{12} = \begin{bmatrix} 0 & I \end{bmatrix}^T$  and  $D_{21} = \begin{bmatrix} 0 & I \end{bmatrix}$
- (A6) There are no cross terms in the cost function ( $D_{12}^T C_1 = 0$ ) and process noise and measurement noise are uncorrelated ( $B_1 D_{21}^T = 0$ ).
- (A7)  $(A, B_1)$  is stabilizable and  $(A, C_1)$  is detectable.

### 2-3-2 Mixed sensitivity

The generalized plant in the proposed  $\mathcal{H}_\infty$  norm minimization can be reformulated to control problems with multi-objective requirements by adding frequency-dependent weights to the input and output channels. This  $\mathcal{H}_\infty$ -norm-based multi-objective framework is known as mixed sensitivity  $\mathcal{H}_\infty$  and is synonymously used in literature, often with a weighted loop-shaping design approach. In this approach, the controlled plant is pre-and post multiplied with compensators to achieve a desirable loop transfer that attenuates noise at high frequencies and tracks and rejects disturbances at lower frequencies. In this thesis, however, the term

mixed sensitivity is used for any norm minimization problem that involves multiple closed-loop transfer functions.

In flutter suppression control applications, the frequency-dependent input and output weights in the mixed sensitivity  $\mathcal{H}_\infty$  approach are often tuned to attenuate the structural modes without impairing the rigid-body dynamics or the handling qualities. In this work, however, the rigid-body frequencies are too close to the structural frequencies and the entire INDI control structure will be exploited in the mixed sensitivity framework to improve the smoothness of the structural flexibility in the response. To specify this smooth responsiveness, the next section will introduce relevant metrics.

## 2-4 Quantitative assessment criteria

To allow for an admissible comparison between the developed control systems, metrics are used to judge their performance and robustness. This section will introduce the reader to the relevant quantitative criteria metrics for assessing aeroservoelastic responses.

### 2-4-1 Control performance metric

A common way to evaluate the performance of a controller is by analyzing the error between the reference  $y_{k,\text{ref}}$  and output  $y_k$  for each measured sample  $k$ . For the aeroservoelastic application of the control systems, we also want to evaluate the interactions between the control input and the structural dynamics. As these interactions often produce oscillations in both control input and the output response, the following four metrics will be considered to evaluate both the control effort and the reference tracking performance:

- **Numerical integration:** Integrating the control input can emulate the total power required by the actuator [30]. This metric will therefore be used to quantify the control effort over a fixed period of  $T_{\text{end}}$  seconds. In addition, this metric can be used to evaluate whether oscillations or steady-state errors are present in the output responses. Due to the discrete nature of the practically implemented controllers, this metric is approximated via the numerical trapezoidal method:

$$\sum_{e_y} = \frac{T_{\text{end}}}{2N} \sum_{n=1}^N (|y_k - y_{k,\text{ref}}| + |y_{k+1} - y_{k+1,\text{ref}}|). \quad (2-29)$$

- **Root Mean Square (RMS) error:** Instead of adding all the contributions of each sample together, the root mean square error can be used as an indication of the average error of the total number of samples obtained. This metric is commonly used to evaluate the performance of many different control methods and is defined by:

$$y_{\text{RMS}} = \sqrt{\frac{1}{N} \sum_{k=1}^N (y_k - y_{k,\text{ref}})^2}. \quad (2-30)$$

- **$\mathcal{L}_\infty$  norm:** The stability and performance of non-linear controllers are often assessed by determining if the error dynamics is bounded by some  $\mathcal{L}$ -norm. In this work, only the  $\mathcal{L}_\infty$  norm will be used to either determine the peak values in signals or to obtain the maximum deviation from the desired reference.

$$\|y_k - y_{k,\text{ref}}\|_{\mathcal{L}_\infty} = \max_{k \in T} \{|y_k - y_{k,\text{ref}}|\}. \quad (2-31)$$

- **Cumulative Moving Standard Deviation:** A suitable metric for quantifying the oscillations in signals is the Cumulative Moving Standard Deviation (CMSD). Since oscillations in the individual control actions can damage the hardware of actuators, this metric can be used to assess the control effort. The CMSD can also be used to evaluate the oscillations or energy of the structural modes in simulation. This metric is recently introduced by [30] and accumulates the moving standard deviation of  $n_s$  samples along the entire sample space independently. As such, the CMSD is defined by:

$$y_{\text{CMSD}} = \sum_{j=n_s/2+1}^{N-n_s/2} \sqrt{\frac{1}{n_s-1} \sum_{k=0}^{n_s-1} s_j[k]}, \quad \text{with } s_j[k] = (\mu[j - n_s/2 + k] - \bar{\mu})^2, \quad (2-32)$$

where,  $s_j[k]$  is the squared deviation from the mean of the set of data samples of  $j$  with mean  $\bar{\mu}_j$ .

## 2-4-2 Control robustness metrics

Although INDI control strategies are known through their sufficient robust performance, a thorough analysis would be required to guarantee that the sensor-based INDI controller and the model-dependent  $\mathcal{H}_\infty$  controller are stable across an uncertain parametric space. Commonly, gain and phase margins are used to evaluate how much phase and gain variations single loop transfer functions can tolerate before reaching instability. Given the MIMO nature of the controller, one could consider disk margins to investigate acceptable gain and phase variations on different channels. However, due to the additional filtered angular rate and actuator feedback in INDI control, these metrics will provide insufficient insight. Another tool for evaluating robustness that comes with the  $\mathcal{H}_\infty$  synthesis method is the minimization of maximum singular values in feedback signals. By adding real and complex uncertain dynamics to the generalized plant, robust controllers can be synthesized

Note that these latter stability margins are computed using linear systems. Given the non-linear control nature of INDI, other nonlinear certificates have to be considered. These type of certificates can be classified into analytic and simulation-based metrics. While analytical metrics are often overly conservative and are requiring high computational resources, simulation-based metrics are widely applied in the certification industry. Despite their dominant use, it is worth noticing that their computational advantages impair when various parameter configurations and disturbance are considered. As a result, repeated simulations have to be performed to acquire reliable computations of these simulation certificates. Monte Carlo techniques are often used to compute these repeated simulations over the admissible ranges of parametric uncertainties and disturbances.

As in INDI control continuous input-output feedback linearization is performed using measured feedback, it is considered to be highly robust against parametric uncertainties. Despite

this benefit, a drawback is that its stability is more affected by hardware events such as noise, biases and time delays. Through considering these effects, a relevant metric for evaluating robustness could be the identification of acceptable phase lags or time delays. This stability metric is better known as the Time Delay margin and will be further introduced in the next subsection.

### Time Delay Margin

The Time Delay Margin (TDM) is defined as the largest time delay within the system before closed-loop instability is reached. In this context, it can be seen as a potential successor of phase margin for evaluating how much phase lag a system can tolerate [31]. Contrary to the control of linear systems, the computation of this metric is analytically challenging when considering nonlinear controllers. Therefore, in this work, robustness will be evaluated by computing the time delay margins using repeated simulations.

These repeated simulations consist of trial and error Simulink runs using different parameters and inputs in which the upper-bound TDM is found using the bisection method. Additional metrics such as the  $\mathcal{L}_\infty$  norm or  $\sum_e$  can be included to identify instability. Note that the parameters that are affecting the fastness of the aircraft response are influencing the TDM the most. For these parameters, an additional repeated simulation can be performed.

# Aeroservoelastic modelling of a fixed-wing aircraft

So far, all the basic tools that are required for developing flight control laws have been presented. Before assessing the performance and limitations of these tools, first, an aeroservoelastic platform of a flexible glider will be derived. This chapter will present this platform by introducing relevant variable notions and corresponding reference frame definitions. For the derivation of the aeroelastic equations of motions, the chapter starts with discussing the underlying assumptions. Subsequent sections will then present the actuator dynamics and elaborate upon the corresponding aeroservoelastic characteristics.

### 3-1 Assumptions and reference frames

In literature, several types of nonlinear modelling techniques are proposed to simulate the aeroservoelastic coupling effects [32]. Instead of using these complex nonlinear models, this thesis considers a linear rigid and structural coupling relation by relying on the mean axis formulation [33]. The main benefit of this framework is that the resulting state vector is a direct extension of the known state vector in rigid aircraft dynamics. As this is attractive for the planned system identification method at NLR, the mean axis formulation based model will be used for control design. To arrive at a complete mean axis based modelling framework, the following most important assumptions are made:

1. The effects of the earth's curvature and rotation are neglected. Hence, the earth is assumed to be flat and the north-east-down directions are chosen as an inertial reference.
2. The gravitational force that acts on the glider in a vertical direction is constant as the mass of the glider does not change during flight and low altitude is considered.
3. Steady flow conditions are assumed. Implying that aerodynamic forces and moments are obtained through the glider its attitude with respect to the free-stream velocity.

4. Structural and aerodynamic contributions are modelled in the same moving reference frame by relying on the mean-axis formulation assumptions listed in [33]:
  - (a) Structural deformation is small and described by a set of eigenmodes.
  - (b) Moments and products of inertia do not vary with deformations
  - (c) Deformation and deformation rates are assumed to be colinear
  - (d) Aerodynamic forces are modelled by the quasi-steady strip theory

Note that the first three assumptions are valid for modelling a rigid aircraft while the last 4 sub-assumptions are listed for establishing a reference frame for modelling the aeroelastic effects. To arrive at this reference frame notion, the following right-handed coordinate frames are defined:

**Earth-fixed inertial reference frame:** Earth-fixed reference frame ( $\mathcal{O}_I$ ) is considered to be the inertial reference frame that is fixed to a certain location on the surface of the flat earth. Its  $X_I$ ,  $Y_I$  and  $Z_I$  axis are pointing to the same North, East and Down (NED) directions as the navigation reference frame.

**Navigation reference frame:** The navigation reference frame ( $\mathcal{O}_N$ ) is a translating NED reference that coincides with the aircraft's center of gravity. Its axis  $X_N$ ,  $Y_N$  and  $Z_N$  are aligned with the same NED directions of the inertial frame and its location is defined by the position vector  $\mathbf{R}_0$  as illustrated in Figure 3-1.

**Body reference frame:** The body reference frame ( $\mathcal{O}_B$ ) is a rotating reference frame with respect to the navigation reference frame. Its origin is fixed to the aircraft's body and coincides with the origin of the navigation frame. The  $X_B$ -axis points in the nose direction, the  $Y_B$ -axis points in the starboard direction and the  $Z_B$ -axis points towards the downward direction. The aircraft's accelerations, velocities and rates are usually defined in this reference frame. The transformation from this body frame to the navigation frame is defined in terms of three Euler angles:

$$\mathbb{T}_N^B(\phi, \theta, \psi) = \begin{bmatrix} 1 & 0 & 0 \\ 0 & \cos(\phi) & \sin(\phi) \\ 0 & -\sin(\phi) & \cos(\phi) \end{bmatrix} \begin{bmatrix} \cos(\theta) & 0 & -\sin(\theta) \\ 0 & 1 & 0 \\ \sin(\theta) & 0 & \cos(\theta) \end{bmatrix} \begin{bmatrix} \cos(\psi) & \sin(\psi) & 0 \\ -\sin(\psi) & \cos(\psi) & 0 \\ 0 & 0 & 1 \end{bmatrix}. \quad (3-1)$$

**Stability reference frame:** The stability reference frame is used to define the aerodynamic lift, drag and side forces. Consequently, its  $X_S$  and  $Z_S$  axis are aligned with the directions of the lift and drag force, respectively. The  $Y_S$  axis is aligned with the  $Y_B$  axis of the body frame and its origin is fixed to the aircraft's center of gravity. The body frame can be found by rotating the stability reference with the angle of attack using the following transformation:

$$\mathbb{T}_B^A(\alpha) = \begin{bmatrix} \cos(\alpha) & 0 & -\sin(\alpha) \\ 0 & 1 & 0 \\ \sin(\alpha) & 0 & \cos(\alpha) \end{bmatrix}. \quad (3-2)$$

**Mean axis reference frame:** The mean axis reference frame is a body reference frame that coincides with the instantaneous center of gravity of the aircraft. This instantaneous center of gravity moves with the deformation of structure by following assumptions 4a-c and

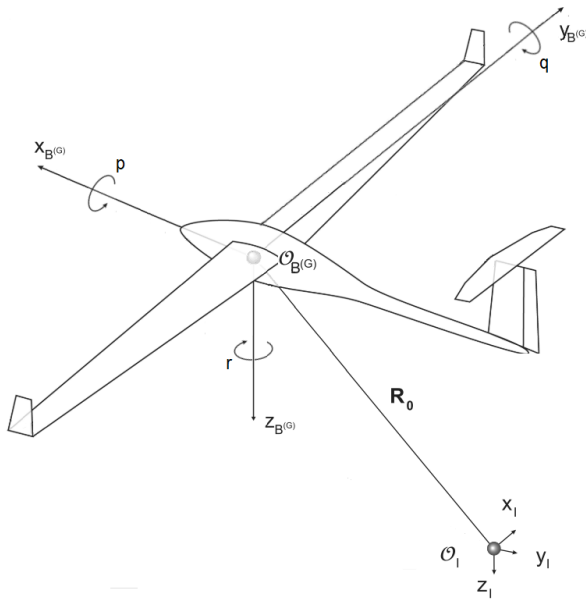


**Figure 3-1:** Inertial and body reference frame of an undeformed or rigid glider [2]

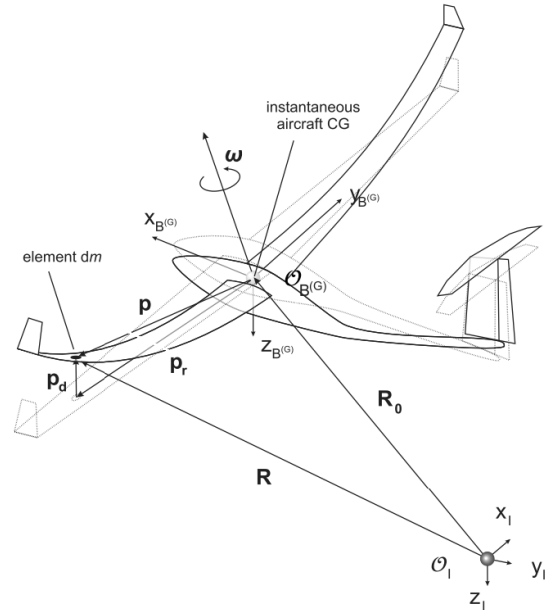


**Figure 3-2:** Mean axes reference frame of a deformed glider [2]

constraining the internal translational and rotational momentum to zero [33]. As a result, the mean axis reference frame is defined as common moving reference frame in which the rigid body states can be augmented with the flexible states.

The definitions of these augmented flexible states are obtained by recalling assumption 4a and analyzing Figure 3-2. Here, it is considered that the local linear and angular deformation,  $\mathbf{p}_d$  and  $\boldsymbol{\theta}_d$ , are described by an infinite superposition of orthogonal contributions:

$$\mathbf{p}_d(x, y, z, t)|_u = \sum_{i=1}^{\infty} \boldsymbol{\Phi}_i(x_u, y_u, z_u) \eta_i(t), \quad \boldsymbol{\theta}_d(x, y, z, t)|_u = \sum_{i=1}^{\infty} \nabla \boldsymbol{\Phi}_i(x_u, y_u, z_u) \eta_i(t). \quad (3-3)$$

Throughout this thesis, the  $i$ -th flexible state is defined as the generalized displacement amplitude  $\eta_i$  of the  $i$ -th structural mode. Multiplying this state with its corresponding mode shape  $\boldsymbol{\Phi}_i(x_u, y_u, z_u)$  results into its displacement. By summing up the contributions of all the structural modes, the total displacement with respect to the local coordinate  $x_u, y_u, z_u$  can be obtained. Note that (3-3) is often truncated by retaining only the most dominant modes within the frequency range of interest.

## 3-2 Aeroservoelastic model

As no validated model was initially available for the control synthesis of the 1:3 scaled Diana-2 glider, two models within the developed framework will be considered in this thesis. Both models rely on the same mean axes formulation but are different in terms of aircraft parameters and aerodynamic coefficients (as listed in A). The first model is developed and validated in [34] and includes estimates of the aerodynamic coefficients of a full scale SB-10 glider from real flight test data. The second model includes the coefficients of the 1:3 scaled Diana-2

glider that are numerically obtained using ZAERO's simulation software [35]. Although both models have similar aspect ratios, the aeroservoelastic characteristics are different due to the different structural properties and inertias. To investigate whether these aeroservoelastic effects can be problematic in controlling the rigid-body motions, first the equations of motion with corresponding aerodynamic forces and moments will be derived.

### 3-2-1 Equations of motion

The equations of motion of a flexible aircraft in the mean axis reference frame can be defined by applying the Euler-Lagrange equations to the motion of a flexible body with a constant mass. The resulting rigid body state update of both the translational and rotational velocities, included in the vectors  $\mathbf{V}_B = [u \ v \ w]^T$  and  $\boldsymbol{\omega} = [p \ q \ r]^T$ , are described by the following first two equations:

$$\begin{aligned}\dot{\mathbf{V}}_B &= -\boldsymbol{\omega}_B \times \mathbf{V}_B + \mathbb{T}_B^N \mathbf{G}_N + \frac{1}{m} \mathbf{F}_B^{\text{ext}} \\ \dot{\boldsymbol{\omega}}_B &= -J^{-1} (\boldsymbol{\omega}_B \times (J\boldsymbol{\omega}_B)) + J^{-1} \mathbf{M}_B^{\text{ext}} \\ \ddot{\boldsymbol{\eta}} &= -2\xi\omega_{nF}\dot{\boldsymbol{\eta}} - \omega_{nF}^2\boldsymbol{\eta} + \mu^{-1}\mathbf{Q}_\eta,\end{aligned}\tag{3-4}$$

where the gravity force vector  $\mathbf{G}_N$  is transformed to the body reference frame using the transpose of (3-1). The external forces and moments are described by the vectors  $\mathbf{F}_B^{\text{ext}} = [\mathcal{X} \ \mathcal{Y} \ \mathcal{Z}]^T$  and  $\mathbf{M}_B^{\text{ext}} = [\mathcal{L} \ \mathcal{M} \ \mathcal{N}]^T$ , while the products of inertia terms are included in the matrix:

$$J = \begin{bmatrix} I_{xx} & 0 & -I_{xz} \\ 0 & I_{yy} & 0 \\ -I_{xz} & 0 & I_{zz} \end{bmatrix}.\tag{3-5}$$

Note that these external forces and moments are dependent on both the rigid and flexible states. The flexible states in this context are updated through a spring-mass damper system that is forced by some generalized load  $\mathbf{Q}_\eta$  as modelled by the third expression in (3-4). Here, each  $i$ -th structural mode has its undamped natural frequency  $\omega_i$ , damping ratio  $\xi_i$  and modal mass  $\mu_i$ . By truncating (3-3) to a number of  $nF$  structural modes, these parameters can be included in the diagonal matrices  $\omega_{nF}$ ,  $\xi_{nF}$  and  $\mu_{nF}$ .

Depending on the structural properties of the airframe, different type of modes can be observed within the structure. Ground vibrations tests are usually performed to identify the undamped natural frequencies with corresponding mode shapes. The modes that can interfere with the control system are often the ones with the lowest natural frequencies. In high aspect ratio and fixed-wing airframes, these slow modes often represent the symmetric wing bending motions. For the SB-10 glider, the shapes of the three lowest structural frequencies are illustrated in Figure 3-3 and are deflecting the wing symmetrically,

The structural modes that higher are in frequencies are commonly concerned with asymmetric motions. For the SB-10 glider, the shapes of these modes are displayed in Figure 3-4.

### 3-2-2 Aerodynamical forces and moments

The aerodynamic forces can be decomposed into two main components. A lift force that is perpendicular to the airflow direction and a drag force that is opposite to the airflow

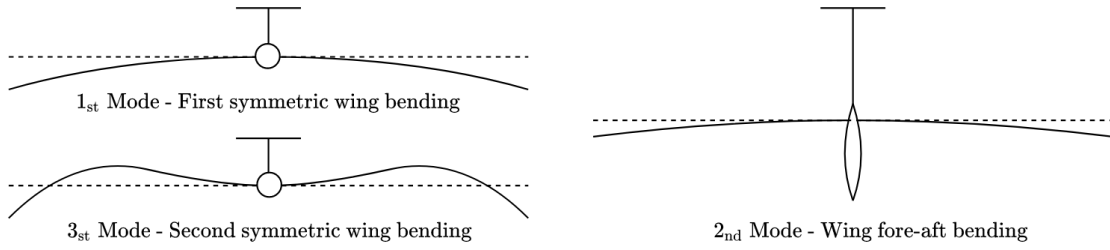


**Figure 3-3:** The first three symmetric wing bending modes of the full scale SB-10 glider

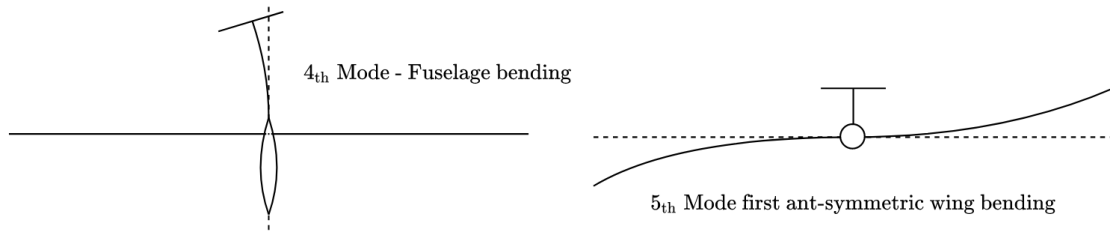


**Figure 3-4:** The two asymmetric structural modes of the full scale SB-10 glider

direction. These aerodynamic forces are defined in the stability and are transformed to the body reference frame to obtain the external forces, moments and generalized loads of (3-13):

$$\mathbf{F}_B^{\text{ext}} = \bar{q} S \mathbb{T}_B^A \underbrace{\begin{bmatrix} -C_D \\ C_Y \\ -C_L \end{bmatrix}}_{\mathbf{C}_F}, \quad \mathbf{M}_B^{\text{ext}} = \bar{q} S \mathbb{T}_B^A M \underbrace{\begin{bmatrix} C_L \\ C_M \\ C_N \end{bmatrix}}_{\mathbf{C}_M} + \Delta_{cg} \mathbf{F}_B^{\text{ext}}, \quad \mathbf{Q}_\eta = \bar{q} S e \mathbf{C}_Q. \quad (3-6)$$

Here,  $S$  is the wing surface area and  $\bar{q} = \frac{1}{2} \rho V^2$  is the dynamic pressure. The moment arm distances from the centre of gravity to the aerodynamic centre of pressure are included in  $\Delta_{cg}$  and are normalized by the diagonal matrix  $M$  that includes the aerodynamic chord length  $\bar{c}$  and the wingspan  $b$  on the rows for symmetric and asymmetric motions, respectively. The aerodynamic force and moment coefficients that are contained in  $\mathbf{C}_F$  and  $\mathbf{C}_M$  and are deduced from the quasi-steady strip theory according to assumption 4d. Here, it is assumed that the aerodynamic moment coefficient  $\mathbf{C}_M$ , the generalized force coefficient  $\mathbf{C}_Q$ , and the aerodynamic force coefficients  $C_Y$  and  $C_L$  are a linear combination of the rigid body states, the flexible body states and the control surface deflections:

$$\begin{bmatrix} \mathbf{C}_F \\ \mathbf{C}_M \\ \mathbf{C}_Q \end{bmatrix} = \underbrace{\begin{bmatrix} A_{RR} & A_{RF} & B_R \\ A_{FR} & A_{FF} & B_F \end{bmatrix}}_{A_M} \underbrace{\begin{bmatrix} \mathbf{x}_R \\ \mathbf{x}_F \\ \mathbf{u} \end{bmatrix}}_{\mathbf{v}} + \frac{1}{\pi A_s e} \underbrace{\mathbf{p} \mathbf{v}^T A_M^T W A_M \mathbf{v}}_{C_L^2}. \quad (3-7)$$

The drag force coefficient  $C_D$  is assumed to be parabolic with regard to the lift coefficient as indicated by the most right term in (3-7). To model this induced drag, this term is multiplied with the inverse of the aspect ratio  $A_s$  and the inverse of the Oswald factor  $e$ . Furthermore, the single-entry vector  $\mathbf{p}$  and single-entry matrix  $W$  are included to select the correct row vectors for adding the induced drag contribution and squaring the lift coefficient, respectively.

Following the quasi-steady strip theory, the linear relations in (3-7) with the respect to rigid and linear flexible states contained in  $\mathbf{x}_R$  and  $\mathbf{x}_F$  can be derived by assuming that the 2-dimensional lift force is essentially dependent on the local angle of attack. This local angle of attack at a  $x, y$  in  $X_B - Y_B$  plane of the body frame can be approximated using (3-3) through:

$$\alpha_s = \underbrace{\alpha_v + i_s - q \left( \frac{\Delta x + e_{ac}}{u} \right) + p \frac{y}{u}}_{\text{rigid dynamics}} + \underbrace{\sum_{i=1}^{\infty} \left[ \left( \frac{d\Phi_i^b}{dx} \right) \eta_i + \frac{1}{u} \Phi_i^b \dot{\eta}_i \right]}_{\text{flexible dynamics}}. \quad (3-8)$$

Where  $\alpha_v = \tan^{-1}(u/w)$ ,  $i_s$  is the incidence angle and  $\Delta x + e_{ac}$  is the distance between the  $Y_B$  axis and the axis of the aerodynamic centre (AC). By relying on this quasi-steady strip theory and grouping the rigid and flexible contributions, the linear coupling between the rigid body and flexible body in (3-7) can be defined through the following definition

$$A_{RR}\mathbf{x}_R = \sum_{k=1}^{nR} \begin{bmatrix} -C_{Dx_k} x_k \\ C_{Yx_k} x_k \\ -C_{Lx_k} x_k \\ C_{\mathcal{L}x_k} x_k \\ C_{\mathcal{M}x_k} x_k \\ C_{\mathcal{N}x_k} x_k \end{bmatrix}, \quad A_{RF}\mathbf{x}_F = \sum_{i=1}^{nF} \begin{bmatrix} -C_{D\eta_i} \eta_i - C_{D\dot{\eta}_i} \hat{\eta}_i \\ C_{Y\eta_i} \eta_i + C_{Y\dot{\eta}_i} \hat{\eta}_i \\ -C_{L\eta_i} \eta_i - C_{L\dot{\eta}_i} \hat{\eta}_i \\ C_{\mathcal{L}\eta_i} \eta_i + C_{\mathcal{L}\dot{\eta}_i} \hat{\eta}_i \\ C_{\mathcal{M}\eta_i} \eta_i + C_{\mathcal{M}\dot{\eta}_i} \hat{\eta}_i \\ C_{\mathcal{N}\eta_i} \eta_i + C_{\mathcal{N}\dot{\eta}_i} \hat{\eta}_i \end{bmatrix}. \quad (3-9)$$

Note that  $nR$  denotes the number of rigid body states included in the state vector  $\mathbf{x}_R$  and that  $nF$  denotes the number of retained structural modes. As such, the size of  $\mathbf{x}_F$  is  $2nF \times 1$  to include both the modal amplitude and the modal velocity as state variables. The linear relationship of the rigid and flexible states with regards to the generalized force coefficients is described through a similar procedure:

$$A_{FR}\mathbf{x}_F = \sum_{k=1}^{nR} \begin{bmatrix} C_{x_k}^{\eta_i} x_k \\ C_{x_k}^{\eta_{i+1}} x_k \\ \vdots \\ C_{x_k}^{\eta_{nF-1}} x_k \\ C_{x_k}^{\eta_{nF}} x_k \end{bmatrix}, \quad A_{FF}\mathbf{x}_F = \sum_{j=1}^{nF} \begin{bmatrix} C_{\eta_j}^{\eta_i} \eta_j + C_{\dot{\eta}_j}^{\eta_i} \hat{\eta}_j \\ C_{\eta_j}^{\eta_{i+1}} \eta_j + C_{\dot{\eta}_j}^{\eta_{i+1}} \hat{\eta}_j \\ \vdots \\ C_{\eta_j}^{\eta_{nF-1}} \eta_j + C_{\dot{\eta}_j}^{\eta_{nF-1}} \hat{\eta}_j \\ C_{\eta_j}^{\eta_{nF}} \eta_j + C_{\dot{\eta}_j}^{\eta_{nF}} \hat{\eta}_j \end{bmatrix} \quad (3-10)$$

The input and state variables contained in the vectors  $\mathbf{u}$  and  $\mathbf{x}_R$  are presented in Section A for the SB-10 and Diana2 model. Both models have the same control actions available, only the variables in  $\mathbf{u}$  and  $\mathbf{x}_R$  are different for the SB-10 and Diana-2 model due to the different methods used for acquiring the corresponding coefficients. All coefficients in (3-9) and (3-10) are dimensionless resulting in that the angular rate and modal velocity states in  $\mathbf{x}_R$  and  $\mathbf{x}_F$  are scaled with their respective reference length and normalized by the total velocity  $V$ :

$$\hat{p} = \frac{pb}{2V}, \quad \hat{q} = \frac{q\bar{c}}{2V}, \quad \hat{r} = \frac{rb}{2V} \quad \text{and} \quad \hat{\eta}_i = \frac{\dot{\eta}_i \bar{c}}{2V} \quad (3-11)$$

To arrive at a complete and compact set of equations for the flexible glider, consider that the forces and moment in (3-6) can be also be written as:

$$\begin{bmatrix} \mathbf{F}_B^{\text{ext}} \\ \mathbf{M}_B^{\text{ext}} \\ \mathbf{Q}_\eta \end{bmatrix} = \bar{q}S \underbrace{\begin{bmatrix} \mathbb{T}_B^A & 0 & 0 \\ \Delta_{cg} \mathbb{T}_B^A & M \mathbb{T}_B^A & 0 \\ 0 & 0 & \bar{c} \end{bmatrix}}_T \begin{bmatrix} \mathbf{C}_F \\ \mathbf{C}_M \\ \mathbf{C}_Q \end{bmatrix}. \quad (3-12)$$

By substituting (3-7) into this expression and combining it with the set of equations in (3-4), the following equations of motion can be obtained for the flexible aircraft:

$$\begin{bmatrix} \dot{\mathbf{V}}_B \\ \dot{\boldsymbol{\omega}}_B \\ \ddot{\boldsymbol{\eta}} \end{bmatrix} = \begin{bmatrix} -\boldsymbol{\omega}_B \times \mathbf{V}_B + \mathbb{T}_B^N \mathbf{G}_N \\ -J^{-1}(\boldsymbol{\omega}_B \times (J\boldsymbol{\omega}_B)) \\ -2\xi\omega_{n_F}\dot{\boldsymbol{\eta}} - \omega_{n_F}^2\boldsymbol{\eta} \end{bmatrix} + \bar{q}S \begin{bmatrix} \frac{1}{m} & 0 & 0 \\ 0 & J^{-1} & 0 \\ 0 & 0 & \mu^{-1} \end{bmatrix} T \left( A_M \mathbf{v} + \frac{1}{\pi A_s e_o} \mathbf{p} \mathbf{v}^T A_M^T W A_M \mathbf{v} \right). \quad (3-13)$$

Additionally, the update equations for the angle of attack  $\alpha$  and slide slip angle  $\beta$  are modelled by extracting the linear and rotational acceleration from  $\dot{\mathbf{V}}_B$  and  $\dot{\boldsymbol{\omega}}_B$  and using:

$$\dot{\alpha} = \frac{u\dot{w} - w\dot{u}}{u^2 + w^2}, \quad \dot{\beta} = \frac{\dot{v}V - v\dot{V}}{V\sqrt{u^2 + w^2}}, \quad \text{with} \quad \dot{V} = \frac{u\dot{u} + v\dot{v} + w\dot{w}}{V}.. \quad (3-14)$$

### 3-2-3 Virtual sensor modelling

To measure the flexibility of the structure during flight, accelerometers and Inertial Measurement Units (IMU) were distributed along the airframe. For using these measurements in the upcoming chapter, the output of these sensors will be modelled using the variables defined by (3-13). Consequently, the virtual accelerometer output, located at a position  $k$  and displaced by  $(x_k, y_k, z_k)$  from the centre of gravity, can be calculated by summing the rigid and structural contributions:

$$\begin{aligned} a_{x,k} &= a_{x,\text{cg}} - x_k(q^2 + r^2) + y_k(pq - \dot{r}) + z_k(pr + \dot{q}) + \sum_{i=1}^{n_F} \Phi_{x_i}^k \ddot{\eta}_i \\ a_{y,k} &= a_{y,\text{cg}} + x_k(pq + \dot{r}) - y_k(p^2 + r^2) + z_k(qr - \dot{p}) + \sum_{i=1}^{n_F} \Phi_{y_i}^k \ddot{\eta}_i \\ a_{z,k} &= a_{z,\text{cg}} + x_k(pr - \dot{q}) + y_k(qr + \dot{p}) - z_k(p^2 + q^2) + \sum_{i=1}^{n_F} \Phi_{z_i}^k \ddot{\eta}_i. \end{aligned} \quad (3-15)$$

Where the first term corresponds to the measured acceleration at the center of gravity and the middle three terms are modelling the inertial effects of the displacement relative to the center of gravity. The last term represents the contribution of the modal accelerations that follow from (3-3). Note that the effects from the change in orientation of the sensor, due to the modal deflections, are neglected as small deformation is assumed. Similarly, the virtual output of the strain measurements of a strain gauge positioned at a location  $k$ , can be modelled through:

$$\epsilon_k = \epsilon_{0,k} + \sum_{i=1}^{n_F} \epsilon_{i,k}. \quad (3-16)$$

where  $\epsilon_{0,k}$  corresponds to the zero term in the strain measurement and  $\epsilon_{i,k}$  models the contribution of the  $i$ -th structural mode.

## 3-3 Actuator modelling

The actuators that drive the control surfaces are an important aspect in aeroelastical control applications. As already stated in Section 1-1, the actuator bandwidth is commonly

limiting when considering the control of the structural dynamics. If the natural frequencies of the structural modes are higher than the actuator bandwidth, the controller cannot actively control the corresponding structural dynamics. This section will, therefore, introduce the reader to the available control surfaces for achieving the desired control authority. As such, the actuator dynamics will be identified and the corresponding control activity region will be discussed.

### 3-3-1 Available control surfaces

In fixed-wing aircraft control a roll, pitch and yaw motion can be achieved by deflecting the aileron, elevator and rudder surfaces, respectively. In this context, an elevator trailing upwards, a left aileron deflecting downwards, a right aileron deflecting upwards and a rudder trailing to the right are defined as positive deflections. Both the Diana-2 and SB-10 glider are equipped with one elevator  $\delta_e$ , one rudder  $\delta_r$  and six ailerons  $\delta_a$ . These control surfaces are illustrated in Figure 3-5. The three ailerons on both wings can be combined to achieve

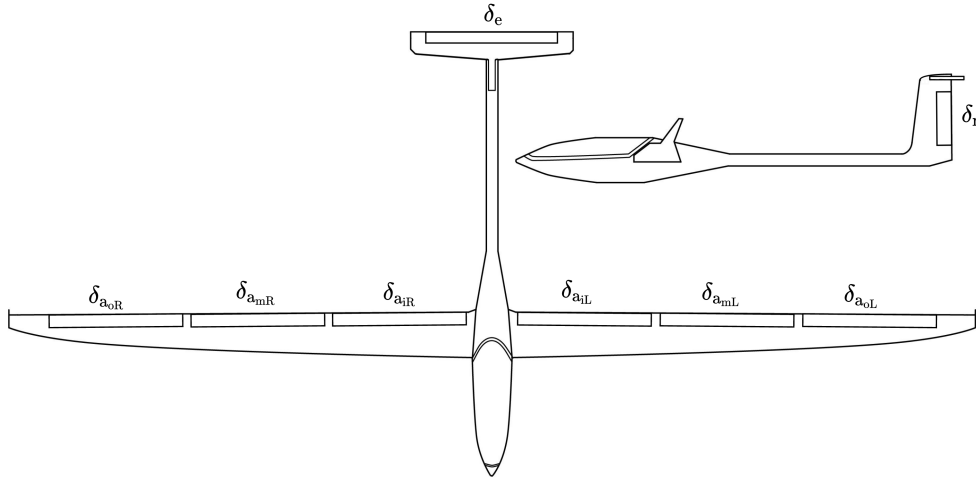


**Figure 3-5:** Available control surfaces deflections for both the Diana2 and SB-10 glider

the desired roll and structural motion control. Using this, the following two control allocation configurations will be considered in this thesis:

1. **Structural control:** In this configuration, the outer ailerons are deflected symmetrically to reduce possible wing bending motions. The middle ailerons are deflected asymmetrically to achieve the desired roll control effectiveness. As such, the following definitions are specified.

$$\delta_{fo} = \frac{1}{2}(\delta_{a_oL} + \delta_{a_oR}), \quad \delta_a = \frac{1}{2}(\delta_{a_mL} - \delta_{a_mR}), \quad \delta_{fi} = \frac{1}{2}(\delta_{a_iL} + \delta_{a_iR}) \quad (3-17)$$

Note, that the inner ailerons can only be deflected downwards to act as flaps.

2. **Conventional control:** As the control surfaces are less effective at low dynamic pressure, insufficient roll control authority can emerge during take off and landing. This

configuration, therefore, considers the combination of using both the middle and outer ailerons to increase roll effectiveness:

$$\delta_a = \frac{1}{2}(\delta_{a_{oL}} - \delta_{a_{oR}} + \delta_{a_{mL}} - \delta_{a_{mR}}), \quad \delta_{fi} = \frac{1}{2}(\delta_{a_{iL}} + \delta_{a_{iR}}). \quad (3-18)$$

The selection of the outer flaps to control the structural motions is based on the reasoning that the moment arm to the wing root location is larger than the middle aileron. This suggests that less outer flap deflection is needed for achieving an equal wing bending moment. Since it takes time for the actuator to achieve a certain deflection, less control effort is needed when selecting this outer flap. The next section will investigate how long this exactly takes by identifying the time constant of a suitable actuator model.

### 3-3-2 Actuator identification

As the incremental control laws discussed in Section 2-2 are relying on good actuator feedback, a model of the actuator will be used simulations to evaluate control performance. In this subsection, the identification procedure is briefly addressed. The complete identification of all the control servos including time delays is described in Section D-0-1.

The actuator models are identified by feeding three pulses and a chirp signal, at 20% of the maximum control surface deflection through all servos connected to the control surfaces. Magnetic position sensors, placed on the shaft of the servo, are used to measure the control surface deflections. Additionally, an IMU is placed on the control surface to observe any compliance in the linkage between the servo and the control surface.

The System Identification Toolbox in MATLAB is used to identify suitable actuator models. To obtain accurate dampening across the frequency range of the inputted chirp signal a second-order model structure is selected. The resulting bandwidths and damping ratios of the control surfaces on the Diana-2 are presented in Table 3-1. Looking at this table, it should

**Table 3-1:** Identified second order actuator model parameters of all 8 control surfaces installed on the Diana-2 demonstrator

	$\delta_{a_{oL}}$	$\delta_{a_{mL}}$	$\delta_{a_{iL}}$	$\delta_{a_{oR}}$	$\delta_{a_{mR}}$	$\delta_{a_{iR}}$	$\delta_r$	$\delta_e$
$\omega_a$ [rad/s]	56.46	51.85	49.75	59.56	52.58	55.88	32.81	34.83
$\zeta$ [-]	0.65	0.69	0.73	0.63	0.71	0.64	0.88	0.99

be seen that the outboard flaps have the highest bandwidth while the rudder and elevator are significantly lower in bandwidth. Note that this bandwidth is defined at the -3dB cross-over frequency and that more control effectiveness could be achieved beyond this bandwidth when the effectiveness of the control surfaces is sufficiently large.

Although these values apply to the Diana-2 demonstrator, it should be noticed that the actuator dynamics of the SB-10 glider are uncertain. To address the challenge presented Section 1-4 a representative actuator model will be selected instead. For the selection of this model, two conditions will be considered. First, to simplify the control problem, the same first-order actuator model will be applied to all control surfaces. Second, the selected bandwidth should be higher than the two most dominant structural modes for addressing the

aeroservoelastic control issues. Consequently, a first order actuator model with a bandwidth of 26.79 rad/s will be considered for the full-scale SB-10 model.

### 3-4 Aerodynamic damping

With the aeroservoelastic modelling framework defined, the frequency separations between the rigid and structural dynamics within the control activity bandwidth can be revealed. From (3-13) and (3-10) it is important to notice that natural frequency of structural modes is influenced by the aerodynamic generalized load  $Q_{\eta_i}$ . To analyse how the damping and natural frequency of both the rigid and structural dynamics change under different aerodynamic loadings, the poles of multiple linear systems are evaluated at different trim conditions using the linearization methods described in A-2. The resulting poles of both the SB-10 and Diana 2 glider are presented in Figure 3-6a and Figure 3-6b, respectively.

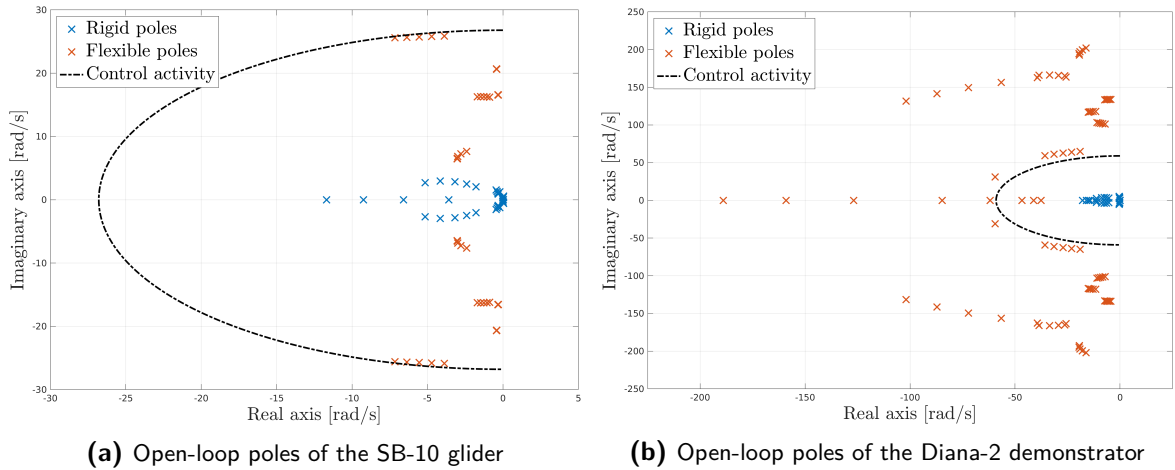


**Figure 3-6:** Open loop rigid poles (in blue) and structural poles (in red) of multiple linear systems, trimmed at 5 horizontal steady flight conditions between 20 m/s and 40 m/s

By looking at Figure 3-6 the following points should be observed before introducing the subsequent control system design chapter:

- Notice that poles in both graphs are all lying in the left half-plane and that no structural poles are crossing the imaginary axis. This suggests that open-loop stability is preserved and that no flutter is expected within the flight envelope of interest.
- Furthermore, one should see that the control activity region for SB-10 glider is large enough for controlling the structural dynamics. For the Diana-2 demonstrator, the control of the structural dynamics is limited by the identified actuator bandwidths. Hence, minor interactions with the structural dynamics and the control system is expected.

Based on these observations, it can be concluded that for addressing the challenges presented in 1-4, the SB-10 glider is better suited for evaluating the applicability of the proposed control methodologies in Chapter 2. To assess the performance and limitation of these methodologies, the full-scale SB-10 glider will be considered in the upcoming control design chapter.

In this SB-10 model, the dynamics of the first symmetric wing bending mode and second symmetric wing for aft bending mode are closest to the fastest rigid short-period mode. Therefore, these two symmetric structural modes can potentially interact with the control system when fast pitching motions are controlled. Note that the natural frequency and damping of these modes are plotted versus airspeed in Figure 3-7 to illustrate the effect of different aerodynamic loading. For the control design in the next chapter, it is important

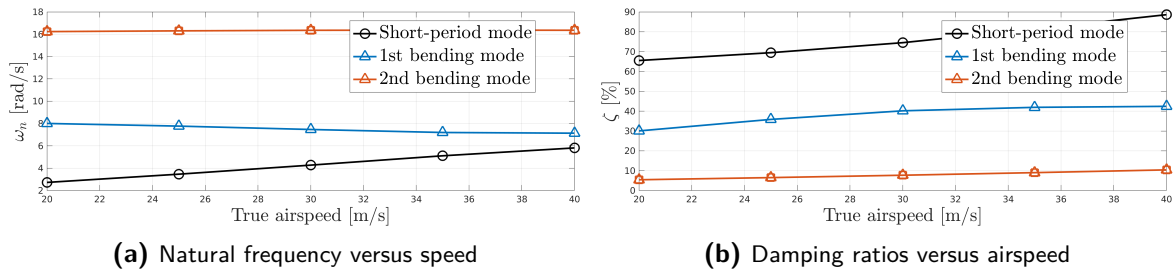


**Figure 3-7:** Change in natural frequency and damping of the first two structural modes and the rigid body short period at different flying velocities

to notice from Figure 3-7a that the frequency separation between the first symmetric wing bending and short period mode reduces with increasing airspeed. Furthermore, from Figure 3-7b it should be seen that the wing for aft bending is damped less than the symmetric wing bending mode.

### 3-5 Conclusive remarks

In this chapter, an aeroservoelastic modelling framework was introduced that can be parameterized with the coefficients of the full-scale SB-10 glider or the coefficients of the 1:3 scaled Diana-2 demonstrator. For control synthesis, the following conclusive remarks are made:

- In the proposed aeroservoelastic platform, the rigid and structural contributions are mostly linear with respect to their corresponding states. The only nonlinearities in this model are the transformations between reference frames, the calculation of the cross velocity terms and the multiplications with dynamic pressure. This suggests that linear control techniques can be applied to local dynamic pressure conditions when small aerodynamic angles are assumed.
- The proposed models of the SB-10 and Diana-2 are significantly different in structural properties in terms of mass and inertia. As such, the SB-10 glider is considered to be more flexible and thus better suited for evaluating the applicability of the proposed control methodologies. This model will, therefore, be considered in the upcoming control design chapter.



# Incremental NDI and $\mathcal{H}_\infty$ control synthesis for aeroservoelastic aircraft

This chapter elaborates on two control problems for which INDI and  $\mathcal{H}_\infty$  methods are used. First, an inner-loop INDI controller applied to the angular rate control is considered for controlling an aeroelastic airframe. Secondly, the INDI controller is blended into a linear and multi-objective synthesis formulation to reduce the unfavourable aeroservoelastic interactions. Lastly, to control pitch and roll angles, a compatible outer-loop control structure will be proposed.

## 4-1 Incremental Nonlinear Dynamic Inversion control

In this section, the INDI control methods discussed in 2-2 are applied to the flexible and full-scale SB-10 model. First, the applicability of the classical INDI angular rate controller to aeroservoelastic aircraft will be discussed. Subsequent subsections then present methods to compensate for the unfavourable aeroservoelastic interactions using elastic state information and Incremental Control Allocation (ICA) techniques.

To keep consistent with the notation of the angular rates and the attitude angles throughout this chapter, the control variables are defined as

$$\mathbf{x}_I = \begin{bmatrix} p \\ q \\ r \end{bmatrix}, \quad \mathbf{x}_{I,\text{ref}} = \begin{bmatrix} p_{\text{ref}} \\ q_{\text{ref}} \\ r_{\text{ref}} \end{bmatrix}, \quad \text{and} \quad \mathbf{x}_O = \begin{bmatrix} \phi \\ \theta \end{bmatrix}, \quad \mathbf{x}_{O,\text{ref}} = \begin{bmatrix} \phi_{\text{ref}} \\ \theta_{\text{ref}} \end{bmatrix}. \quad (4-1)$$

Here, the subscript I and O referring to the corresponding variables in the inner and outer loop, respectively. With referencing to Section 3-3-1, the considered control input vectors are denoted by:

$$\mathbf{u} = [\delta_a \quad \delta_e \quad \delta_r]^T, \quad \text{and} \quad \mathbf{u}_F = [\delta_a \quad \delta_e \quad \delta_r \quad \delta_{fo}]^T. \quad (4-2)$$

#### 4-1-1 INDI angular rate controller

Similar as presented in 2-9, the INDI control law can be derived by performing the first-order Taylor series expansion on the angular rate dynamics between a current and previous point in time:

$$\begin{aligned}\dot{\mathbf{x}}_I &\approx f_I(\mathbf{x}_0, \mathbf{u}_0) + \left. \frac{\partial f_I(\mathbf{x}, \mathbf{u})}{\partial \mathbf{x}} \right|_{\mathbf{x}=\mathbf{x}_0, \mathbf{u}=\mathbf{u}_0} (\mathbf{x} - \mathbf{x}_0) + \left. \frac{\partial f_I(\mathbf{x}, \mathbf{u})}{\partial \mathbf{u}} \right|_{\mathbf{x}=\mathbf{x}_0, \mathbf{u}=\mathbf{u}_0} (\mathbf{u} - \mathbf{u}_0) \\ \dot{\mathbf{x}}_I &\approx \dot{\mathbf{x}}_{I,0} + A_{I,0} \Delta \mathbf{x} + B_{I,0} \Delta \mathbf{u}.\end{aligned}\quad (4-3)$$

Relying on the time scale separation principle of Section 2-2-1, the  $A_{I,0} \Delta \mathbf{x}$  can be neglected and the incremental control law can be reduced to:

$$\Delta \mathbf{u} = B_{I,0}^{-1} (\boldsymbol{\nu}_I - \dot{\mathbf{x}}_{I,0}). \quad (4-4)$$

Where  $\boldsymbol{\nu}_I$  is linearly controlled to  $\dot{\mathbf{x}}_I$  with a proportional gain  $K_p$  to achieve the desired error dynamics. As such, the virtual control input can be defined as

$$\boldsymbol{\nu}_I = K_p (\mathbf{x}_{I,\text{ref}} - \mathbf{x}_I). \quad (4-5)$$

The total control law can then be obtained by substituting (4-5) in (4-4) and adding the resulting control increment to the previous measured control input

$$\begin{aligned}\mathbf{u} &= \mathbf{u}_0 + B_{I,0}^{-1} (\boldsymbol{\nu}_I - \dot{\mathbf{x}}_{I,0}) \\ &= \mathbf{u}_0 + B_{I,0}^{-1} (K_p (\mathbf{x}_{I,\text{ref}} - \mathbf{x}_I) - \dot{\mathbf{x}}_{I,0}).\end{aligned}\quad (4-6)$$

By defining the error dynamics as  $\mathbf{e} = (\mathbf{x}_{I,\text{ref}} - \mathbf{x}_I)$  and considering that  $B_{I,0}$  is defined by the control effectiveness equations from (3-13), the total control law in its full vector notation results into

$$\begin{bmatrix} \delta_a \\ \delta_e \\ \delta_r \end{bmatrix} = \begin{bmatrix} \delta_{a,0} \\ \delta_{e,0} \\ \delta_{r,0} \end{bmatrix} + \frac{J}{qS} \begin{bmatrix} bC_{L\delta_a} & 0 & bC_{L\delta_r} \\ 0 & \bar{c}C_{M\delta_e} & 0 \\ bC_{N\delta_a} & 0 & bC_{N\delta_r} \end{bmatrix}^{-1} \left( \begin{bmatrix} K_p & 0 & 0 \\ 0 & K_q & 0 \\ 0 & 0 & K_r \end{bmatrix} \begin{bmatrix} e_p \\ e_q \\ e_r \end{bmatrix} - \begin{bmatrix} \dot{p}_{I,0} \\ \dot{q}_{I,0} \\ \dot{r}_{I,0} \end{bmatrix} \right). \quad (4-7)$$

Here,  $\mathbf{u}_0$  is directly measured while  $\dot{\mathbf{x}}_{I,0}$  is often a finite difference approximation of a filtered angular rate measurement. This filter can be defined as:

$$H(s) = \frac{\omega_f^2}{s^2 + 2\omega_f s + \omega_f^2}. \quad (4-8)$$

The filter bandwidth  $\omega_f$  is selected such that noise at high frequency is attenuated. As the performance of the incremental controller relies on good synchronization of the measured states and inputs [27], the same filter will be applied to the actuator measurement  $\mathbf{u}_0$  to ensure an equal delay between both feedback signals. Figure 4-1 illustrates how this filter blocks and the finite difference approximation can be included in a discrete-time INDI control structure. Note that  $A(s)$  represents the actuator dynamics and that (4-8) is converted to  $H(z)$  using the Tustin transformation. Furthermore,  $D(z)$  represents a discrete-time derivative operator that will be further introduced in Section 4-2-1.

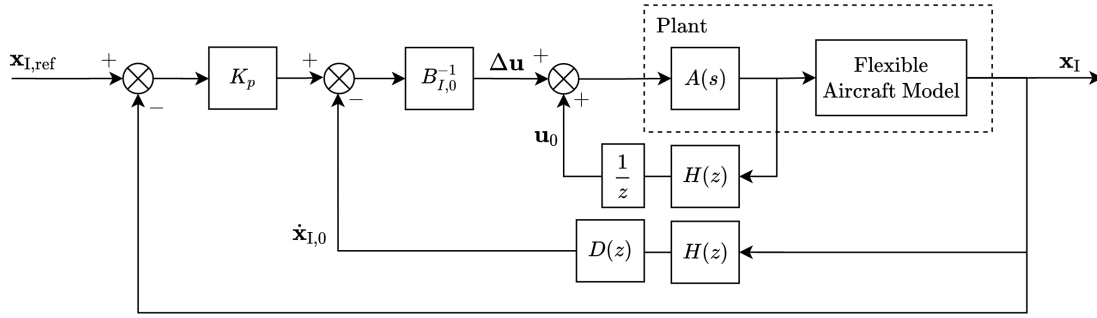


**Figure 4-1:** The resulting INDI control scheme including actuator dynamics  $A(s)$ , a discrete-time equivalent of the filter (4-8) denoted by  $H(z)$  and a discrete time finite difference operator  $D(z)$

To illustrate how the incremental control law interacts with the slowest symmetric bending modes, the pitch rate control law of (4-9) is simulated for an ideal and nominal case.

$$\delta_e = \delta_{e,0} + \frac{J\bar{c}}{\bar{q}S} C_{M_{\delta_e}^{-1}} (K_q e_q - \dot{q}_{I,0}). \quad (4-9)$$

The nominal case represents the realistic condition and includes the filter and actuator dynamics. The ideal case does not. The simulation conditions of these cases are clarified in Table 4-1. Note that the sampling rate is set to 100 Hz to satisfy the time scale separation assumption of (2-15). The filter bandwidth  $\omega_a$  is selected high enough to include the effect of the first two structural bending modes but low enough to attenuate noise at higher frequencies. The resulting pitch rate responses and elevator control inputs for a doublet reference are displayed in Figure 4-2. Compared to the ideal case, more oscillations in the

**Table 4-1:** The simulation conditions for the ideal and nominal case of the INDI angular rate controller

Case	$\omega_a$ [rad/s]	$\omega_f$ [rad/s]	Trim $V$ [m/s]	$K_q$ [-]	$T_s$ [sec]	Solver
Ideal	No	No	30	10	0.01	ode4 (Range Kutta)
Nominal	26.79	20	30	10	0.01	ode4 (Range Kutta)

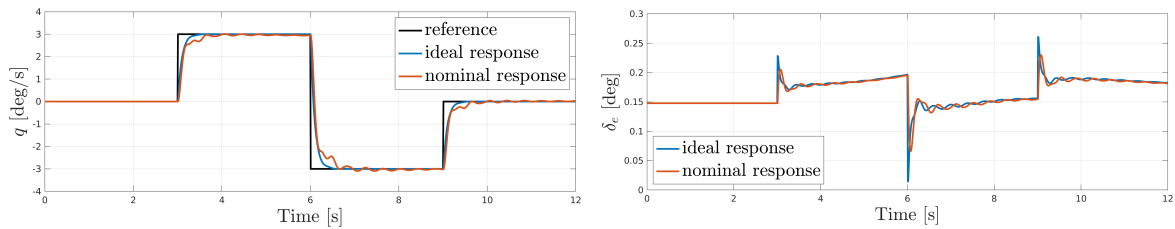


**Figure 4-2:** Simulated pitch rate response of (4-9) on the left, and corresponding elevator input on the right. Here, the ideal response is indicated in blue and the nominal response in red

pitch rate response and the elevator control input can be observed in the nominal case. The next subsection will investigate where these oscillations come from and how they can be attenuated.

#### 4-1-2 Incremental time delays

The ideal incremental control law of INDI assumes that the system dynamics increments can be neglected when high sampling rates are considered. In real-life applications however, where actuator dynamics and low pass filters are introducing additional phase lags, this assumption may not be valid anymore. This is explained by considering that the time interval at which the nonlinear dynamics are inverted is increased by the additional phase lags. As such, the contribution of the system dynamics increments enlarges and its effect becomes more dominantly present in the response. To validate whether the contribution of this increment can be neglected for flexible aircraft, this subsection focuses on breaking down the system dynamics increment term. For this, consider again the first-order Taylor-series expansion of (4-3). Here, the system dynamics increment is defined through the following partial derivative with respect to the full state vector  $\mathbf{x}$ :

$$\begin{aligned} A_{I,0}\Delta\mathbf{x} &= \left. \frac{\partial f_I(\mathbf{x}, \mathbf{u})}{\partial \mathbf{x}} \right|_{\mathbf{x}=\mathbf{x}_0, \mathbf{u}=\mathbf{u}_0} (\mathbf{x} - \mathbf{x}_0) \\ &= -J^{-1}(\omega_B \times (J\omega_B)) + \bar{q}S J^{-1}M \Delta\mathbf{C}_M. \end{aligned} \quad (4-10)$$

By considering that the effect of the cross-product of the angular rates is small, the system dynamics increment can be broken down into a component of the rigid-body dynamics and the structural dynamics:

$$A_{I,0}\Delta\mathbf{x} = \bar{q}S J^{-1}M \begin{bmatrix} A_{RR} & A_{RF} \end{bmatrix} \begin{bmatrix} \Delta\mathbf{x}_R \\ \Delta\mathbf{x}_F \end{bmatrix}. \quad (4-11)$$

In this respect,  $\Delta\mathbf{x}$  is partitioned into a vector  $\Delta\mathbf{x}_R$  that contains the rigid-body states and a vector  $\Delta\mathbf{x}_F$  that consist of the flexible states. These expressions show that the contribution of the system dynamics increases proportionally with the size of  $\Delta\mathbf{x}$ , or the incremental delay. The size of this incremental delay can be directly related to tracking errors and can be estimated through the following definition

$$\Delta t = nT_s + \frac{1}{\omega_a} + \frac{1}{\omega_f}. \quad (4-12)$$

Where  $n$  denotes the number of samples the flight computer needs for process the flight control algorithm. To investigate the effect of this incremental delay on the control of the flexible glider, the system dynamics increments of the rigid ( $A_{I,0}\Delta\mathbf{x}_R$ ) and the structural dynamics ( $A_{I,0}\Delta\mathbf{x}_F$ ) are calculated and plotted for the nominal case with  $n = 0$  and  $n = 5$  in Figure 4-3. This 5 sampled delay is inspired from the time delay identification presented in Section D-0-2.

Looking at the roll rate response, no significant structural dynamics increment can be observed. This can be explained by the large frequency separation between the spiral mode and the fifth asymmetric structural mode. The yaw response does show some structural oscillation due to relatively slow asymmetric fuselage bending mode. For the symmetric motions, where the structural frequencies are close to the natural frequency of the short period dynamics, a significant increase in structural dynamics increment between the  $n = 0$  and  $n = 5$  can be observed. Based on these observations, one can conclude that greater delays result in more interaction between the system dynamics increments and the controller. Instead of omitting these dynamics, the next subsection will show how these system dynamic increments can be incorporated in the control law to reduce the structural oscillations in the responses.

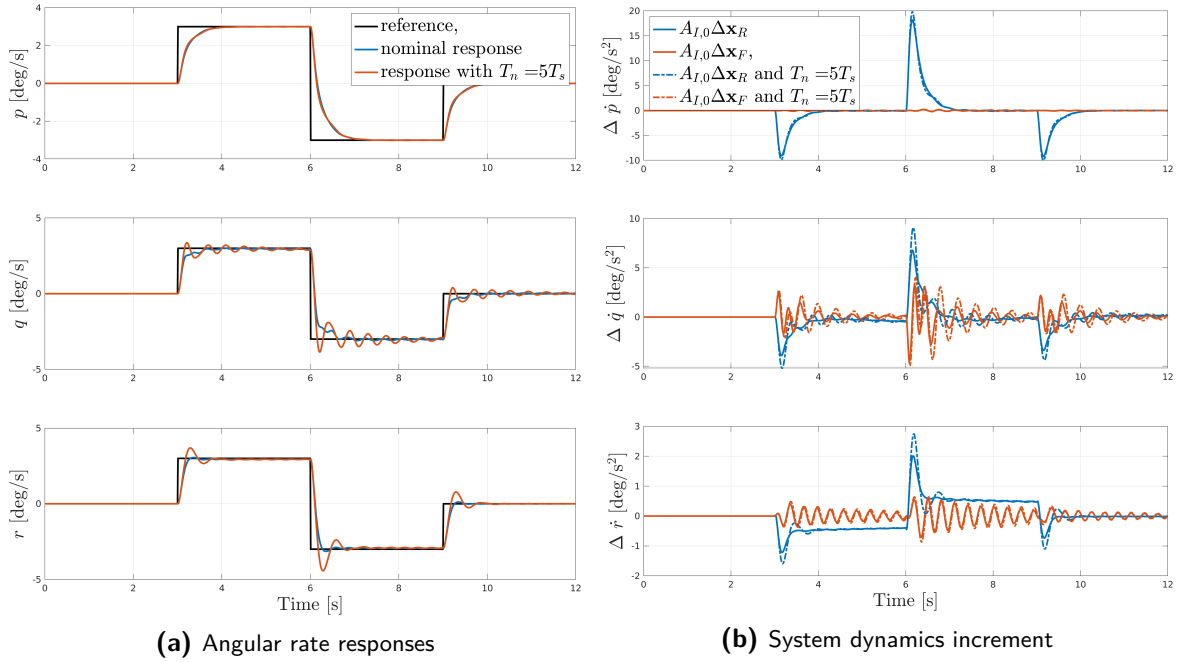


**Figure 4-3:** Doublet response of the angular rates in Figure 4-3a with corresponding rigid-body and structural dynamics increments in Figure 4-3b. The nominal and ideal case are described in Table 4-1

### 4-1-3 System dynamics increment compensation

As the dynamics of the first symmetric structural modes are affected the most by an increase in incremental delay, only the compensation for the pitching moment increment will be addressed. When the aeroservoelastic states are perfectly known, tracking performance can be improved by including the system dynamics increment in the incremental control step:

$$\Delta\delta_e = B_{q,0}^{-1}(K_q e_q - \dot{q}_0) - A_{q,0}\Delta\mathbf{x}. \quad (4-13)$$

By considering an actuator model in the continuous-time Laplace domain  $A(s)$  and the second-order filter of (4-8), the first-order Taylor approximation can be reconstructed using (4-13)

$$\begin{aligned} \dot{q} &\approx \dot{q}_0 + A_{q,0}\Delta\mathbf{x} + B_{q,0}\Delta\delta_e \\ &\approx \dot{q}_0 + A_{q,0}\Delta\mathbf{x} + B_{q,0}A(s) \left( B_{q,0}^{-1}K_q(e_q - H(s)\dot{q}_0) - A_{q,0}\Delta\mathbf{x} \right) \\ &\approx (1 - A(s)H(s))\dot{q}_0 + (1 - A(s))A_{q,0}\Delta\mathbf{x} + A(s)K_q e_q. \end{aligned} \quad (4-14)$$

From this last expression, it can be concluded that the compensation for the system dynamics increment cannot always be achieved due to the phase lags of the actuator model. In addition, the flexible states included in  $\Delta\mathbf{x}$  are typically hard to measure in aeroservoelastic control applications and can therefore not directly be used for compensating these system dynamics increments.

However, incorporating estimates of these states in the control law can still reduce the system dynamics increments by augmenting them to the control variable vector  $\mathbf{x}_I$ . This is often done in cases where known load models are available [18] [19]. Here, these load models are

used to generate accurate references for the augmented flexible states in the control variable vector. Generating such references in this thesis remains difficult due to the uncertainties involved and the modal nature of the considered modelling framework. Therefore, the next subsection will elaborate upon suitable control allocation methods to reduce the interaction between the control surface deflection and the structural dynamics.

#### 4-1-4 Incremental Control Allocation

To reduce the oscillations induced by the controller and the structural dynamics increments, control actions can be allocated in a way that its contribution to the structural increments is minimized. In this context, the control surfaces along the main wing can be deflected symmetrically to achieve the desired pitching moment without introducing a generalized load on the structural modes. With four symmetric control actions available and three symmetric modes included in the model, this optimal allocation can theoretically be obtained by extracting the control input vector from the following equality condition:

$$\begin{bmatrix} 0 \\ 0 \\ 0 \\ C_{\mathcal{M}} \end{bmatrix} = \begin{bmatrix} C_{n1\delta_{fo}} & C_{n1\delta_{fm}} & C_{n1\delta_{fi}} & C_{n1\delta_e} \\ C_{n2\delta_{fo}} & C_{n2\delta_{fm}} & C_{n2\delta_{fi}} & C_{n2\delta_e} \\ C_{n3\delta_{fo}} & C_{n3\delta_{fm}} & C_{n3\delta_{fi}} & C_{n3\delta_e} \\ C_{\mathcal{M}\delta_{fo}} & C_{\mathcal{M}\delta_{fm}} & C_{\mathcal{M}\delta_{fi}} & C_{\mathcal{M}\delta_e} \end{bmatrix} \begin{bmatrix} \delta_{fo} \\ \delta_{fm} \\ \delta_{fi} \\ \delta_e \end{bmatrix}. \quad (4-15)$$

Note that  $C_{\mathcal{M}}$  can be obtained by multiplying (4-9) with  $C_{\mathcal{M}\delta_e}$  as

$$C_{\mathcal{M}} = C_{\mathcal{M}\delta_e} \left( \delta_{e,0} + \frac{2J\bar{c}}{\bar{q}S} C_{\mathcal{M}\delta_e}^{-1} (K_q e_q - \dot{q}_{I,0}) \right). \quad (4-16)$$

By combining (4-15) with the incremental control step in (4-16), control actions can be allocated such that the desired pitching moment is achieved and the induced generalized symmetric forces by the control actions is minimized.

$$\begin{bmatrix} \delta_{fo} \\ \delta_{fm} \\ \delta_{fi} \\ \delta_e \end{bmatrix} = \begin{bmatrix} \delta_{fo,0} \\ \delta_{fm,0} \\ \delta_{fi,0} \\ \delta_{e,0} \end{bmatrix} + \begin{bmatrix} C_{n1\delta_{fo}} & C_{n1\delta_{fm}} & C_{n1\delta_{fi}} & C_{n1\delta_e} \\ C_{n2\delta_{fo}} & C_{n2\delta_{fm}} & C_{n2\delta_{fi}} & C_{n2\delta_e} \\ C_{n3\delta_{fo}} & C_{n3\delta_{fm}} & C_{n3\delta_{fi}} & C_{n3\delta_e} \\ C_{\mathcal{M}\delta_{fo}} & C_{\mathcal{M}\delta_{fm}} & C_{\mathcal{M}\delta_{fi}} & C_{\mathcal{M}\delta_e} \end{bmatrix}^{-1} \begin{bmatrix} 0 \\ 0 \\ 0 \\ 1 \end{bmatrix} \frac{2J\bar{c}}{\bar{q}S} K_q (e_q - \dot{q}_{I,0}). \quad (4-17)$$

Looking at Figure 4-4, one can observe that the ICA method results in less system dynamics increments and a reduced oscillation of the elevator compared to INDI without ICA. Still, it should be noted that the simulations rely on a perfectly-known aerodynamic and structural model that is linear in the control effectiveness coefficients. In reality, however, this control effectiveness matrix is often dependent on the state and input in a nonlinear fashion. This is especially relevant for large flexible aircraft where in-flight deformations can change the vehicle's moment inertia and local angle of attack values. In theory, one can account for this by updating the direction of the nonlinear control effectiveness using partial derivatives of known analytical models. As no such analytical model is available and to account for parametric uncertainties and unmodelled dynamics, an adaptive INDI controller will be considered to estimate the control effectiveness coefficients online.

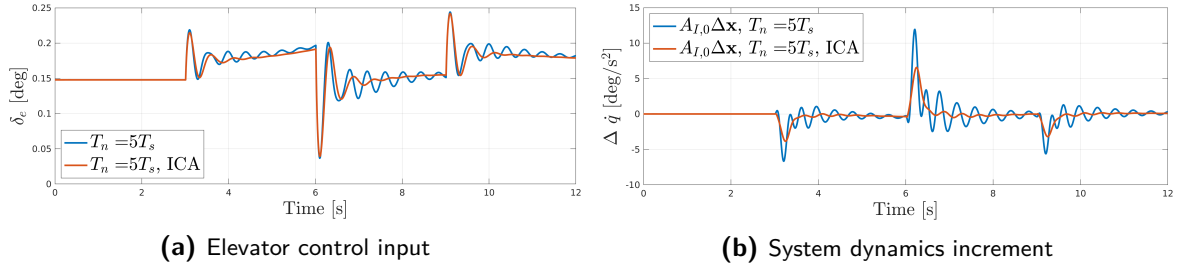


**Figure 4-4:** The incremental control allocation method compared against the nominal INDI control case for a time delay with  $n = 5$

### Adaptive incremental control allocation

To remove the dependency on the control effectiveness in the proposed incremental control laws, online estimation of the control effectiveness will be considered. This online estimation in the incremental control law is known as adaptive incremental nonlinear dynamic inversion and has already found its application in the control of quadcopters in [21]. The core of the adaptation law is described by the following definition:

$$B_{I,0}(k) = B_{I,0}(k-1) - U_2(B_{I,0}(k-1)\Delta\mathbf{u}_0 - \Delta\dot{\mathbf{x}}_{I,0})\Delta\mathbf{u}_0^T U_1. \quad (4-18)$$

Here,  $U_1$  and  $U_2$  are diagonal matrices that contain the adaptation constants for the control inputs and the control variables, respectively. When considering the pitch dynamics only, notice that the  $C_{M_{\delta_e}}$  is updated through this adaptation. Since a negative  $C_{M_{\delta_e}}(k-1)\Delta\delta_{e,0} - \Delta\dot{q}$  will increase  $C_{M_{\delta_e}}(k)$ , more interaction between the elevator and the structural dynamics is expected. To reduce this interaction, another signal that measures the symmetric wing bending will be explored in the adaptation law. In most adaptive INDI applications, such an additional control variable is often directly controlled towards the desired reference. In this control problem however, no reference generation algorithm is available and the additional control variable will only be used to update the control effectiveness matrix for the allocation step.

$$\begin{bmatrix} \delta_{f_0} \\ \delta_e \end{bmatrix} = \begin{bmatrix} \delta_{f_0,0} \\ \delta_{e,0} \end{bmatrix} + \underbrace{\begin{bmatrix} C_{n_1\delta_{f_0}} & C_{n_1\delta_e} \\ C_{M_{\delta_{f_0}}} & C_{M_{\delta_e}} \end{bmatrix}^{-1}}_G \begin{bmatrix} 0 \\ 1 \end{bmatrix} \frac{2J\bar{c}}{qS} K_q (e_q - \dot{q}_{I,0}). \quad (4-19)$$

Note that this control law has a reduced amount of control actions compared to the allocation method of (4-17). The choice for controlling the symmetric bending mode with the outer flap relies on the assumption that less control surface deflection is required for achieving certain effectiveness. The reason for not including more control actions is explained by the difficulty of real-time estimating the modal accelerations for each symmetric structural mode. Such estimation is often concerned with feeding many sensor data points though extensive least squares and Kalman filtering techniques [36]. Since the implementation of such a filter is outside the scope of this thesis, a simplified linear estimation will be considered for analyzing the effectiveness of this adaptive allocation method.

This filtering technique seeks to find an estimate of the first symmetric bending mode acceleration by simplifying and linearizing the equations of the virtual accelerations at both

wingtips. For this estimate, consider again the virtual and vertical acceleration from (3-15) of the left wingtip:

$$a_{z,wL} = \underbrace{a_{z,cg} + x_{wL}(pr - \dot{q}) + y_{wL}(qr + \dot{p}) - z_{wL}(p^2 + q^2)}_{\text{rigid-body}} + \sum_{i=1}^{n_F} \Phi_{z_i}^{wL} \ddot{\eta}_i \quad (4-20)$$

By neglecting the angular rate cross-terms, subtracting the rigid-body contribution from the measurement, dividing the result by the corresponding modeshapes and averaging both wing tip contributions, the following model acceleration estimate can be obtained:

$$\hat{\eta}_1 \approx \frac{1}{2\Phi_{z_1}^{wL}} (a_{z,wL} - a_{z,cg} + x_{wL}\dot{q}_0 - y_{wL}\dot{p}_0) + \frac{1}{2\Phi_{z_1}^{wR}} (a_{z,wR} - a_{z,cg} + x_{wR}\dot{q}_0 - y_{wR}\dot{p}_0). \quad (4-21)$$

Where  $\dot{p}_0$  and  $\dot{q}_0$  are the finite difference approximation of the filtered angular rates that are also contained in the vector  $\hat{\mathbf{x}}_{I,0}$ . Note that the accelerations  $a_{z,w}$  and  $a_{z,cg}$  are filtered with the same filter to attenuate noise and synchronize the phase lag. Consequently, using (4-18) the following update for the control effectiveness matrix  $G$  in (4-18) can be specified:

$$\begin{bmatrix} C_{n_1\delta_{fo}}^k & C_{n_1\delta_e}^k \\ C_{\mathcal{M}\delta_{fo}}^k & C_{\mathcal{M}\delta_e}^k \end{bmatrix} = \begin{bmatrix} C_{n_1\delta_{fo}}^{k-1} & C_{n_1\delta_e}^{k-1} \\ C_{\mathcal{M}\delta_{fo}}^{k-1} & C_{\mathcal{M}\delta_e}^{k-1} \end{bmatrix} - U_1 \left( \begin{bmatrix} C_{n_1\delta_{fo}}^{k-1} & C_{n_1\delta_e}^{k-1} \\ C_{\mathcal{M}\delta_{fo}}^{k-1} & C_{\mathcal{M}\delta_e}^{k-1} \end{bmatrix} \begin{bmatrix} \Delta\delta_{fo,0} \\ \Delta\delta_{e,0} \end{bmatrix} - \begin{bmatrix} \Delta\hat{\eta}_1 \\ \Delta\dot{q}_0 \end{bmatrix} \right) \begin{bmatrix} \Delta\delta_{fo,0} \\ \Delta\delta_{e,0} \end{bmatrix}^T U_2. \quad (4-22)$$

Here, the superscript  $k$  denotes the discrete-time instance and the diagonal entries in  $U_1$  and  $U_2$  are containing the adaptation constant for control variable estimates and inputs, respectively. Since the estimate of (4-21) still includes some of the contributions from the second and third symmetric bending modes, the effectiveness coefficient for  $n_1$  are assumed to be less constant in time than the control effectiveness coefficient for  $\mathcal{M}$ . Based on this assumption, the selected adaptation constants for the pitching moment are smaller than for the generalized load:

$$U_1 = \text{diag} [0.1 \quad 0.001], \quad U_2 = \text{diag} [1 \quad 0.1]. \quad (4-23)$$

For this adaptation constants, the resulting elevator response and system dynamics increments of this adaptive incremental allocation method are plotted in Figure 4-5a and Figure 4-5b. Looking at these figures, it can be seen that the Adaptive Incremental Control Allocation

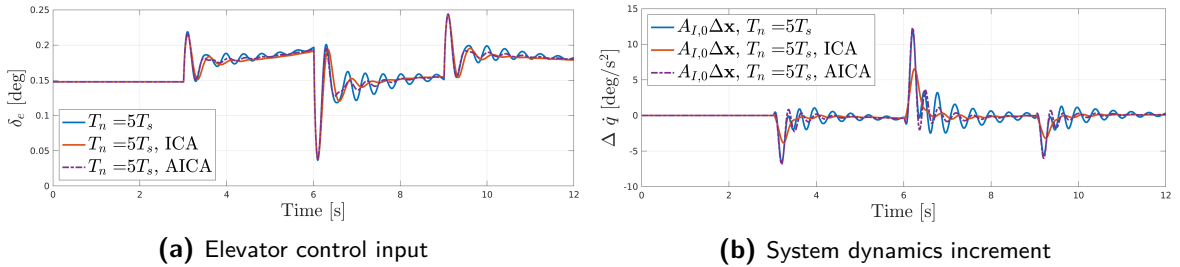


**Figure 4-5:** The Adaptive Incremental Control Allocation (AICA) method compared against previously discussed ICA and the nominal INDI controller with a time delay of  $n = 5$

(AICA) method reduces the oscillations in the elevator input and the system dynamics increments when comparing it against the nominal INDI control case. Still, the ICA outperforms

the AICA method due to the exact cancellation of the control effectiveness contribution and the utilization of more control surfaces. It should be noted, that the choice of the adaptation constants in  $U_1$  and  $U_2$  are determining the stability of this adaption law and that increasing these constants can jeopardise the controller its stability. This is especially relevant when considering that aerodynamic disturbances such as wind gust and turbulence can influence the convergence of this adaption law. Although the theoretical limit of these gains depend on the auto-correlation matrix of the input [21], a formal systematic stability proof of nonlinear adaptive controllers is still to be found [37].

#### 4-1-5 Intermediate conclusions

Up to this point, we have analyzed the angular rate tracking performance of INDI control applied to the flexible SB-10 glider. From this analyses, we can conclude that the unfavourable aeroservoelastic effects degrade when time delays and phase lags are increased. To explain the performance deterioration and to compensate for it accordingly, the following can be concluded:

- Subjecting time delays and phase lags to the INDI control method will result in oscillating behaviour of both the rigid and structural motions responses as well as the computed control input. These oscillations originate from responding to a delayed measurement with a sign and magnitude corresponding to only the rigid pitching moment coefficient  $C_{M\delta_e}$ . In theory, the pitching moment is also influenced by the motion of structural modes which in this context is not accounted for by the nonlinear inversion part in the controller. Instead, due to their specific fastness and the delayed measurement, these structural dynamics enter the system dynamics term  $A_0\Delta\mathbf{x}$  and oscillations occur.
- A way to accommodate for these dynamics is through not neglecting the  $A_0\Delta\mathbf{x}$  term. However, the computation of the  $\Delta\mathbf{x}$  term requires knowledge of all the structural states which in practice requires computationally extensive filtering techniques. As the development of such online estimation techniques is outside of the scope of this thesis, suitable control allocation is examined.
- With the current model, linear incremental control allocation seems to be promising for reducing the interactions between the controller and the structural dynamics increments. Note that this is only valid when assuming no uncertainties and exact cancellation of the control effectiveness contribution. As this is often not the case in reality, an adaptive incremental control allocation method is considered to update the control effectiveness matrix. Although this method is beneficial in terms of reducing model dependency, its stability in the presence of time delays and aerodynamic disturbances remains inadequate when considering its implementation on a flexible and fixed-wing aircraft.

The next section, therefore, introduces a more conservative approach for reducing the oscillations in closed-loop INDI responses. This approach relies on local linear stability tools and seeks to improve aerodynamic disturbance rejection and structural motion alleviation without neglecting phase lags and time delays.

## 4-2 Symmetric wing bending alleviation using $\mathcal{H}_\infty$ synthesis

In this section, the INDI controller will be augmented with a linear state space controller that reduces the oscillation of the response in the presence of time delays and aerodynamic disturbances. This state-space controller is found by utilizing the mixed sensitivity  $\mathcal{H}_\infty$  norm minimization similar as presented in [8] and [9]. Here, a state-space controller is synthesized to suppress flutter without incorporating the closed-loop effect of a rigid-body controller. In this work, however, the closed-loop response of the INDI controller is incorporated in a  $\mathcal{H}_\infty$  synthesis to improve tracking and to reduce symmetric wing bending motions.

The benefit of blending the INDI control structure in this synthesis method is that the effect of aeroservoelastic coupling and time delays can be included. Accordingly, a state-space controller can be synthesized to alleviate the oscillating system dynamics increments in INDI-based control. The overall control structure that will be analysed throughout this chapter is illustrated in Figure 4-6. Note that the outboard flaps are added to reduce the oscillation while

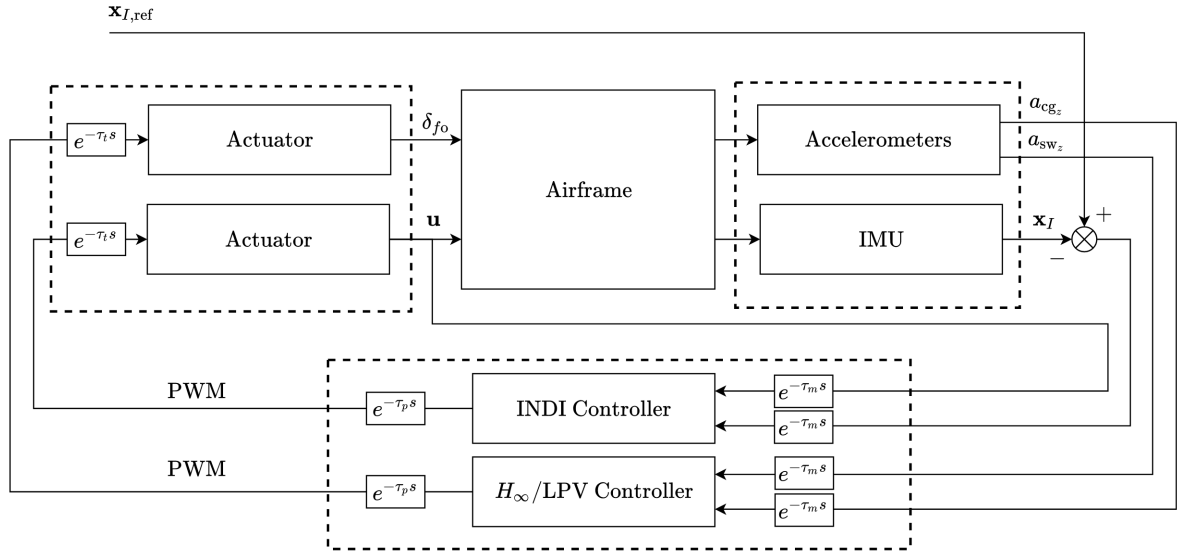


**Figure 4-6:** Overall pitch rate control structure with INDI angular rate control and linear  $\mathcal{H}_\infty$  control

the other control surfaces are reserved for roll, pitch and yaw control by INDI. Furthermore, the signals are delayed to realistically model the implementation of the controller on real hardware. Three types of delays will be considered in this context:

- **Measurement delay:** The measurement delay, indicated by  $\tau_d$ , denotes the time it takes to receive the measurements from on-board sensors. In existing autopilot software these measurements are often filtered and synchronized. As such, the same measurement delay will be considered for all received sensor information.
- **Process delay:** The process delay, defined by  $\tau_m$ , is the time the flight computer requires for processing the flight control algorithm. In simulation, this delay is added to the output of the controller, i.e. the input to the plant.

- **Transport delay:** The transport delay, specified as  $\tau_p$ , is an additional latency to the process delay and represents the delay of the actuator.

To incorporate these delays in the linear  $\mathcal{H}_\infty$  optimization, the nonlinear model 3-13 is linearized and discretized in 4-2-1. Thereafter, the problem is reformulated as a multi-objective  $\mathcal{H}_\infty$  optimization to minimize the closed-loop structural frequency peaks.

#### 4-2-1 Synthesis model

The goal of this subsection is to describe and model the closed-loop INDI response in the required framework for  $\mathcal{H}_\infty$  synthesis. Since the closed-loop INDI performance is affected by time delays as shown in the previous section, the question arises whether the design should be carried out in continuous time or in discrete-time. Although time delays can be approximated through pade approximations in continuous time, the corresponding increase in model order can be limited in  $\mathcal{H}_\infty$  synthesis. Furthermore, through considering that INDI control is sampled when implemented, it is preferred to carry out the synthesis in discrete-time to obtain a directly real-time implementable controller. Before describing how a sampled data system can be derived, first, the continuous-time linear model will be introduced.

##### Linear elastic airframe model

As the  $\mathcal{H}_\infty$  control synthesis is a linear optimization, the nonlinear model 3-13 is linearized around multiple trim points across different airspeeds using the method described in A-2. With symmetric structural motions being most dominantly present, only pitching motions will be considered. As such, the following state-space representation will be used to model the dynamics of the airframe:

$$\dot{\mathbf{x}}_s = A_s \mathbf{x}_s + B_s \mathbf{u}_s \quad \text{and} \quad \mathbf{y}_s = C_s \mathbf{x}_s + D_s \mathbf{u}_s. \quad (4-24)$$

Here, the subscript  $s$  indicates that only symmetric states and inputs are included. Subsequently, the state and input vector can be described by

$$\mathbf{x}_s = \left[ u \quad \alpha \quad \theta \quad q \quad \eta_1 \quad \dot{\eta}_1 \quad \eta_2 \quad \dot{\eta}_2 \quad \eta_3 \quad \dot{\eta}_3 \right]^T \quad \text{and} \quad \mathbf{u}_s = \left[ \delta_e \quad \delta_{f_0} \quad \Delta\alpha_d \right]^T. \quad (4-25)$$

Note that the angle of attack disturbance,  $\Delta\alpha_d$ , is modelled as a forcing function to the state-space model by augmenting  $\Delta\alpha_d$  to the input and extending the input matrix  $B_s$  with a copy of the second column of  $A_s$ . As such, the system will respond to  $\Delta\alpha_d$  as it would to  $\alpha$  [30]. To model the accelerations at the wing tip locations, the row vectors in  $A_s$  and  $B_s$  of  $\dot{\eta}_1$ ,  $\dot{\eta}_2$  and  $\dot{\eta}_3$  are multiplied with their corresponding mode shapes and included in  $C_s$  and  $D_s$ . Accordingly, the left and right wingtip accelerations are averaged as only symmetric motions are considered. As a result, the output vector will be defined as

$$\mathbf{y}_s = \begin{bmatrix} q \\ a_{z,S} \end{bmatrix}^T \quad \text{with} \quad a_{z,S} = \frac{1}{2}a_{z,wL} + \frac{1}{2}a_{z,wR} - a_{z,cg}. \quad (4-26)$$

In addition to the measurable states, non-measurable states will be utilized in the subsequent sections to reduce the oscillations in the responses. These additional performance outputs

are introduced by the variable  $\mathbf{z}_s = C_z \mathbf{x}_s$ . Here, the modal velocities of the first and second structural modes are selected as performance measures. To keep consistent with the notation throughout this section, these variables are partitioned to the measurable outputs in an equivalent transfer function representations through  $F(s) = \begin{bmatrix} F_z(s) & F_y(s) \end{bmatrix}^T$ .

### Discrete equivalent of linear a INDI controller

To carry out  $\mathcal{H}_\infty$  in discrete time, an equivalent sampled data system of the INDI control loop should be derived. To arrive at a complete sampled data system of both continuous and discrete-time transfer functions, samplers and zero-order hold transfer functions are included in INDI control scheme as illustrated in Figure 4-7. Here, the second-order filter  $H(z)$  is

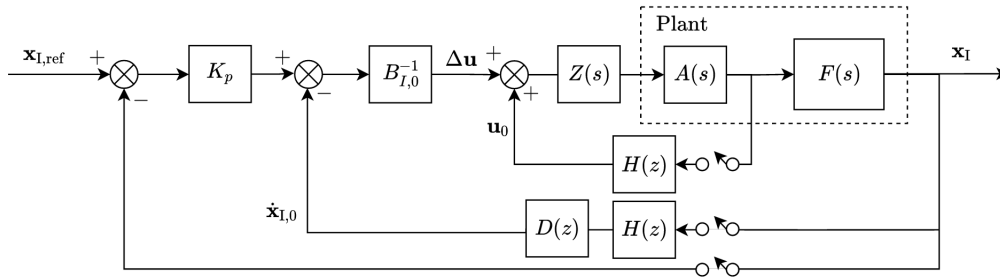


**Figure 4-7:** INDI control scheme with a discrete-time finite difference approximation, second order washout filter, actuator model and a proportional linear control gain  $K_p$

obtained through discretizing (4-8) using the Tustin approximation. Furthermore, the discrete signals that are sampled with  $T_s$  are converted to continuous signals through the multiplication with  $Z(s)$ . This transfer function, together with the first order actuator model  $A(s)$ , and the finite difference approximation  $D(z)$ , are defined through

$$Z(s) = \frac{1 - e^{-sT_s}}{s}, \quad A(s) = \frac{\omega_a}{s + \omega_a}, \quad D(z) = \frac{z - 1}{T_s z}. \quad (4-27)$$

Grouping the continuous time transfer functions together and placing samplers in front and behind their corresponding blocks permits the use of zero order hold discretization. This rearranging is illustrated in figure 4-8. Finally, by discretizing the transfer functions in between

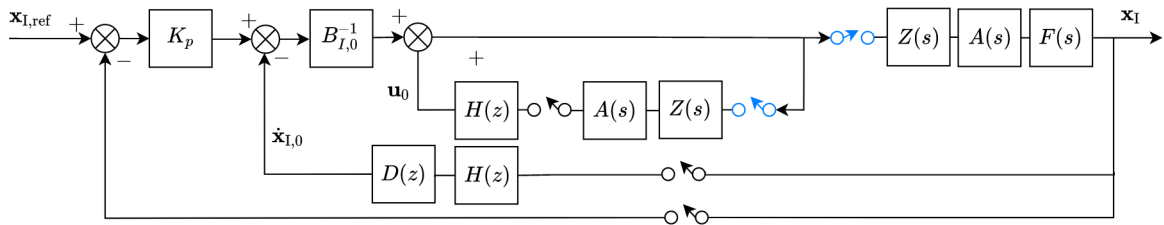


**Figure 4-8:** INDI control scheme in which the continuous time transfer functions are separated from the discrete time functions using samplers

the samplers using the zero order hold method a complete sampled data system for  $\mathcal{H}_\infty$  can be obtained. To motivate the selection of the 100 Hz sampling rate used in Table 4-1, the

stability margins of the closed-loop system has been simulated for various sampling times, proportional gains  $K_p$  and actuator bandwidths in Figure 4-9. Here, it is confirmed that low

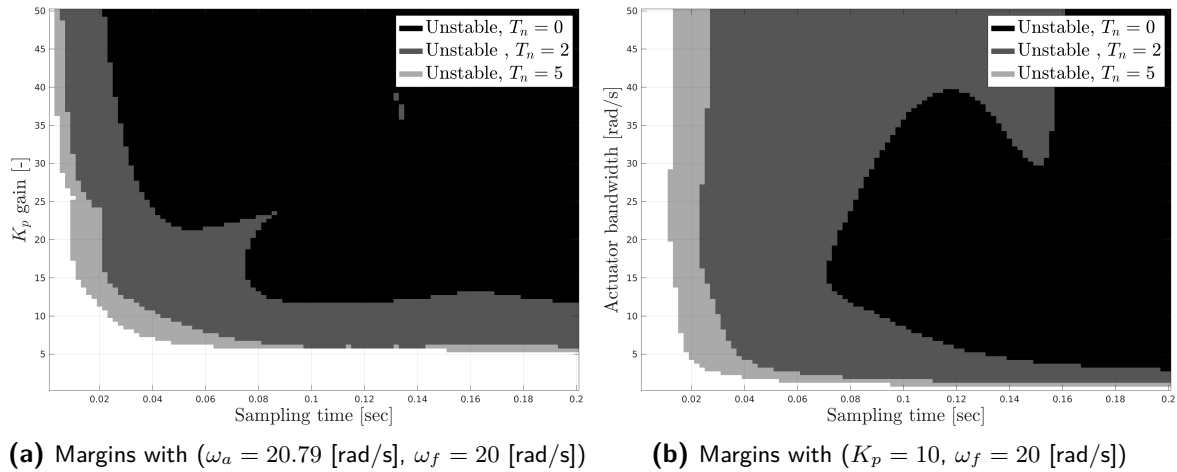


**Figure 4-9:** Stability margins for various sampling times, proportional gains and actuator bandwidths when subjected to different incremental time delays

sampling times and low proportional gains are guaranteeing stability in the presence of time delays. However, higher gain settings may be required in cases where better tracking should be achieved. This is especially relevant for a glider, where potential energy is continuously lost and a maximum amount of manoeuvres should be performed within limited flight time. In this context, the next subsection seeks to increase these stability margins for specific INDI proportional gain and time delay configurations. For this, the discretized transfer functions in Figure 4-8 will be denoted by  $\mathcal{Z}\{ZA(s)\}$  and  $\mathcal{Z}\{ZA(s)F(s)\}$ .

#### 4-2-2 Mixed sensitivity framework with INDI

In this subsection, the generalized interconnection required for the  $\mathcal{H}_\infty$ -norm minimization will be derived. Similar as in Section 2-3-1, this generalized scheme includes multiple input and output channels that can be weighted according to some desired performance requirements. For the control problem at hand, these desired input-output performance characteristics are defined as follows:

- Achieve pitch rate tracking of  $q_{\text{ref}}$  with a fastness that is specified by the linear controller and the control effectiveness in the INDI controller.
- Reject output disturbances on the wing tip acceleration measurements and the pitch rate measurements that are generated by the von Kármán model.
- Reject perturbations on the angle of attack, denoted by  $\Delta\alpha_d$  and defined by the vertical and horizontal wind components from the von Kármán model.

The goal is to achieve all these performance characteristics while also reducing the energy in the symmetric wing bending motions and control activity. The reduction of this energy is translated to minimizing the frequency peaks of the first and second modal velocities. As



Furthermore, to ensure that the pitch rate is controlled with the elevator using INDI and to provide wingtip accelerations feedback to the linear controller  $K_h(z)$ , the other matrices in Figure 4-10 are defined as:

$$G_2^{-1} = \begin{bmatrix} G^{-1} & 0 \\ 0 & 1 \end{bmatrix}, \quad D_2(z) = \begin{bmatrix} D(z) & 0 \\ 0 & 0 \end{bmatrix}, \quad H_2(z) = \begin{bmatrix} H(z) & 0 \\ 0 & 0 \end{bmatrix}.$$

Using this, the transfer functions in (4-28) from the input channels to the control input can be defined:

$$\begin{aligned} N_{\mathbf{d}_s}^{\mathbf{b}_s}(z) &= G_2^{-1} A_L(z) H_2(z) D_2(z) (I + G_2^{-1} A_L(z) H_2(z) D_2(z) \mathcal{Z}\{Z A_2(s) F_y(s)\})^{-1} \\ N_{\alpha_d}^{\mathbf{b}_s}(z) &= (I + G_2^{-1} A_L(z) H_2(z) D_2(z) \mathcal{Z}\{Z A_2(s) F_y(s)\})^{-1} \\ N_{\mathbf{u}_e}^{\mathbf{b}_s}(z) &= G_2^{-1} A_L(z) (1 + G_2^{-1} A_L(z) H_2(z) D_2(z) \mathcal{Z}\{Z A_2(s) F_y(s)\})^{-1} \end{aligned} \quad (4-31)$$

Similarly, the loop transfers to the performance channels are obtained through:

$$\begin{aligned} N_{\mathbf{d}_s}^{\mathbf{z}_s}(z) &= (I + \mathcal{Z}\{Z A_2(s) F_z(s)\} A_L(z) G^{-1} D_2(z) H_2(z))^{-1} \\ N_{\alpha_d}^{\mathbf{z}_s}(z) &= \mathcal{Z}\{Z A_2(s) F_z(s)\} (I + G_2^{-1} A_L(z) H_2(z) D_2(z) \mathcal{Z}\{Z A_2(s) F_y(s)\})^{-1} \\ N_{\mathbf{u}_e}^{\mathbf{z}_s}(z) &= \mathcal{Z}\{Z A_2(s) F_z(s)\} A_L(z) G_2^{-1} (I + \mathcal{Z}\{Z A_2(s) F_z(s)\} A_L(z) G^{-1} D_2(z) H_2(z))^{-1}. \end{aligned} \quad (4-32)$$

The relation between the input channels to the measurable channels are calculated by:

$$\begin{aligned} N_{\mathbf{d}_s}^{\mathbf{y}_s}(z) &= (1 + \mathcal{Z}\{Z A_2(s) F_y(s)\} A_L(z) G_2^{-1} D_2(z) H_2(z))^{-1} \\ N_{\alpha_d}^{\mathbf{y}_s}(z) &= \mathcal{Z}\{Z A_2(s) F_y(s)\} (I + G_2^{-1} A_L(z) H_2(z) D_2(z) \mathcal{Z}\{Z A_2(s) F_y(s)\})^{-1} \\ N_{\mathbf{u}_e}^{\mathbf{y}_s}(z) &= \mathcal{Z}\{Z A_2(s) F_y(s)\} A_L(z) G_2^{-1} (I + \mathcal{Z}\{Z A_2(s) F_y(s)\} A_L(z) G_2^{-1} D_2(z) H_2(z))^{-1}. \end{aligned} \quad (4-33)$$

Finally, the closed loop transfer function is acquired through applying the linear fractional transformation of (2-27):

$$\mathcal{F}_L(P, K) = \begin{bmatrix} 0 & W_u N_d^b(z) & W_u N_\alpha^b(z) \\ 0 & W_z N_d^z(z) & W_z N_\alpha^z(z) \\ 0 & W_y N_d^y(z) & W_y N_\alpha^y(z) \end{bmatrix} + \begin{bmatrix} N_u^b(z) \\ N_u^z(z) \\ N_u^y(z) \end{bmatrix} K(z) (I + N_u^y K(z))^{-1} \begin{bmatrix} W_r & -N_d^y & N_\alpha^y \end{bmatrix}. \quad (4-34)$$

As the fastness of the rigid-body response is to be specified by the INDI control gain and the oscillations should be reduced by the synthesised controller, a decoupled control structure will be considered for  $K(z)$ . As such, the structure of  $K(z)$  is predefined as a diagonal matrix with its first element filled with the INDI control gain and its second element with the frequency-dependent controller  $K_h(z)$ :

$$K(z) = \begin{bmatrix} K_p & 0 \\ 0 & K_h(z) \end{bmatrix}. \quad (4-35)$$

Accordingly, the  $\mathcal{H}_\infty$ -norm minimization of (2-26) can be performed to find a stable and linear controller for  $K_h(z)$ . Note that the controller found through the conventional  $\mathcal{H}_\infty$  algorithm, presented in Section B-1, will have the same number of states as the generalized plant. This implies that when disregarding the presence of time delay, the size of the obtained controller will be 16, i.e. 10 states from the model, 1 from the actuator, 2 from the filter  $H(z)$ , 2 from the frequency-dependent weighing function  $W_u(z)$  and 1 from the derivative operator  $D(z)$ .

Since one of the objectives is to also account for different time delays, additional states are added at the green, blue and red dots in the generalized plant of Figure 4-10. Consequently, higher order controllers will be obtained when using the conventional  $\mathcal{H}_\infty$  algorithm. As this will increase the computational load of the controller on real hardware, a low system order should be acquired. Fortunately, additional structural constraints can be imposed on the controller by using specialized non-smooth optimization techniques as proposed in [38] and [39]. In this thesis, these techniques are used in MATLAB to acquire a controller with a system order of 9, that according to [5] can be real-time implemented. The next paragraph will investigate whether the augmentation of this controller can improve the pitch rate response and reduce structural interactions.

**Performance illustration:** To evaluate whether the oscillations in the pitch rate response are alleviated by the augmented  $\mathcal{H}_\infty$  controller, a simulation is performed. Note that this simulation will only be illustrative and that a more numeric verification will be provided in Section 5-1. For this illustrative purpose, the same nominal simulation condition will be considered as in Table 4-1. Therefore, the same incremental time delay on the controller output of  $\tau_p = 5$  samples will be included in the synthesis model to reproduce the oscillation of system dynamics increments. To reduce these oscillations with the augmented  $\mathcal{H}_\infty$  controller, the input weights are tuned to

$$W_r = \begin{bmatrix} 1 \\ 0 \end{bmatrix}, \quad W_d = \begin{bmatrix} 1 & 0 \\ 0 & 1 \end{bmatrix}, \quad W_\alpha = \begin{bmatrix} 0 \\ 0 \\ 0.2 \end{bmatrix}. \quad (4-36)$$

While the output weights are set to

$$W_u = \begin{bmatrix} 0 \\ W_u(z) \end{bmatrix}, \quad W_z = \begin{bmatrix} 0.04 & 0 \\ 0 & 0.06 \end{bmatrix}, \quad W_y = \begin{bmatrix} 0.05 & 0 \\ 0 & 0 \end{bmatrix}. \quad (4-37)$$

Note that the second structural mode is penalized more in  $W_z$  than the first structural mode due to its lower damping i.e. Figure 3-7b. The weighing matrix on the disturbance channel  $W_d$  is set to identity to normalize the input-output relations. The frequency-dependent output function in  $W_u$  is inspired by [9] and configures a band-pass filter centered around the natural frequency of the first and second structural modes. The continuous time representation of this filter is defined by

$$W_u(s) = 2.1 \frac{s^2 + 10s + 40}{s^2 + 100s + 40}, \quad (4-38)$$

and the Tustin approximation is used to find the discrete-time equivalent  $W_u(z)$ . For illustrative purposes, its corresponding frequency response is visualized in Figure 4-11a. By incorporating these input-output weights accordingly and finding  $K(z)$  through minimizing (4-34), the closed-loop resonance peak of the control system interacting with the second structural mode can be reduced. This is shown in Figure 4-11b.

This alleviation in pitch rate oscillation is also confirmed by looking at Figure 4-12. Here, a pitch rate doublet response of the INDI controller with the synthesized  $K(z)$  is simulated using the nonlinear model. Clearly, the oscillations in both the pitch rate and the elevator control input are reduced by the addition of the synthesised controller  $K(z)$ .

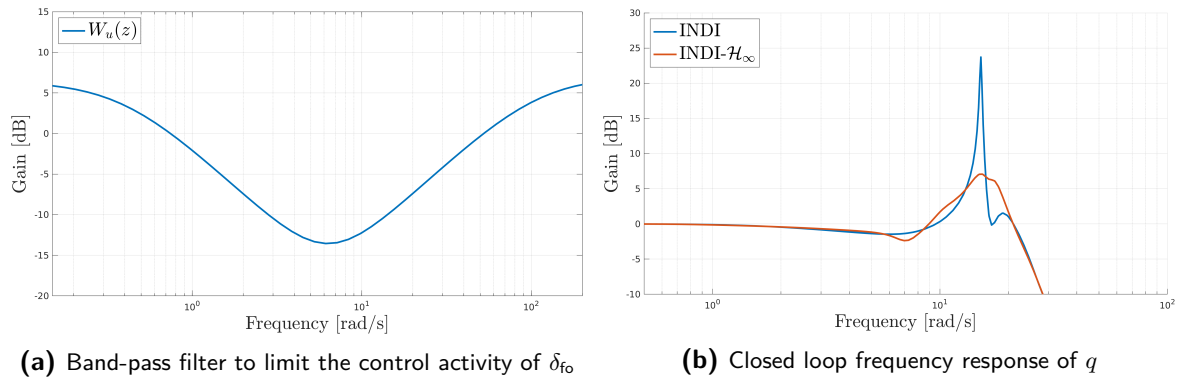


**Figure 4-11:** Frequency response of the weighted output function  $W_u(z)$  on the left and the closed loop pitch rate response on the right

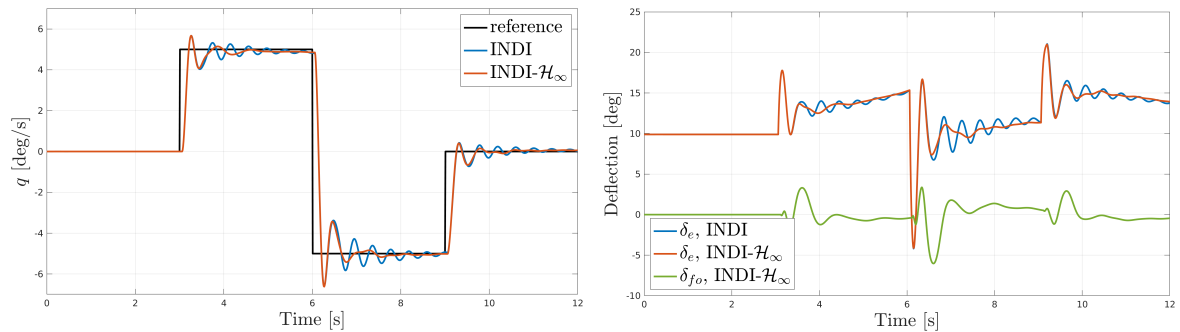


**Figure 4-12:** Doublet response of  $q$  for both the INDI and INDI- $\mathcal{H}_\infty$  controller in the left figure and corresponding control surfaces deflections in the right figure

Two things should be noted here. First, this synthesis formulation does not account for actuator saturation. Second, the time delays are assumed to be synchronized and constant in time. As this not always the case in reality, the concept of pseudo control hedging will be adapted to this framework.

### 4-2-3 Synthesis with Pseudo Control Hedging

As stated in [27] and Section 2-2-2, Pseudo Control Hedging (PCH) can be utilized for two reasons. First, PCH can shift the region of adequate performance towards a surplus of delays  $\mathbf{x}_0$  when PI-control and P-control is used for the design of the reference model and the virtual control input, respectively. Second, PCH can be used as an anti-windup technique by selecting P-control for the reference model and P(I)-control for the virtual control input. In both control configuration, the closed-loop frequency response of the rigid-body and structural dynamics is affected. To account for this effect, PCH will be included in the synthesis formulation.

The inclusion of the PCH structure in the generalized plant is illustrated in Figure 4-13. Here, the fixed P or PI control structure of the reference model is denoted by  $K_r(z)$  while the control structure for the virtual control input is defined by  $K_p(z)$ . Through performing a similar derivation as in the previous subsection, the closed-loop transfer functions can be obtained and minimized using the  $\mathcal{H}_\infty$  algorithm. This derivation with the resulting weighted

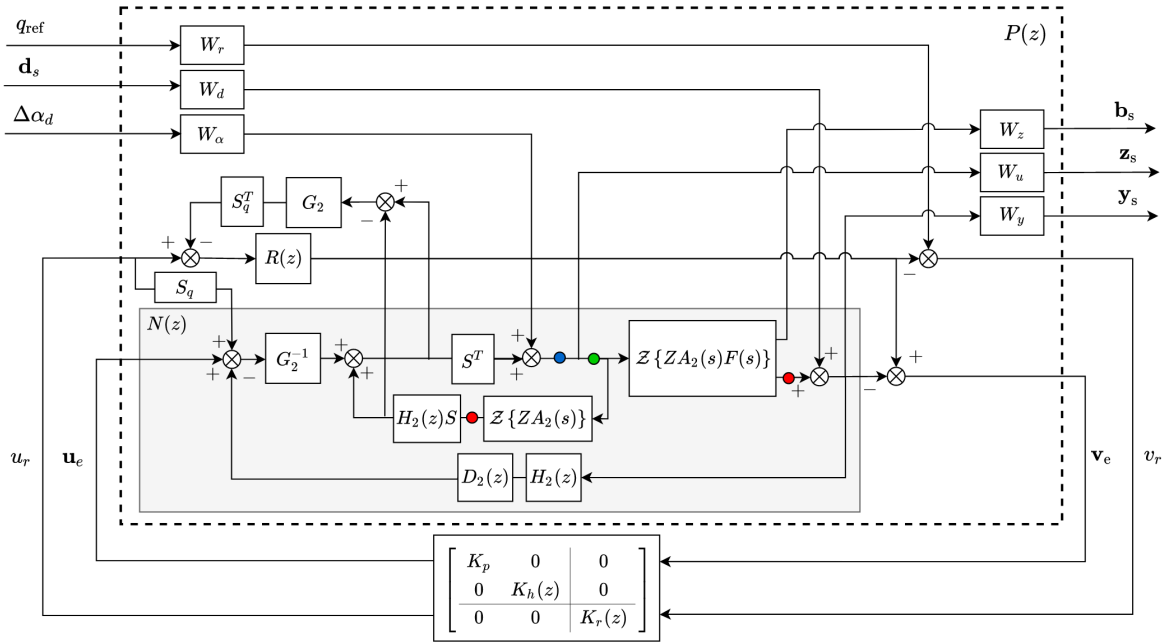


**Figure 4-13:** Generalized interconnection for synthesising the linear controller  $K(z)$  with the INDI-PCH control included using a mixed sensitivity  $\mathcal{H}_\infty$ -norm minimization. Similar as in 4-10 the blue, green and red dots indicate the process, transport and measurement delay respectively.

matrix multiplication is provided in Appendix B-2. Based on the configured control structure of  $K_p(z)$  and  $K_r(z)$ , the inputs and output weights may be tuned differently to achieve the required performance characteristics.

An important remark regarding the blending of INDI and  $\mathcal{H}_\infty$  is that the obtained linear controller  $K(z)$  only provides satisfactory performance in the vicinity of its corresponding linear operating point. Therefore, the next subsection will elaborate upon suitable scheduling techniques to achieve better performance across various aerodynamic dampening conditions of the structural dynamics.

#### 4-2-4 Scheduled structural motion alleviation controller

Contrary to INDI control, where continuous input-output linearization is performed through measured feedback,  $\mathcal{H}_\infty$  control synthesis has to be performed on an individual linear operating point. As such, in order to benefit from the  $\mathcal{H}_\infty$  control augmentation, multiple single-point controllers have to be designed and scheduled across different aerodynamic loading conditions to guarantee stability and structural motion alleviation. To this end, two scheduling techniques will be considered:

- **Linear Parameter Varying (LPV) control** automates the  $\mathcal{H}_\infty$  synthesis procedure over the entire range of varying parameters by treating the parameter-dependent plant as a single entity. In this respect, this method could preserve stability and robustness over the entire range of varying aerodynamic and structural parameters. Two main drawbacks arise when considering this technique for the developed mixed sensitivity framework. First, according to techniques provided in [14], no predefined control

structure can be incorporated within the LPV optimization. As a consequence, the system order of the obtained controller is thus equal to the generalized plant and has to be reduced to be real-time implementable. Second, no discrete-time systems can be solved with the proposed LPV optimization [14] yet and the benefit of including multiple discrete time delays without using high order approximations impairs. Since model reduction methods of either the generalized plant or the obtained controller are outside the scope of this thesis, simple scheduling through interpolation techniques can be considered instead.

- **Interpolation** is often used in various flight control applications to achieve adequate performance across the flight envelope of interest. Contrary to LPV, control scheduling through interpolation cannot ensure both nominal and robust performance in between the gridded design points. For the application in this thesis, in which a linear model of the structural dynamics is used, a piece-wise linear interpolation that is inspired by [8] can be considered.

However, before utilizing this interpolation technique, first, the overall performance improvements of a single-point controller will be evaluated. In this respect, no scheduling will be considered and the focus of the remainder of this thesis is oriented around evaluating the benefit of the INDI- $\mathcal{H}_\infty$  concept in general. As such, a worst-case operating point will be selected as a design point in the sequel of this thesis. This worst-case operating point is defined at the airspeed at which most interaction between the control system and the structural dynamics is expected. With reference to Figure 3-7a, this point is at 40 m/s, the airspeed with the first structural mode frequency closest to the natural frequency of the short period dynamics.

#### 4-2-5 Intermediate conclusions

In this section, the unfavourable interactions between INDI control and the aeroelastic dynamics have been modelled in a multi-objective design formulation to find a linear  $\mathcal{H}_\infty$  controller that reduces the motions in the control input and the structural response. Contrary to the incremental control allocation techniques presented in the previous section, this developed synthesis method allows for the compensation of oscillating behaviour caused by time delays and phase lags. For implementing this control structure, the following has to be considered:

- Although PCH can be applied to prevent actuator saturation of the elevator, it should be noted that the saturation of the outboard flap is not handled by the  $\mathcal{H}_\infty$  synthesis. Despite this, the outboard flap will most likely not saturate that often as high-frequency signals or spikes in the acceleration measurements are not transferred to the actuator commands due to the limited control activity region. Furthermore, biases in the centre of gravity and wingtip acceleration measurements should be removed to achieve the best performance.
- One of the current limitation of the developed control synthesis procedure, is that adequate performance across the flight envelope of interest cannot yet be guaranteed. Only the performance of the the additional  $K(z)$  controller will be evaluated under the assumption that the flexibility effects are not changing substantially across the tested

flight conditions. This conflicts with the scheduling benefit of INDI-based control and impairs the overall applicability of the proposed control design. Nevertheless, it is illustratively shown that control effort and oscillations in pitch rate can be reduced.

### 4-3 Attitude control

Although the focus in this thesis is oriented around controlling the aircraft its pitching motions, roll control should be considered for changing the aircraft's heading and rejecting asymmetric aerodynamic disturbances. This section, therefore, considers the control of  $\phi$  and  $\theta$  in an outer-loop control structure that provides the angular rate references for the inner-loop controller. The derivation of this outer loop structure relies on a simpler variation of the NDI method presented in Section 2-1. In this case, only the following kinematic relation is applicable:

$$\underbrace{\begin{bmatrix} \dot{\phi}_{\text{ref}} \\ \dot{\theta}_{\text{ref}} \\ \dot{\psi}_{\text{ref}} \end{bmatrix}}_{\dot{\mathbf{y}}_{\text{ref}}} = \underbrace{\begin{bmatrix} 1 & \sin \phi \tan \theta & \tan \theta \cos \phi \\ 0 & \cos \phi & -\sin \phi \\ 0 & \sin \phi \sec \theta & \cos \phi \sec \theta \end{bmatrix}}_{G_o(\theta, \phi)} \underbrace{\begin{bmatrix} p_{\text{ref}} \\ q_{\text{ref}} \\ r_{\text{ref}} \end{bmatrix}}_{\mathbf{x}_{I, \text{ref}}}. \quad (4-39)$$

By inverting this relation and introducing a virtual control variable  $\boldsymbol{\nu}_o$ , the following control law can be defined:

$$\mathbf{x}_{I, \text{ref}} = G_o(\theta, \phi)^{-1} \boldsymbol{\nu}_o, \quad \text{with} \quad \boldsymbol{\nu}_o = K_{p, o}(\mathbf{y}_{\text{ref}} - \mathbf{y}). \quad (4-40)$$

Here, the virtual control variable  $\boldsymbol{\nu}_o$  is controlled with the diagonal proportional gain matrix  $K_{p, o}$ . By relying on this nonlinear kinematic inversion controller, the aircraft's Euler angles can be controlled towards the desired reference of pitch, roll and course angle. For the course angle or heading, denoted by  $\psi$  in the vector output vector  $\mathbf{y}$ , no specific reference will be defined as it is preferred to roll the aircraft into a coordinated turn to minimize drag. To achieve this coordinated condition, a sideslip angle controller will be considered.

Controlling the sideslip angle of a glider is especially relevant when considering that long and slender wings tend to produce more induced drag than shorter wings. As such, a counter and negative yaw moment is introduced when positive rolling motions is generated by the ailerons. This is explained by the fact that the wing that moves up produces more lift and thus more induced drag than the wing that goes down. This effect is known as adverse yaw and should be considered when controlling a glider. Therefore, to maximize the efficiency of the glider the side slip angle should be controlled to zero. To achieve this reference condition, two types of control techniques will be considered depending on the measurements available.

#### 4-3-1 Direct side-slip control

In case the side slip angle can be measured or estimated, a reference for the yaw rate can be found through the nonlinear dynamic inversion control law proposed in Section 2-1. This control law is found by substituting the accelerations from (4-41) in the derivative of  $\dot{\beta}$  (3-14).

$$\begin{bmatrix} \dot{u} \\ \dot{v} \\ \dot{w} \end{bmatrix} = \frac{1}{m} \begin{bmatrix} \mathcal{X} \\ \mathcal{Y} \\ \mathcal{Z} \end{bmatrix} + \begin{bmatrix} 0 & -w & v \\ w & 0 & -u \\ -v & u & 0 \end{bmatrix} \begin{bmatrix} p \\ q \\ r \end{bmatrix} + \mathbb{T}_B^N \begin{bmatrix} 0 \\ 0 \\ g \end{bmatrix}. \quad (4-41)$$

By rearranging the resulting equations, and introducing the measurable body accelerations as  $a_x$ ,  $a_y$  and  $a_z$ , the following reference for the yaw rate can be obtained:

$$r_{\text{ref}} = \left( \frac{-u}{\sqrt{V^2 - v^2}} \right)^{-1} \left[ \nu_\beta - \frac{1}{\sqrt{V^2 - v^2}} \left( -\frac{uv}{V^2} a_x + \left( 1 - \frac{v^2}{V^2} \right) a_y - \frac{vw}{V_t^2} a_z \right) - \frac{w}{\sqrt{V^2 - v^2}} p_{\text{ref}} \right]. \quad (4-42)$$

Similar as the previous discussed nonlinear inversion control law, here the virtual control input  $\nu_\beta$  is found by linearly controlling the side slip error using a proportional controller.

### 4-3-2 Indirect side-slip control

When the side slip angle can not be estimated or measured, a reference for  $\dot{\psi}$  can be derived from a coordinated turn condition. By assuming that the bank angle is equal to the roll angle and that the flight angle is equal to the pitch angle, the sum of forces in the lateral direction of the horizontal plane can be described by:

$$mV \cos \theta \dot{\psi} = \mathcal{Y} \cos \beta \cos \phi + L \sin \phi. \quad (4-43)$$

To achieve a coordinated turn with zero side slip angle, it should hold that the side forces are zero, i.e.  $\mathcal{Y} = 0$ . By additionally assuming that  $L = mg$ , a reference for  $\dot{\psi}$  can be derived by rewriting (4-43) as

$$\dot{\psi}_{\text{ref}} = \frac{g \sin \phi}{V \cos \theta} \quad (4-44)$$

Consequently, a reference for  $\dot{\psi}$  is set by a feed-forward of both the reference pitch and roll angle. It should be noted however that this feed-forward does not anticipate a constant wind disturbance. To compensate for this and the other assumptions made in the derivation, an additional proportional control law on the lateral acceleration can be included.

$$\dot{\psi}_{\text{ref}} = \frac{g \sin \phi}{V \cos \theta} + K_{p,\psi} a_y. \quad (4-45)$$

## 4-4 Conclusive remarks

In this chapter, we presented the limitation of implementing INDI control laws for aeroservoelastic control applications in Section 4-1. It is shown that the phase lags of actuator dynamics and filters are increasing the interactions between the aeroelastic dynamics and the control system. To account for these effects a linear  $\mathcal{H}_\infty$  is augmented to the conventional INDI controller to damp the resulting oscillating behaviour.

Through this augmentation, it has illustratively been shown that the control effort can be reduced and that tracking can be improved. Furthermore, to account for varying time delays or actuator saturation the concept of PCH is included in the design synthesis formulation. The design primarily focused on the alleviation of the symmetric structural motions as these were most dominantly interacting with the control system. For implementing the developed symmetric control system two outer-loop control structures are proposed in 4-3. Depending on the available side-slip angle measurements, an direct and indirect side-slip angle controller



# Simulation and implementation results

In this chapter, the controller performance and robustness are evaluated by tracking a pre-defined reference of pitch angle. For this evaluation, a comparison between the discussed controllers and a baseline PID controller will be provided. The robustness of the controllers is tested in situations where time delays and model mismatches are present. Lastly, the implementation of the INDI controller on the Diana-2 demonstrator is presented.

## 5-1 Simulation results

In this section, simulations are performed to evaluate the performance and robustness of the developed controllers. In these simulations, the performance and robustness metrics from Section 2-4 and Section 2-4-2 are calculated to compare the INDI- $\mathcal{H}_\infty$  controller against the conventional INDI controller and a baseline controller. This baseline controller will be introduced first, subsequent subsections then present the comparison in terms of performance and robustness.

### 5-1-1 Baseline control design

To arrive at a representative comparison between the developed controllers and a commonly used control structure, a PID controller will be considered as a baseline. In most aeroservoelastic applications [7], PID controllers are used in conjunction with passive roll-off filters to isolate the rigid-body dynamics from the structural dynamics. In the model of the SB-10 glider, however, the dynamics of the structural motions are too close the rigid motions and inadequate performance will occur. As a solution instead, the derived PID controller from Section 2-2-3 will be considered as a baseline.

The main benefit of using this control structure is that the PID gains can found from the INDI control gains and that a similar response can be obtained. This similar response is especially important when considering that for a representative comparison, a similar rise and should

be achieved to excite the structural dynamic equally. Note that this mainly relevant for the faster dynamics in the inner-loop. Therefore, the same nonlinear dynamic inversion strategy from Section 4-3 can be considered for the outer loop. As such, this resulting control scheme that is used as a baseline is shown in Figure 5-1.

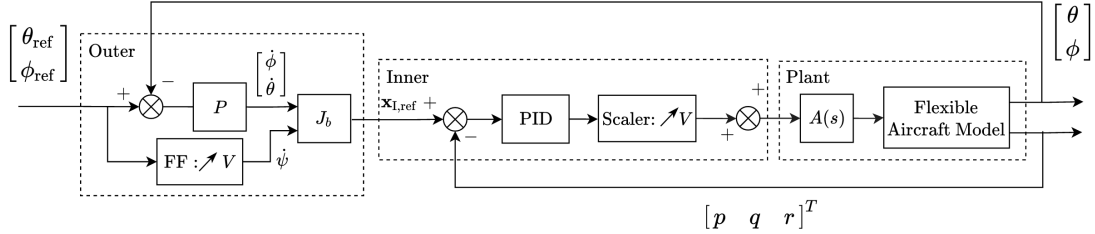
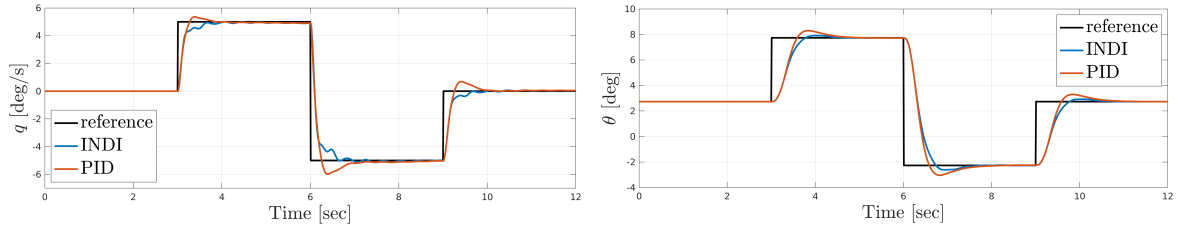


**Figure 5-1:** The baseline control architecture with the kinematic nonlinear inversion controller in the outer-loop and baseline PID controller in the inner-loop

Here, the PID gains in the inner-loop are obtained from (2-24) and are relying on the same control effectiveness coefficients as the INDI controller. Accordingly, the PID control gains can be defined as

$$K_p^{\text{PID}} = B_0(V)^{-1} (\omega_a + K_p^{\text{INDI}}), \quad K_i^{\text{PID}} = B_0(V)^{-1} K_p^{\text{INDI}} \omega_a, \quad K_d^{\text{PID}} = B_0(V)^{-1}. \quad (5-1)$$

Note that the control effectiveness  $B_0$  depends on the airspeed  $V$ , that the  $K^{\text{INDI}}$  are the configured INDI control gains and that  $\omega_a$  denotes the actuator bandwidth in Hz. To illustrate the similar responses between the baseline and the INDI controller, the pitch rate and pitch angle responses are simulated for the nominal condition in Figure 5-2a and Figure 5-2b, respectively. As can be seen in Figure 5-2a, the rise time of the PID controller closely matches



**(a)** Pitch rate response of the INDI and PID controller **(b)** Pitch angle response of the INDI and PID controller

**Figure 5-2:** Pitch rate and pitch angle responses of the INDI controller and the baseline PID controller for the nominal simulation condition described in Table 4-1

the rise time of the INDI controller. Furthermore, the inclusion of the differential gain in the PID controller allows for a smoother dampening of the structural dynamics at the cost of producing slightly more overshoot. Note that time delays are not included in this simulation. The next subsection will evaluate the effect of these delays by considering suitable evaluation configurations.

### 5-1-2 Controller performance comparison

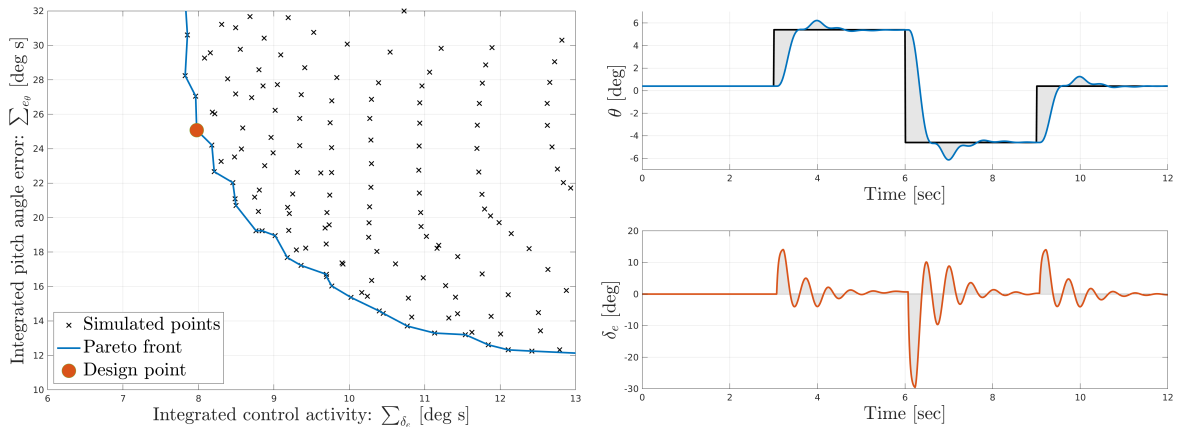
As already mentioned in Section 4-2-4, an operating condition at an airspeed of 40 m/s will be selected to evaluate the performance of the developed controllers. At this operating condition,

three additional time delay configurations will be considered. These three configurations are classified into a best-case (BC) with minimal time delays, a mid-case (MC) with realistic time delays and a worst-case (WC) with the most unforeseeable time delays. These configurations are clarified in Table 5-1 and motivated by the time delay identification analyses in Section D. At the 40 m/s operating condition, a worst-case time delay scenario will be selected as a design

**Table 5-1:** The three different time delay configurations that are used for evaluating control performance and control robustness

	Process $\tau_p$ [ms]	Transport $\tau_t$ [ms]	Measurement $\tau_m$ [ms]
Best case (BC)	20	10	0
Mid case (MC)	30	20	10
Worst case (WC)	30	30	20

point. For this design configuration, an equal reference model and inner-loop INDI control gain are selected and a simple grid of test points are simulated to get insight into how the performance changes when the inner-loop gains and outer-loop are varied. The corresponding pitch angle error and elevator deflection are integrated and plotted on the horizontal and vertical axis of Figure 5-3a to visualize the performance variation. Note that a Pareto front can be observed and a gain configuration on this line is selected for the conventional INDI controller as a design point. This point is indicated by the red colored dot and corresponds to an integrated pitch angle error of  $\sum e_\theta = 7.98$  [°s] and a integrated and control effort of  $\sum \delta_e = 25.08$  [°s]. The gain values at this design point are  $K_{p,o} = 3.2$  and  $K_{p,i} = 7.4$  and the corresponding doubled response in a pitch angle and elevator input are shown in Figure 5-3b. With these gains and the worst-case time delay configuration, the baseline PID



(a) Simulation for different  $K_{p,o}$  and  $K_{p,i}$  gains (b) Corresponding pitch angle and elevator deflections.

**Figure 5-3:** The left figure shows the simulations for a grid of inner and outer loop control gains that is evaluated by the integrated pitch angle error and the elevator deflection. The right figure displays the pitch angle and elevator response of the selected design point. Here, the shaded represents the integrated pitch angle error and elevator deflection.

controller is tuned using (5-1) and the INDI- $\mathcal{H}_\infty$  is synthesised using the procedure described in Section 4-2. Note that the same INDI outer-loop controller will be added to all three inner-loop controllers and that their performance will be evaluated with and without wind and

turbulence disturbances. These disturbances are equal for all cases and are generated using the Von Kármán model that is parameterized with a scale length of  $L_w = 1000$  m, a gust intensity of  $\sigma_\omega = 0.8$  m/s, and a probability of exceedance of  $10^{-3}$  (moderate conditions). For the same  $5^\circ$  doublet reference signal as in Figure 5-3b, the three controllers are simulated and plotted in the figures presented in Section C. The performance metrics are calculated and presented in Table 5-2. Here, one should observe that most oscillations are present in the baseline PID

**Table 5-2:** Comparison table between the PID, INDI and INDI- $\mathcal{H}_\infty$  controllers. The controllers are simulated with the same INDI outer-loop and a worst-case time delay configuration at 40 m/s

	PID		INDI		INDI- $\mathcal{H}_\infty$	
	without disturbance	with disturbance	without disturbance	with disturbance	without disturbance	with disturbance
RMS $_{\theta}$ [°]	0.031	0.032	0.032	0.033	0.032	0.033
$\sum e_{\theta}$ [°s]	8.56	9.45	7.98	9.51	7.93	9.40
$\sum \delta_e$ [°s]	70.78	93.14	25.08	33.16	23.19	30.98
CMSD $_{\theta}$ [°]	140.91	202.66	102.49	142.72	99.88	133.54
CMSD $_{\delta_e}$ [°]	68.76	119.59	17.55	24.88	15.37	23.39
CMSD $_{\dot{\eta}_1}$ [-]	0.59	1.05	0.24	0.63	0.21	0.57
CMSD $_{\dot{\eta}_2}$ [-]	0.38	0.66	0.089	0.20	0.058	0.29

controller response. This can be explained by considering that the derivation of the baseline PID controller is more sensitive to time delay than the INDI controller (refer to Section 2-2-3). For the INDI with  $\mathcal{H}_\infty$ , a more relaxed flexible motion is presented by the lower CMSD values of the modal velocities and elevator deflection. This suggests that less interaction between the elevator and the structural dynamics occurs when INDI- $\mathcal{H}_\infty$  control is used over conventional INDI control. For the cases with disturbances, however, the INDI- $\mathcal{H}_\infty$  controller produces more oscillations of the second modal velocity than the conventional INDI controller. This entails that not all performance requirements can be satisfied and that compromises have to be made when tuning the INDI- $\mathcal{H}_\infty$  controller. To illustrate the limitations of tuning for disturbance rejection, tracking and wing bending reduction the corresponding vertical wingtip velocities and strain measurements are plotted in figure 5-4a and 5-4b, respectively. In these plots, it should be noticed that during the first three seconds, the addition of the  $\mathcal{H}_\infty$

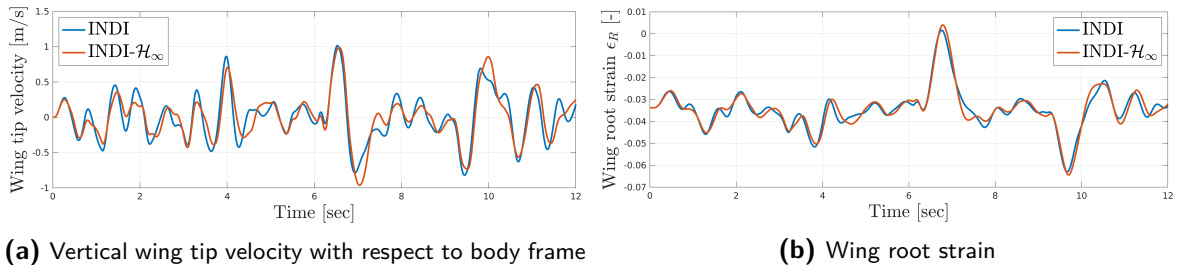


**Figure 5-4:** Vertical wingtip velocity on the left with corresponding strain measurements at the wing root at the right. Note that these responses correspond to the same disturbance conditions as in Table 5-2.

controller, reduces the wingtip velocity and relaxes the strain measurements at wing the root.

Thereafter, when the error between the doublet reference and the pitch angle increases, higher vertical velocities and strain values can be observed. From this, one can state that the effect of the INDI controller is more dominantly present and that the addition of the  $\mathcal{H}_\infty$  controller cannot provide enough control action to also improve both structural motion alleviation and disturbance rejection. Nevertheless, one should notice that the INDI- $\mathcal{H}_\infty$  results in a more overall relaxed flexible motion response than the conventional INDI controller.

### 5-1-3 Controller robustness comparison

To evaluate the robustness of the developed control systems, Time Delay Margins (TDM) are computed and various combinations of different parameters configurations are simulated. Note that the methods used to perform these analyses are already introduced in Section 2-4-2. This section solely focuses on selecting suitable evaluation conditions and presenting the simulation results.

#### Time Delay Margin simulations

To compute the TDM in simulations, a reference signal for the pitch angle is generated and presented in Figure 5-5. The only constraints regarding this reference signal are the minimum and maximum pitch angle references of  $\pm 5^\circ$  to realistically model the considered doublet responses. In the 45 seconds lasting simulations, the controllers are subjected to the same Von Kármán disturbances as discussed in Section 5-1-2. If the response is unstable or exceeding the stability limits of  $\pm 15^\circ$  an upper bound of the time delay is saved. Accordingly, a bisection method is repeated up until a certain error between the upper and lower bound is achieved. The varied time delays are added behind the actuator dynamics inside the plant

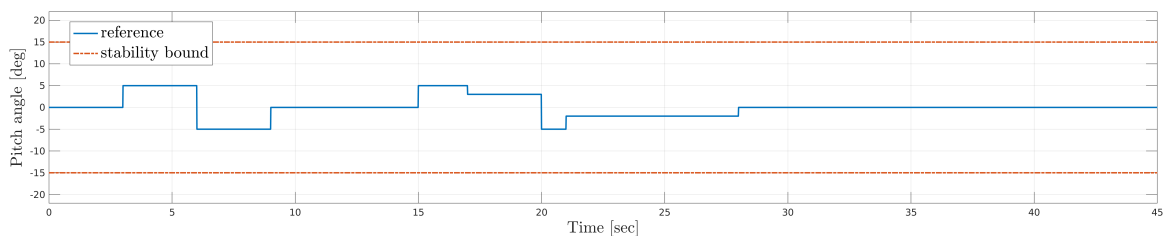


**Figure 5-5:** The reference signal of pitch angle in blue, with upper and lower stability limits marked in red, used in TDM simulations

model to simulate phase lags of the system itself rather than adding them in front of the actuator and also delaying the actuator feedback measurements with the same variation. In this way, the phase lags that can originate from parametric uncertainties are considered. The simulations are performed at the 40 m/s operating conditions for various controllers and time delay configuration. The resulting Time Delay Margins are presented in Table 5-3. In this table, it can be seen that the PID baseline controller is most sensitive to time delays. This is not unexpected as its derivation in Section 2-2-3 disregards the presence of phase lags or time delays. The incremental control techniques do systematically compensate for the delay as it is based on a Taylor series expansion about a previous point in time. As such, larger TDM values can be observed for the INDI based controllers. More noticeably, the INDI-ICA

**Table 5-3:** Computed TDM of the PID, INDI-ICA, INDI and INDI- $\mathcal{H}_\infty$  controllers for different time delay configurations at an operating condition with 40 m/s.

	PID	INDI-ICA	INDI	INDI- $\mathcal{H}_\infty$
BC, TDM [ms]	10.64	26.64	39.84	47.65
MC, TDM [ms]	0.98	17.96	30.47	36.71
WC, TDM [ms]	0.78	8.59	22.65	28.91

controllers from Section 4-1-4 can tolerate less time delay variation than the INDI controller without allocation. This suggests that the INDI and INDI- $\mathcal{H}_\infty$  controller are more robust against the considered time delays variations than the PID and INDI-ICA controller.

Note, however, that the performed simulations are only computing an upper bound of the TDM and that the time delays are equally varied across the input channel. In practical implementations, the different variations of time delays on the input channels cannot be neglected. Analytical metrics can provide more adequate information about the admissible set of time delays variations in this context. In this work, the derivation of such an analytical metric for the  $\mathcal{H}_\infty$  controller will not be considered. Instead, through analyzing multiple time delay configurations, it is shown that for each considered combination the  $\mathcal{H}_\infty$  is more robust.

### Parametric uncertainty simulations

In addition to the robustness evaluation using TDM computations, different rigid-body and structural coefficients are varied to get insight into how sensitive the controllers are against parametric uncertainties. For the same 12 seconds doublet manoeuvre as presented in the previous subsection, repeated simulations have been performed in which aerodynamic coefficients in (3-10) are scaled with a scaling factor  $F_{i,*}^*$ . The selected scaled coefficients are defined as

$$\begin{aligned} C_{\eta_1, A_{FF}}^{\text{scaled}} &= F_{i,\eta}^{\eta_1} \begin{bmatrix} C_{\eta_1}^{\eta_1} & C_{\eta_2}^{\eta_1} & C_{\eta_3}^{\eta_1} \end{bmatrix} & C_{\eta_2, A_{FF}}^{\text{scaled}} &= F_{i,\eta}^{\eta_2} \begin{bmatrix} C_{\eta_1}^{\eta_2} & C_{\eta_2}^{\eta_2} & C_{\eta_3}^{\eta_2} \end{bmatrix} \\ C_{\dot{\eta}_1, A_{FF}}^{\text{scaled}} &= F_{i,\dot{\eta}}^{\eta_1} \begin{bmatrix} C_{\dot{\eta}_1}^{\eta_1} & C_{\dot{\eta}_2}^{\eta_1} & C_{\dot{\eta}_3}^{\eta_1} \end{bmatrix} & C_{\dot{\eta}_2, A_{FF}}^{\text{scaled}} &= F_{i,\dot{\eta}}^{\eta_2} \begin{bmatrix} C_{\dot{\eta}_1}^{\eta_2} & C_{\dot{\eta}_2}^{\eta_2} & C_{\dot{\eta}_3}^{\eta_2} \end{bmatrix}. \end{aligned} \quad (5-2)$$

While the scaled control effectiveness is specified as:

$$\begin{aligned} C_{\eta_1, \delta_e}^{\text{scaled}} &= F_{i,\delta_e}^{\eta_1} C_{\eta_1} \delta_e & C_{\eta_2, \delta_e}^{\text{scaled}} &= F_{i,\delta_e}^{\eta_2} C_{\eta_2} \delta_e \\ C_{\eta_1, \delta_{fo}}^{\text{scaled}} &= F_{i,\delta_{fo}}^{\eta_1} C_{\eta_1} \delta_{fo} & C_{\eta_2, \delta_{fo}}^{\text{scaled}} &= F_{i,\delta_{fo}}^{\eta_2} C_{\eta_2} \delta_{fo}. \end{aligned} \quad (5-3)$$

To evaluate the sensitivity of the augmented  $\mathcal{H}_\infty$  controller, mainly the structural dynamics of the first and second bending mode are varied. The model coefficients with respect to modal amplitude and modal velocity are scaled separately to simulate changing aerodynamic damping conditions. As the undamped modal frequencies are acquired through ground vibration tests, they are considered to be known with sufficient certainty. Therefore, only the coefficients for the generalized load with respect to flexible states are varied over a minimum and maximum value. The limits of these values are set by  $F_{i,*}^* = \pm 20\%$ . Furthermore, the rigid-body control effectiveness coefficient  $C_{\mathcal{M}_{\delta_e}}$  is scaled with +20% to simulate a worst-case gain configuration. For each of the scaled combinations, the pitch angle responses of the

INDI and INDI- $\mathcal{H}_\infty$  controllers are simulated and presented in Figure C-4a and Figure C-4b, respectively. Looking at both figures it can be seen that the INDI response produces more

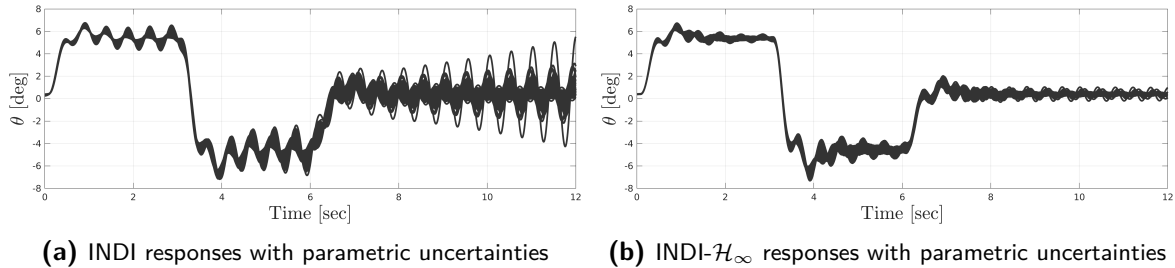


**Figure 5-6:** Robustness comparison between the INDI controller and the INDI- $\mathcal{H}_\infty$  controller for various parametric uncertainty configurations of the structural dynamics.

oscillations than the INDI- $\mathcal{H}_\infty$  controller. For specific parameter simulated parameter configurations, one can observe that the INDI response even becomes unstable. The INDI- $\mathcal{H}_\infty$  controller seems to remain stable and is, therefore, considered to be more robust against the simulated parameter uncertainties.

## 5-2 Implementation results

One of the challenges in this research is to also implement and validate the previously discussed control concepts. To achieve this, the controllers have to be implemented on the available hardware platform of the 1:3 scaled Diana-2 demonstrator. Note that this platform is specifically built for the Diana-2 demonstrator and that the controllers have to be designed using the corresponding aircraft model accordingly. As discussed in Section 3-4, the main difference between the SB-10 and the Diana-2 model is that the frequency separation between the structural dynamics and the rigid-body dynamics is higher in the Diana-2 model. Consequently, the benefit of applying the proposed design  $\mathcal{H}_\infty$  formulation fades when considering that the washout filter on the angular rate feedback in INDI control will attenuate or remove the effect of the structural motions. Through considering this, the focus in this section is oriented to implementing and validating the conventional INDI controller.

As a step towards implementing this controller, the available hardware platform will be introduced first in Section 5-2-2. The subsequent section will then present the used hardware-in-the-loop simulation for testing the controller effectively on real hardware. Note that due to unforeseen practical instrumentation issues, its proof of concept is only tested in experiments on the ground in Section 5-2-3

### 5-2-1 Available hardware platform of the Diana-2 demonstrator

To gather the desired measurements during flight, the Diana-2 is equipped with hard-and-software hardware components to accommodate the required sensing, processing and actuating capabilities. The resulting platform on which the controllers are implemented is illustrated in Figure 5-7 and consist of two main computing components, namely, the flight computer and the data acquisition system. Here, the Pixhawk 4 hardware board is used as a flight computer

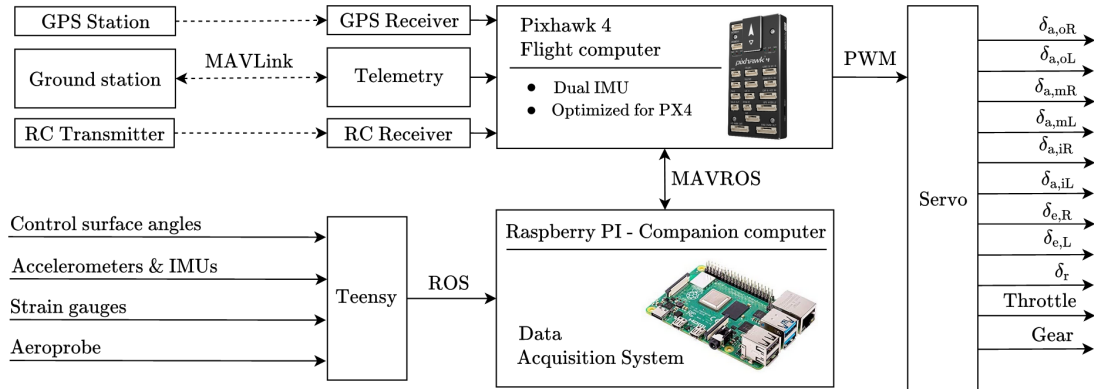


**Figure 5-7:** Data flow through the different available hardware component on the Diana-2 demonstrator

and runs the optimized PX4 autopilot software to receive commands from the transmitter, communicate with the ground station and drive the servos of the gear, engine and control surfaces. It includes a dual IMU and a Global Positioning System (GPS) module that feeds the obtained measurements through an Extended Kalman Filter (EKF) to estimate and synchronize the state variables for control. The additional IMU, strain, air and control surface angle measurements, that are positioned at specific locations on the airframe, are pre-processed on four micro-controllers and send to the data acquisition system using ROS (Robotic Operating System).

For communicating between the data acquisition system and the flight computer, a mavros ROS package is used to enable the required MAVLink messaging protocol. Accordingly, custom MAVLink messages and mavros plugins are created to send the control surface angle measurements and the aeroprobe measurements from the Raspberry PI to the Pixhawk. To use these measurements in the controller, corresponding uORB topics are created inside PX4 its inter-process messaging Application Programming Interface (API). The controller, that is designed in MATLAB/Simulink, reads from those custom uORB topics in a similar fashion as it does for other standard topics inside PX4.

Because the data acquisition system was not reliable enough, the additional measurements were, in the end, not used in closed-loop. Instead, the airspeed sensor was directly connected to the Pixhawk and the actuator feedback was modelled inside the control loop using the identified actuator model and the estimated transport delay. For testing the control design integration with PX4 and the Pixhawk computer, a hardware-in-the-loop simulation is developed.

### 5-2-2 Hardware-in-the-loop simulation

The developed hardware-in-the-loop (HIL) simulation emulates the controlled flight dynamic response by taking the effect of running the controller on real hardware into account. As the existing HIL simulations with PX4 and the Pixhawk do not include the desired aeroservoelastic modelling platform, a custom HIL simulation with MATLAB/Simulink is developed. The closed-loop interconnection of this simulation together with corresponding visualisation and connectivity is illustrated in Figure 5-8.

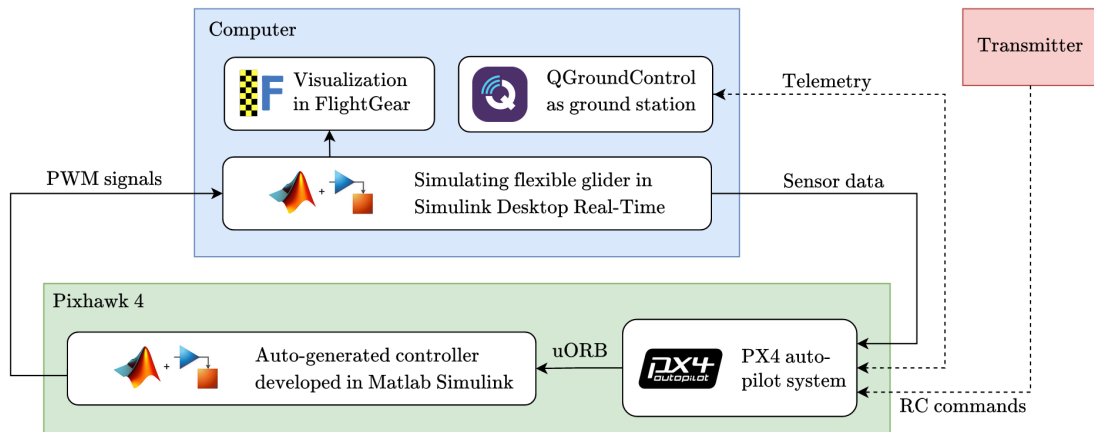


**Figure 5-8:** Developed hardware-in-the-loop simulation in which the the simulation on the computer runs at 200 Hz, the visualization receives data at 20 Hz, the controller on the Pixhawk runs at 100 Hz and the simulation receives the PWM signals at around 70 Hz.

The simulation model, that runs on the computer, receives MAVLink messages from the Pixhawk over a serial connection. These messages are decoded and translated into control inputs to simulate the aircraft response in real-time using the Simulink Desktop Real-Time toolbox in MATLAB/Simulink. The simulated virtual sensor outputs are then decoded to MAVLink messages and send back to the Pixhawk over a different port to trick the controller into thinking it is assembled into the real aircraft. The resulting hardware-in-the-loop setup with the Diana-2 is illustrated in Figure 5-9.

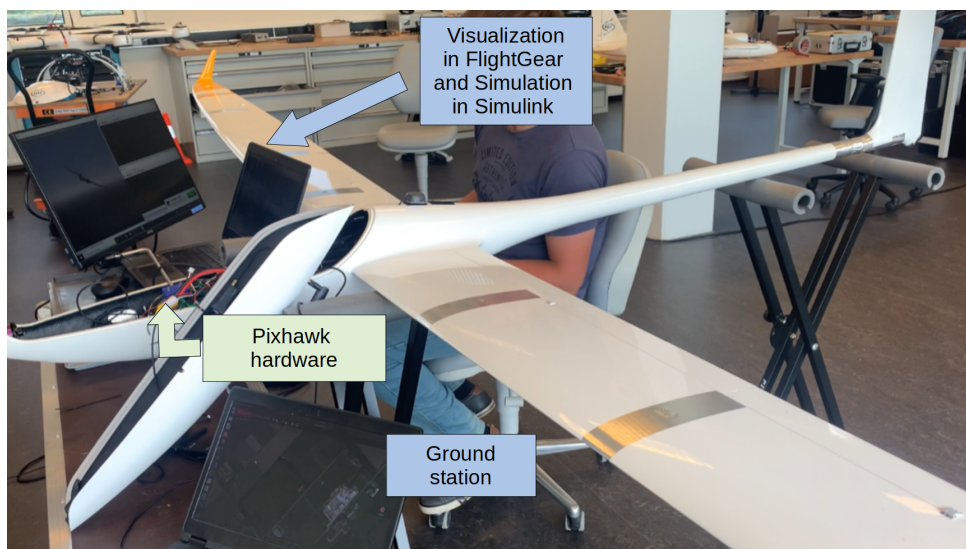


**Figure 5-9:** HIL setup for the Diana-2 demonstrator.

In addition to verifying whether the controller sends the correct commands to the control surfaces, this HIL simulation is also used to evaluate the integration of the flight controller in the utilized PX4 auto-pilot system. As such, connectivity to the ground station and responsiveness to the transmitter is tested to familiarize the pilot with the switching sequence

between the manual mode, the angular rate control mode and the attitude control mode.

### 5-2-3 Ground test experiments

Before conducting the actual flight test, two ground test experiments have been performed to ensure that the controller is reacting to real sensor data as expected. These ground tests include a tilt test and a taxi test. In the tilt test, it was evaluated whether the control surfaces are deflecting in the right directions by tilting the aircraft and producing known angular rate directions. The taxi test is performed to assess the roll stabilization of the controller at low dynamic pressure conditions. During this last test, the airspeed sensor was unfortunately incorrectly initialized, and as consequence, a saturated airspeed of 15 m/s was used in the controller. Due to the actually lower true airspeed, the control effectiveness was underestimated in the INDI controller. Consequently, insufficient roll stabilization was observed. To confirm that the airspeed scaling was the primary issue here, the roll rate response is simulated with the Diana-2 model using the measured roll rate references commanded by the pilot. In this simulation, the same constant airspeed of 15 m/s was used in the controller while a lower estimated true airspeed was set in the model. Furthermore, as only roll control is considered the model was constrained to zero pitching and yawing motions. The resulting plots of the simulated and measured roll rate response are presented in Figure 5-10a. Note that the corresponding controller output in terms of Pulse-width modulation (PWM) values is shown in Figure 5-10b. Here, it can be seen that the amplitude of the measured control output

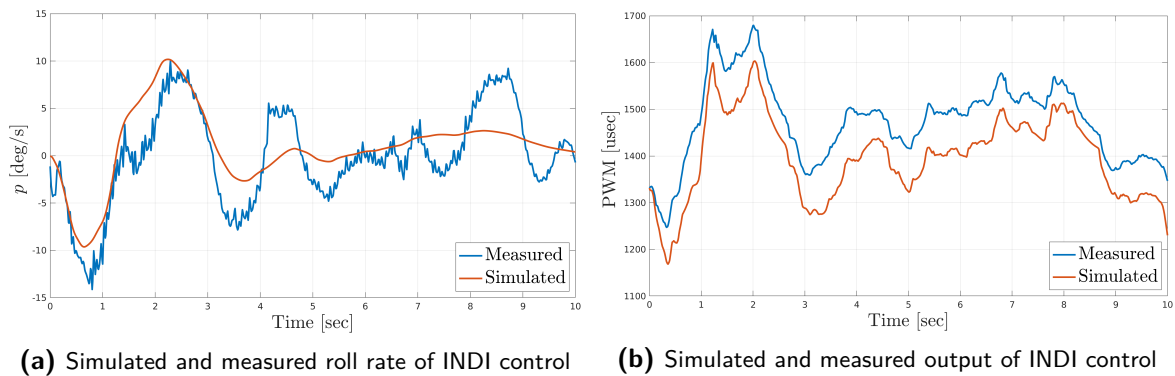


**Figure 5-10:** Simulated and measured roll rate response in the left figure with corresponding PWM outputs in the right figure. The used true airspeed in simulation is set to the mean of the measured ground speed plus an estimate of the wind speed. This resulted in a value of 5.65 m/s.

closely matches the simulated control output. This suggests that the controller is working correctly in real-time and that the control effectiveness coefficients are in the correct order of magnitude. However, as the simulation model is not validated yet, it cannot be concluded with certainty that the model-dependent parameters in the INDI controller are correct.

## 5-3 Discussion

In this chapter, simulations showed that the INDI- $\mathcal{H}_\infty$  controller outperforms the baseline and the conventional INDI controller in terms of tracking accuracy and structural motion

relaxation. Without considering aerodynamic disturbances, the addition of the  $\mathcal{H}_\infty$  controller reduces the oscillations in the pitch angle by 6.4% and the oscillations in the computed elevator input by 5.9%. Despite this benefit, it is noticed that tracking is more dominantly achieved than disturbance rejection or load alleviation. This can be explained by the selected input-output weights in the synthesis formulation and the limited control variables in the  $\mathcal{H}_\infty$  controller. In this respect, future research can investigate which combination of control variables and tuning weights can result in an even better simultaneous reference tracking and structural motion alleviation response.

For evaluating robust performance, repeated TDM and parametric uncertainty simulations have been performed. These simulations showed that the addition of the  $\mathcal{H}_\infty$  can improve the robust performance of an INDI controller. Note, however, that for synthesising the  $\mathcal{H}_\infty$  a reasonable aeroservoelastic model is still required and that the model-independent benefit of INDI is impaired by the addition of the  $\mathcal{H}_\infty$  controller.

This seems to be contradicting with the control design objective for the 1:3 scaled flexible glider of NLR mentioned in Section 1-1. Here, it is stated that a controller should be designed without an accurate aeroservoelastic model. However, using the uncertain Diana-2 model it was noticed with certainty that the rigid-body dynamics can be controlled separately from the structural dynamics and that minor aeroservoelastic effects are expected. Therefore, as the first step towards validation, only the conventional INDI controller has been implemented on the Diana-2.

As mentioned in this chapter, the PX4 flight control software was utilized for implementing the INDI controller. For testing the controller on real hardware, a custom hardware-in-the-loop simulation was developed. After successfully familiarizing the pilot with the switching sequences between the control modes, ground tests have been performed prior to the actual flight test. These ground tests show that the INDI controller responds as expected appropriately scaled with airspeed. Unfortunately, due to unforeseen practical issues, no actual flight tests have been conducted. Nevertheless, the platform for implementing and testing the controllers has been developed.



# Conclusions and recommendations

## 6-1 Conclusions

The main goal of this thesis was to develop a synthesis method of a robust and real-time implementable flight controller for a high aspect ratio and flexible aircraft. To that aim, we investigated the applicability of a sensor-based Incremental Nonlinear Inversion (INDI) control strategy and proposed a  $\mathcal{H}_\infty$ -based synthesis method to alleviate the unfavourable aeroseroelastic interactions. Compared to the nonlinear incremental flight control methods in [18] and [19], this thesis has focused on the development and validation of a practically implementable controller. In this respect, the developed method incorporates the effect of hardware events and synthesizes the closed-loop controller offline to eliminate online optimizations and estimations. To verify whether this design method achieves the remaining requirements of the overall research goal, we recall the three sub-research questions that were initially reported in the introductory chapter.

- *What synthesize method can be developed to simultaneously achieve reference tracking and structural motion alleviation in the presence of sensor noise and time delays?*

In Section 4-1 it is shown that oscillations in the structural dynamics cannot be compensated by the conventional INDI controller when actuator dynamics, filters and time delays are included. To reduce these oscillations without using extensive online estimations a promising adaptive incremental control allocation strategy is proposed. However, due to its unavailable non-linear stability proof, a linear  $\mathcal{H}_\infty$ -based synthesis method is developed instead. In this synthesis formulation, the pitching motions are controlled by the elevator through INDI while the coupled structural motions are alleviated by the outboard flaps. In this design formulation, the effects of time delays can be included and the effect of noise can be attenuated by selecting applicable filters. Furthermore, possible biases can be accounted for by considering the design formulation with Pseudo Control Hedging (PCH).

- *How does the performance and robustness of the synthesized INDI control structure compare to the conventional INDI controller and a comparable baseline controller?*

The simulations in Section 5-1 show that the newly synthesized INDI controller results in a more relaxed structural response than the conventional INDI controller. Similar tracking performance is achieved while less structural motion is present and less control energy is needed. When subjected to disturbances, improved tracking performance is better achieved than disturbance rejection or load alleviation. Regarding the robust performance, Time Delay Margins (TDM) were computed using repeated simulations. These simulation showed, that for the considered time delay configurations, the newly synthesized INDI controller is more robust than the conventional INDI controller. Furthermore, repeated simulations with various combinations of the structural parameter have been performed and showed that the addition of  $\mathcal{H}_\infty$  improves robust performance.

- *How can the developed controllers be implemented and validated on the flexible and gliding UAV of NLR?*

In Section 3-4 it was noticed that the frequency separation between the structural and the rigid-body dynamics was larger for the 1:3 scaled Diana-2 aircraft than for the full-scale SB-10 glider. As such, the added value of implementing the additional  $\mathcal{H}_\infty$  on the available hardware platform diminished and the focus in Section 5-2 switched to validating the INDI method for controlling rigid body motions. To this end, a hardware-in-the-loop simulation was developed and ground tests have been performed. These simulations and tests showed that the performance of the INDI controller is promising when correctly scaled with airspeed. The next step would be to validate this in-flight by comparing the INDI controller against a similarly tuned PID controller.

Overall, it can be concluded that the augmentation of the  $\mathcal{H}_\infty$  controller has the potential to improve both tracking and structural motion alleviation. The synthesis method allows the user to incorporate time delays and to suppress the adverse aeroservoelastic effects with INDI-based control. One drawback regarding this synthesis method is that the model independency benefit of INDI fades when considering that the  $\mathcal{H}_\infty$  control synthesis requires a reasonable aeroservoelastic model for realising the expected performance improvements. Furthermore, it is concluded that the SB-10 model is better suited for the synthesis method than the Diana-2 model.

## 6-2 Recommendations

The conventional INDI and newly INDI- $\mathcal{H}_\infty$  can achieve sufficient reference tracking performance but numerous aspects could be improved or further investigated. As subsequent steps towards improving the scalability and applicability of incremental flight control methods to aeroservoelastic aircraft the following four recommendations are suggested for future work.

- **Adaptive incremental control allocation:** One of the main bottlenecks of the proposed INDI- $\mathcal{H}_\infty$  synthesis method is that it still requires a representative aeroservoelastic model. To reduce model dependency the briefly touched upon adaptive incremental allocation controller can be further investigated to reduce the unfavourable aeroservoelastic effects and to reconfigure the control laws in the event of system faults.

- **Improving the designed synthesis formulation:** In this work, the scheduling of the synthesized controller across multiple operating conditions was not considered. Moreover, it was shown that due to the limited control actions, not all structural motions can be reduced in the presence of disturbances. Further research could reveal whether the synthesis method can be improved by considering the following:
  - A more accurate aeroservoelastic model that may also include the effect of unsteady aerodynamics through additional aerodynamic lag states.
  - More control actions and control variables, instead of only using the outboard flaps and the wing tip accelerations.
  - A suitable model reduction techniques to integrate the synthesis formulation in a LPV framework and achieve appropriate scheduling.
- **Flight envelope extension:** The proposed synthesis method can be applied to aeroservoelastic models that have unstable structural modes inside the flight envelope of interest. For such aircraft, reference tracking and flutter suppression control synthesis can be combined to extend the flight envelope.
- **Implementation:** With the hardware platform on the Diana-2 being almost stable and the hardware-in-the-loop simulations developed, future research can focus on validating the INDI controller in-flight by comparing it against a similarly tuned PID controller.



---

# Appendix A

---

## Aeroservoelastic model

This appendix provides the underlying information for the aeroelastic platform presented in Chapter 3. The basic parameters and state dependency of both the SB-10 and Diana-2 models are presented first. Subsequently, the linearization and trim point algorithm are discussed.

### A-1 The SB-10 and Diana-2 glider model

The platform used in this research is the full scale SB-10 glider and the 1:3 scaled Diana-2 glider. The basic properties of these fixed-wing aircraft are listed in Table A-1. Note that the parameters for the SB-10 glider are obtained from [34] while the parameters of scaled Diana-2 are acquired through extensive testing and measuring. With reference to Section 3-2-2, the

**Table A-1:** Basic aircraft parameters of the full-scale SB-10 and the 1:3 scaled Diana-2 demonstrator

Parameter		Full scale SB-10	1:3 scaled Diana-2
Mass	$m$	783 kg	11 kg
Centre of gravity (from AC)	$\Delta X_{cg}$	0.083 m	0.044 m
Roll inertia	$I_x$	14850 kgm <sup>2</sup>	4.54 kgm <sup>2</sup>
Pitch inertia	$I_y$	2510 kgm <sup>2</sup>	4.48 kgm <sup>2</sup>
Yaw inertia	$I_z$	17360 kgm <sup>2</sup>	8.77 kgm <sup>2</sup>
Roll-yaw inertia	$I_{xz}$	-	0.47 kgm <sup>2</sup>
Mean aerodynamic chord	$\bar{c}$	0.872	0.206
Span	$b$	26 m	5 m
Wing area	$S$	21.81 m <sup>2</sup>	1.03 m <sup>2</sup>

dependency of the aerodynamic coefficients for the SB-10 glider are modelled through the

following rigid body state and input vector.

$$\begin{aligned} \mathbf{x}_R^{\text{SB-10}} &= \left[ \alpha \quad \frac{\dot{\alpha}\bar{c}}{2V} \quad \frac{q\bar{c}}{2V} \quad \alpha \frac{q\bar{c}}{2V} \quad \beta \quad \beta\alpha \quad \frac{\dot{\beta}b}{2V} \quad \frac{pb}{2V} \quad \alpha \frac{pb}{2V} \quad \frac{rb}{2V} \quad \alpha \frac{rb}{2V} \right]^T, \\ \mathbf{u}^{\text{SB-10}} &= \left[ \delta_a \quad \delta_a^2 \quad \alpha\delta_a \quad \delta_{f_0} \quad \delta_{f_i} \quad \delta_r \quad \alpha\delta_r \quad \delta_e \right]^T. \end{aligned} \quad (\text{A-1})$$

The rigid body state and input vector of the scaled Diana-2 glider are defined by:

$$\begin{aligned} \mathbf{x}_R^{\text{Diana-2}} &= \left[ \alpha \quad \frac{\dot{\alpha}\bar{c}}{2V} \quad \beta \quad \frac{pb}{2V} \quad \frac{rb}{2V} \right]^T, \\ \mathbf{u}^{\text{Diana-2}} &= \left[ \delta_a \quad \delta_{f_0} \quad \delta_{f_i} \quad \delta_r \quad \delta_e \right]^T. \end{aligned} \quad (\text{A-2})$$

Clearly, the Diana-2 model is less dependent on various combinations of rigid body states and thus less advanced than the SB-10 glider. This is also confirmed by the fact that SB-10 model is validated while the Diana-2 model is only computationally based. However, the validation of the Diana-2 model is planned soon.

Ground vibration tests have been performed for the Diana-2 glider to obtain the mode shapes and undamped natural frequencies of the structural dynamics. These resulting modal frequencies are shown together with the frequencies of the SB-10 glider in Table A-2. As can be

**Table A-2:** Undamped natural frequencies of the structural dynamics for both the full scale SB-10 and 1:3 scaled Diana-2 demonstrator

Aircraft	$\omega_{\eta_1}$	$\omega_{\eta_2}$	$\omega_{\eta_3}$	$\omega_{\eta_4}$	$\omega_{\eta_5}$	$\omega_{\eta_6}$	$\omega_{\eta_7}$	$\omega_{\eta_8}$	$\omega_{\eta_9}$
Full scale SB-10 [Hz]	1.34	2.55	4.15	3.28	2.64	-	-	-	-
1:3 scale Diana-2 [Hz]	6.94	9.81	15.13	18.17	20.44	21.90	25.46	31.54	34.05

seen in this table, the undamped natural frequencies of the Diana-2 are significantly higher than the SB-10. Through also considering the larger inertia's of the SB-10, it becomes obvious that the SB-10 glider is more flexible than the Diana-2 glider. Note that the coefficients in of the models correspond to an condition where the modal masses and the damping in (3-4) are set to 1 kg and 2%, respectively. This dampening ratio of 2% is inspired from [40].

## A-2 Linearization algorithm

The used linearization algorithm in Section 3-4 and Section 4-2-1 relies on the finite difference approximation of the system dynamics at a stable operating point. This finite difference approximation is performed by the Jacobian linearization method presented A-2-1. The algorithm for finding a stable trim point is discussed in A-2-2.

### A-2-1 Jacobian linearization

To illustrate the concept of Jacobian linearization, consider that the nonlinear dynamics of an aircraft can be described by the following state and output equation

$$\begin{aligned} \dot{\mathbf{x}} &= \mathbf{f}(\mathbf{x}, \mathbf{u}) \\ \mathbf{y} &= \mathbf{h}(\mathbf{x}, \mathbf{u}). \end{aligned} \quad (\text{A-3})$$

Here,  $\mathbf{f}$  and  $\mathbf{h}$  are nonlinear mappings of the state vector  $\mathbf{x} \in \mathbb{R}^n$  and the control input vector  $\mathbf{u} \in \mathbb{R}^m$  to  $\dot{\mathbf{x}}$  and  $\mathbf{y} \in \mathbb{R}^\ell$ , respectively.

The state  $\bar{\mathbf{x}}_i$  is called an equilibrium or trim point for some equilibrium condition  $i$  that satisfies  $0 = \mathbf{f}(\bar{\mathbf{x}}_i, \bar{\mathbf{u}}_i)$  with some constant input  $\bar{\mathbf{u}}_i$ . By applying a coordinate transformation to the state  $\tilde{\mathbf{x}} = \mathbf{x} - \bar{\mathbf{x}}_i$  and the input  $\tilde{\mathbf{u}} = \mathbf{u} - \bar{\mathbf{u}}_i$  and performing a Taylor expansion that neglects all higher order terms, the following linear representation can be obtained

$$\begin{aligned}\dot{\tilde{\mathbf{x}}}(t) &\approx A_i \tilde{\mathbf{x}}_i + B_i \tilde{\mathbf{u}}_i \\ \tilde{\mathbf{y}}(t) &\approx C_i \tilde{\mathbf{x}}_i + D_i \tilde{\mathbf{u}}_i.\end{aligned}\tag{A-4}$$

This is a linear time invariant (LTI) system with  $A_i \in \mathbb{R}^{n \times n}$ ,  $B_i \in \mathbb{R}^{n \times m}$ ,  $C_i \in \mathbb{R}^{\ell \times n}$  and  $D_i \in \mathbb{R}^{\ell \times m}$  specified by

$$A_i := \left. \frac{\partial \mathbf{f}}{\partial \mathbf{x}} \right|_{\substack{\mathbf{x}=\bar{\mathbf{x}}_i \\ \mathbf{u}=\bar{\mathbf{u}}_i}}, \quad B_i := \left. \frac{\partial \mathbf{f}}{\partial \mathbf{u}} \right|_{\substack{\mathbf{x}=\bar{\mathbf{x}}_i \\ \mathbf{u}=\bar{\mathbf{u}}_i}}, \quad C_i := \left. \frac{\partial \mathbf{h}}{\partial \mathbf{x}} \right|_{\substack{\mathbf{x}=\bar{\mathbf{x}}_i \\ \mathbf{u}=\bar{\mathbf{u}}_i}}, \quad D_i := \left. \frac{\partial \mathbf{h}}{\partial \mathbf{u}} \right|_{\substack{\mathbf{x}=\bar{\mathbf{x}}_i \\ \mathbf{u}=\bar{\mathbf{u}}_i}}.\tag{A-5}$$

This type of Jacobian linearization can be easily automated for each of the system matrices in (A-5) using Algorithm 1.

---

**Algorithm 1** Numerical computation of the Jacobian

---

INPUTS: The length  $n$  of the vector and the size of the perturbation step  $\epsilon$ . Depending on the Jacobian to be computed, the corresponding function  $\mathbf{F}(\boldsymbol{\chi}) = \mathbf{f}(\boldsymbol{\chi}, \mathbf{u}_0)$  for obtaining  $J = A_i$  and  $\mathbf{F}(\boldsymbol{\chi}) = \mathbf{f}(\mathbf{x}_0, \boldsymbol{\chi})$  for acquiring  $J = B_i$

OUTPUTS: Numerically computed Jacobian  $J$ .

---

**Note:**

$\tilde{\boldsymbol{\chi}}$  = Perturbed vector

$\boldsymbol{\chi}_0$  = Original vector at equilibrium point

Set perturbed vector equal to the original vector:

$$\tilde{\boldsymbol{\chi}} = \boldsymbol{\chi}_0\tag{A-6}$$

**for**  $i=1:n$  **do**

$$\tilde{\boldsymbol{\chi}}(i) = \tilde{\boldsymbol{\chi}}(i) + \epsilon\tag{A-7a}$$

$$J(:, i) = \frac{\mathbf{F}(\tilde{\boldsymbol{\chi}}) - \mathbf{F}(\boldsymbol{\chi})}{\epsilon}\tag{A-7b}$$

$$\tilde{\boldsymbol{\chi}}(i) = \boldsymbol{\chi}_0(i)\tag{A-7c}$$

**end for**

---

### A-2-2 Trim point algorithm

To find the stable operating conditions for the latter linearization technique, a custom trim point algorithm is developed. This algorithm will be briefly introduced using the parameters and aerodynamic coefficients of the SB-10 glider. By decoupling the asymmetric and symmetric motions, this algorithm can easily be applied to the Diana-2 model.

To find the stable operating conditions or trim points at different airspeeds, a horizontal steady flight condition is assumed. At this flight condition the asymmetric rigid velocity states  $p$ ,  $q$ ,  $r$ , and modal velocity states  $\dot{\eta}_1$ ,  $\dot{\eta}_2$ ,  $\dot{\eta}_3$  are zero. Using this, a combination of  $\alpha$ ,  $\theta$ ,  $\eta_1$ ,  $\eta_2$ ,  $\eta_3$ ,  $\delta_e$  is found that results in a zero aerodynamic pitching moment and a constant aerodynamic force vector in opposite direction of the gravity force vector.

By assuming that the aerodynamic center is only displayed by a distance  $\Delta X_{cg}$  from the center of gravity, the following expression for the pitching moment coefficient is obtained:

$$C_M = C_{M_0} + C_{M_\alpha} + C_{M_{\eta_1}} + C_{M_{\eta_2}} + C_{M_{\eta_3}} - \frac{\Delta X_{cg}}{\bar{c}} (C_L \cos(\alpha_v) + C_D \sin(\alpha_v)) + C_{M_{\delta_e}} \delta_e + C_{M_{\delta_{fi}}} \delta_{fi} \quad (\text{A-8})$$

Using the small angle approximation of  $\cos(\alpha_v) \approx 1$  and  $\sin(\alpha_v) \approx \alpha$  it can be assumed that the term  $C_D \sin(\alpha_v) \approx 0$  as  $C_D \ll 1$ . This simplifies A-8 to  $C_M = -\frac{\Delta X_{cg}}{\bar{c}} C_L$ . By including the dynamics of the structural modes  $-\omega_{n_f}^2 \boldsymbol{\eta}$  inside the aerodynamic coefficient matrix and observing that the coefficients  $C_Q^{\eta_1}$ ,  $C_Q^{\eta_2}$  and  $C_Q^{\eta_3}$  has to be zero for  $\ddot{\eta} = 0$ , one can find  $\alpha_v$ ,  $\eta_1$ ,  $\eta_2$  and  $\eta_3$  by solving the following matrix equality:

$$\begin{bmatrix} \alpha \\ \eta_1 \\ \eta_2 \\ \eta_3 \end{bmatrix} = \begin{bmatrix} C_{M_\alpha} - C_{L_\alpha} \frac{\Delta X_{cg}}{\bar{c}} & C_{M_{\eta_1}} - C_{L_{\eta_1}} \frac{\Delta X_{cg}}{\bar{c}} & C_{M_{\eta_2}} - C_{L_{\eta_2}} \frac{\Delta X_{cg}}{\bar{c}} & C_{M_{\eta_3}} - C_{L_{\eta_3}} \frac{\Delta X_{cg}}{\bar{c}} \\ C_{\eta_1}^{\eta_1} & C_{\eta_1}^{\eta_1} - \frac{\mu_1 \omega_1^2}{\bar{q} S \bar{c}} & C_{\eta_2}^{\eta_1} & C_{\eta_3}^{\eta_1} \\ C_{\eta_2}^{\eta_2} & C_{\eta_1}^{\eta_2} & C_{\eta_2}^{\eta_2} - \frac{\mu_2 \omega_2^2}{\bar{q} S \bar{c}} & C_{\eta_3}^{\eta_2} \\ C_{\eta_3}^{\eta_3} & C_{\eta_1}^{\eta_3} & C_{\eta_2}^{\eta_3} & C_{\eta_3}^{\eta_3} - \frac{\mu_3 \omega_3^2}{\bar{q} S \bar{c}} \end{bmatrix}^{-1} \mathbf{v}_r \quad (\text{A-9})$$

Here, the vector  $\mathbf{v}_r$  contains the zero coefficients and the effect of the elevator and flap deflections:

$$\mathbf{v}_r = \begin{bmatrix} -C_{M_0} - C_{M_{\delta_e}} \delta_e - C_{M_{\delta_{fi}}} \delta_{fi} + \frac{\Delta X_{cg}}{\bar{c}^2} (C_{L_0} + C_{L_{\delta_e}} \delta_e + C_{L_{\delta_{fi}}} \delta_{fi}) \\ -C_{\delta_e}^{\eta_1} - C_{\delta_e}^{\eta_1} \delta_e - C_{\delta_{fi}}^{\eta_1} \delta_{fi} \\ -C_{\delta_e}^{\eta_2} - C_{\delta_e}^{\eta_2} \delta_e - C_{\delta_{fi}}^{\eta_2} \delta_{fi} \\ -C_{\delta_e}^{\eta_3} - C_{\delta_e}^{\eta_3} \delta_e - C_{\delta_{fi}}^{\eta_3} \delta_{fi} \end{bmatrix} \quad (\text{A-10})$$

Accordingly, the lift force in the stability reference frame is found through

$$L = \bar{q} S \underbrace{(C_{L_0} + C_{L_{\alpha_v}} \alpha_v + C_{L_{\eta_1}} \eta_1 + C_{L_{\eta_2}} \eta_2 + C_{L_{\eta_3}} \eta_3 + C_{L_{\delta_e}} \delta_e + C_{L_{\delta_f}} \delta_f)}_{C_L} \quad (\text{A-11})$$

The drag force is found by substituting the latter lift coefficient in the drag polar:

$$D = \bar{q} S \left( C_{D_0} + \frac{C_L^2}{\pi A_s e_o} + C_{D_{\delta_{fi}}} \delta_{fi} \right) \quad (\text{A-12})$$

Since the aircraft is gliding steadily, the following steady horizontal flight equations can be used to find the flight path angle  $\gamma$ .

$$\left. \begin{array}{l} L \cos(\gamma) + D \sin(\gamma) = mg \\ L \sin(\gamma) = D \cos(\gamma) \end{array} \right\} \gamma = -\tan^{-1} \left( \frac{D}{L} \right) \quad (\text{A-13})$$

Subsequently, the pitch angle is found through considering the  $\theta = \gamma + \alpha_v$  relation. For achieving this steady condition, a corresponding  $\delta_e$  is found that satisfies  $\sqrt{L^2 + D^2} = mg$ . By iteratively varying the elevator deflection  $\delta_e$ , a stable state condition is found that results in minimal a minimal error of  $\epsilon = \sqrt{L^2 + D^2} - mg$ .

## $\mathcal{H}_\infty$ algorithm and control design formulation with INDI-PCH

This appendix presents some additional background material for the control synthesis methods discussed in Section 4-2-2. First the  $\mathcal{H}_\infty$  optimization is discussed. Subsequently, the incorporation of Pseudo Control Hedging (PCH) in the design formulation of Section 4-2-2 will be presented.

### B-1 General $\mathcal{H}_\infty$ algorithm

For the general control configuration of Figure 2-1, described by 2-25 and 2-28, with assumptions (A1) to (A6), there exists a stabilizing controller  $K$ , that achieves an upper bound  $\gamma$  as an performance index, i.e.,  $\|\mathcal{F}_L(P, K)\|_\infty < \gamma$ , if and only if:

1.  $X_\infty \geq 0$  is a solution of the algebraic Riccati equation

$$A^T X_\infty + X_\infty A + C_1^T C_1 + X_\infty (\gamma^{-2} B_1 B_1^T - B_2 B_2^T) X_\infty = 0 \quad (\text{B-1})$$

such that  $\text{Re } \lambda_i [A + (-\gamma^2 B_1 B_1^T - B_2 B_2^T) X_\infty] < 0, \forall i$ ; and

2.  $Y_\infty \geq 0$  is a solution of the algebraic Riccati equation

$$A Y_\infty + Y_\infty A^T + B_1 B_1^T + Y_\infty (\gamma^{-2} C_1^T C_1 - C_2^T C_2) Y_\infty = 0 \quad (\text{B-2})$$

such that  $\text{Re } \lambda_i [A + (-\gamma^2 C_1 C_1^T - C_2 C_2^T) Y_\infty] < 0, \forall i$ ; and

3.  $\rho(X_\infty Y_\infty) < \gamma^2$

All such controllers are then given by  $K = \mathcal{F}_L(K_c, Q)$ , where

$$K_c(s) \stackrel{s}{=} \left[ \begin{array}{c|cc} A_\infty & -Z_\infty L_\infty & Z_\infty B_2 \\ \hline F_\infty & 0 & I \\ -C_2 & I & 0 \end{array} \right] \quad (\text{B-3})$$

$$\begin{aligned} F_\infty &= -B_2^T X_\infty, L_\infty = -Y_\infty C_2^T, Z_\infty = \left( I - \gamma^{-2} Y_\infty X_\infty \right)^{-1} \\ A_\infty &= A + \gamma^{-2} B_1 B_1^T X_\infty + B_2 F_\infty + Z_\infty L_\infty \end{aligned} \quad (\text{B-4})$$

and  $Q(s)$  is any stable proper transfer function such that  $\|Q\| \leq \gamma$ . For  $Q(s) = 0$ ,

$$K(s) = K_{c11}(s) = -F_\infty (sI - A_\infty)^{-1} Z_\infty L_\infty \quad (\text{B-5})$$

This is called the central controller and has the same number of states as the generalized plant  $P(s)$ . In practice, however, controllers have a predefined structure with a lower system order than the generalized plant. To still acquire a controller with a predefined structure through  $\mathcal{H}_\infty$ , additional constraints can be imposed on the controller using specialized non-smooth optimization techniques [38].

## B-2 Synthesis formulation for the INDI-PCH controller

This subsection will derive the inclusion of PCH in the already presented design synthesis formulation of Section 4-2-2. For this derivation, recall again the generalized interconnection illustrated by Figure B-1. Here, one should note that the transfer functions from the disturbance channels to the performance output channels are similar to the loop transfer functions presented by (4-31), (4-32) and (4-33). Only the de transfer functions from the manipulated inputs to the outputs  $\mathbf{v}_e$  and  $v_r$  are different. In addition to the INDI loop transfer func-

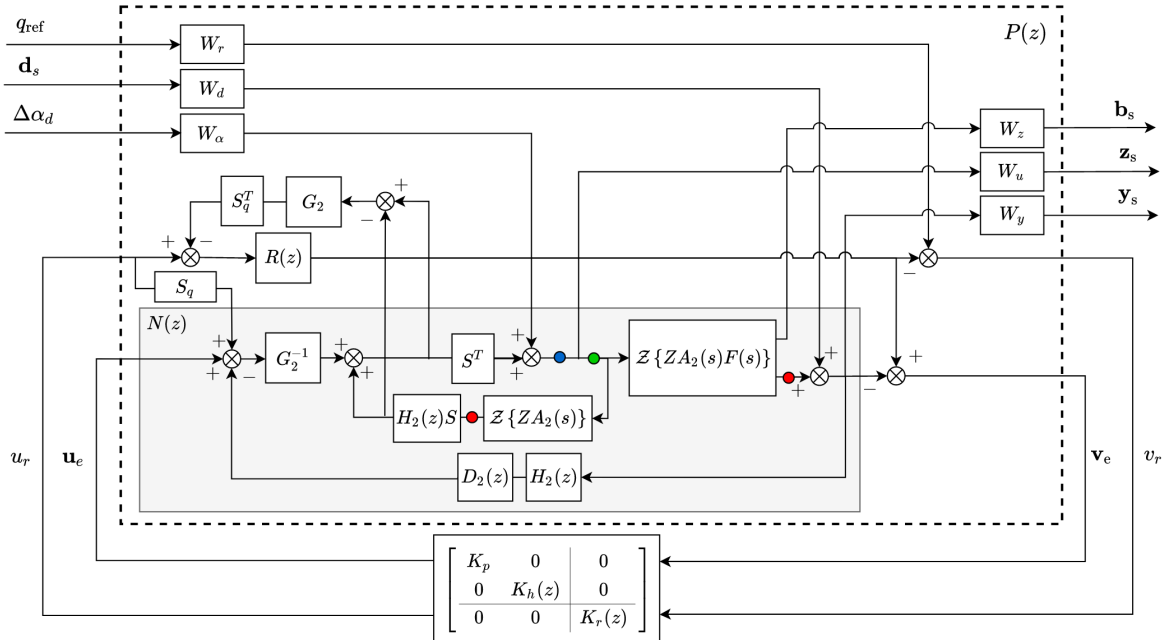


**Figure B-1:** Generalized interconnection for synthesising the linear controller  $K$ , for the INDI-PCH control structure, using a mixed sensitivity  $\mathcal{H}_\infty$ -norm minimization

tion  $N(z)$ , these transfer functions will be denoted by  $V(z)$ . Similar as in Section 4-2-2, the superscripts are indicating the output channel and the subscripts the input channels:

$$\begin{aligned}
V_{\mathbf{u}_e}^{v_r} &= R(z)S_q^T G_2(SA_L(z)G_2^{-1}(I + SA_L(z)G_2^{-1}D_2(z)H_2(z)\mathcal{Z}\{ZA_2(s)F_y(s)\})^{-1} - \\
&\quad SA_L(z)G_2^{-1}(I + SA_L(z)G_2^{-1}D_2(z)H_2(z)\mathcal{Z}\{ZA_2(s)F_y(s)\})^{-1}\mathcal{Z}\{ZA_2(s)\}SH_2(z)) \\
V_{u_r}^{v_r} &= R(z)(1 - S_q^T G_2(SA_L(z)G_2^{-1}(I + SA_L(z)G_2^{-1}D_2(z)H_2(z)\mathcal{Z}\{ZA_2(s)F_y(s)\})^{-1} - \\
&\quad SA_L(z)G_2^{-1}(I + SA_L(z)G_2^{-1}D_2(z)H_2(z)\mathcal{Z}\{ZA_2(s)F_y(s)\})^{-1}\mathcal{Z}\{ZA_2(s)\}SH_2(z))S_q) \\
V_{\alpha_d}^{v_r} &= R(z)S_q^T G_2((H_2S\mathcal{Z}\{ZA_2(s)\} - G_2^{-1}D_2(z)H_2(z)\mathcal{Z}\{ZA_2(s)F_y(s)\}) \\
&\quad \cdot (I - (H_2S\mathcal{Z}\{ZA_2(s)\} - G_2^{-1}D_2(z)H_2(z)\mathcal{Z}\{ZA_2(s)F_y(s)\})S^T)^{-1} \\
&\quad - H_2S\mathcal{Z}\{ZA_2(s)\}(I - H_2S\mathcal{Z}\{ZA_2(s)\}(S^T - S^T G_2^{-1}D_2(z)H_2(z)\mathcal{Z}\{ZA_2(s)F_y(s)\}))^{-1}) \\
V_{\mathbf{d}_s}^{v_r} &= R(z)S_q^T G_2(SA_L(z)G_2^{-1}D_2(z)H_2(z)(1 + SA_L(z)G_2^{-1}D_2(z)H_2(z)\mathcal{Z}\{ZA_2(s)F_y(s)\})^{-1} - \\
&\quad \mathcal{Z}\{ZA_2(s)\}H_2(z)SA_L(z)G_2^{-1}D_2(z)H_2(z)(1 + SA_L(z)G_2^{-1}D_2(z)H_2(z)\mathcal{Z}\{ZA_2(s)F_y(s)\})^{-1})
\end{aligned}$$

Here,  $S_q$  is chosen such that control hedging is only acting on the pitch rate and the measured elevator deflection:

$$S_q^T = \begin{bmatrix} 1 & 0 \end{bmatrix} \quad (\text{B-6})$$

By using latter transfer functions, the transfer functions to the output  $\mathbf{v}_e$  can also be found:

$$\begin{aligned}
V_{\mathbf{u}_e}^{\mathbf{v}_e} &= \mathcal{Z}\{ZA_2(s)F_y(s)\}A_L(z)G_2^{-1}(I + \mathcal{Z}\{ZA_2(s)F_y(s)\}A_L(z)G_2^{-1}D_2(z)H_2(z))^{-1} - V_{\mathbf{u}_e}^{v_r} \\
V_{u_r}^{\mathbf{v}_e} &= \mathcal{Z}\{ZA_2(s)F_y(s)\}A_L(z)G_2^{-1}(I + \mathcal{Z}\{ZA_2(s)F_y(s)\}A_L(z)G_2^{-1}D_2(z)H_2(z))^{-1}S_q - V_{u_r}^{v_r} \\
V_{\alpha_d}^{\mathbf{v}_e} &= \mathcal{Z}\{ZA_2(s)F_y(s)\}(I + \mathcal{Z}\{ZA_2(s)F_y(s)\}A_L(z)G_2^{-1}D_2(z)H_2(z))^{-1} - V_{\alpha_d}^{v_r} \\
V_{\mathbf{d}_s}^{\mathbf{v}_e} &= (I + \mathcal{Z}\{ZA_2(s)F_y(s)\}A_L(z)G_2^{-1}D_2(z)H_2(z))^{-1} - V_{\mathbf{d}_s}^{v_r}
\end{aligned} \quad (\text{B-7})$$

Combining this with the transfer functions in (4-31), (4-32) and (4-33), yields to the following matrix multiplication for the generalized plant  $P(z)$ :

$$\begin{bmatrix} \mathbf{b}_e \\ \mathbf{z}_e \\ \mathbf{y}_e \\ \mathbf{v}_e \\ v_r \end{bmatrix} = \begin{bmatrix} W_u & & & & \\ & W_z & & & \\ & & W_y & & \\ & & & I & \\ & & & & 1 \end{bmatrix} \begin{bmatrix} 0 & N_{\mathbf{d}_s}^{\mathbf{b}_s}(z) & N_{\alpha_d}^{\mathbf{b}_s}(z) & N_u^{\mathbf{b}_s}(z) & N_u^{\mathbf{b}_s}(z) \\ 0 & N_{\mathbf{d}_s}^{\mathbf{z}_s}(z) & N_{\alpha_d}^{\mathbf{z}_s}(z) & N_u^{\mathbf{z}_s}(z) & N_u^{\mathbf{z}_s}(z) \\ 0 & N_{\mathbf{d}_s}^{\mathbf{y}_s}(z) & N_{\alpha_d}^{\mathbf{y}_s}(z) & N_u^{\mathbf{y}_s}(z) & N_u^{\mathbf{y}_s}(z) \\ 0 & V_{\mathbf{d}_s}^{\mathbf{v}_e}(z) & V_{\alpha_d}^{\mathbf{v}_e}(z) & V_{u_e}^{\mathbf{v}_e}(z) & V_{u_r}^{\mathbf{v}_e}(z) \\ 1 & V_{\mathbf{d}_s}^{v_r}(z) & V_{\alpha_d}^{v_r}(z) & V_{u_e}^{v_r}(z) & V_{u_r}^{v_r}(z) \end{bmatrix} \begin{bmatrix} W_r & & & & \\ & W_d & & & \\ & & W_\alpha & & \\ & & & I & \\ & & & & 1 \end{bmatrix} \begin{bmatrix} q_{\text{ref}} \\ \mathbf{d}_s \\ \Delta\alpha_d \\ \mathbf{u}_e \\ u_r \end{bmatrix} \quad (\text{B-8})$$

Finally, as discussed in Section 4-2-2, the linear controller  $K$  can be obtained by utilizing (2-27) and (2-26).



---

## Appendix C

---

# Simulated tracking and structural motion alleviation results

This appendix shows the simulated responses of the PID, INDI and  $\mathcal{H}_\infty$  controllers subjected to the conditions described in Section 5-1-2.

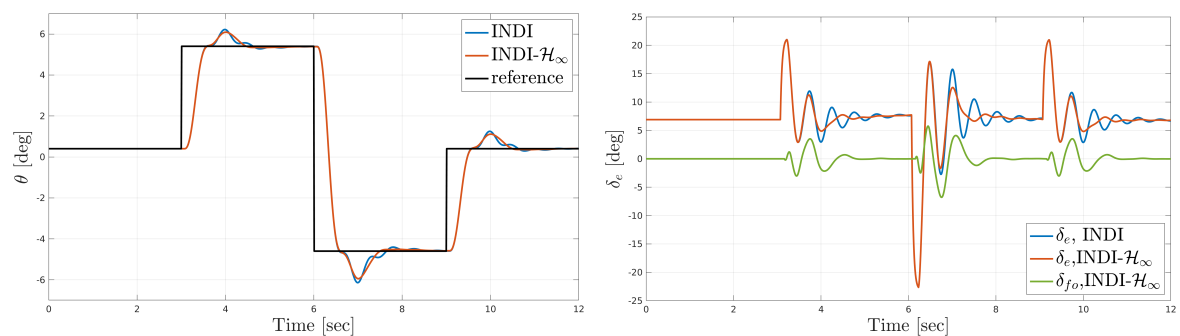


**Figure C-1:** Pitch angle response with corresponding control surface deflections of the INDI and INDI- $\mathcal{H}_\infty$  controller.

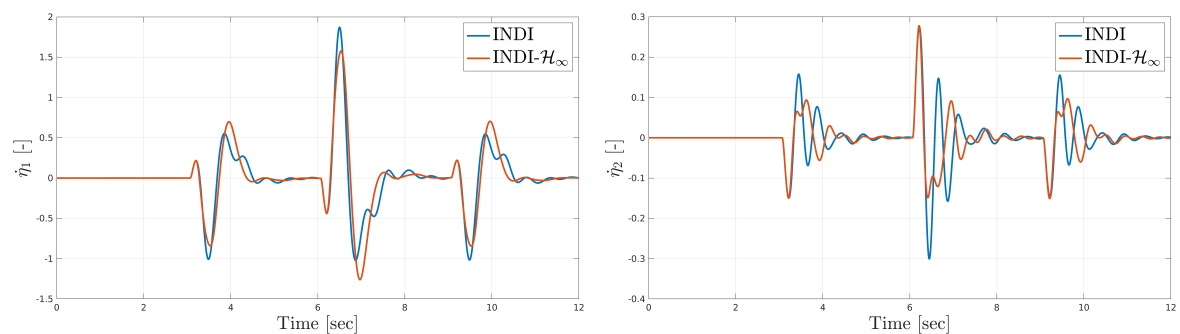


**Figure C-2:** Structural motion response, depicted by the first and second modal velocities, of the INDI and INDI- $\mathcal{H}_\infty$  controller

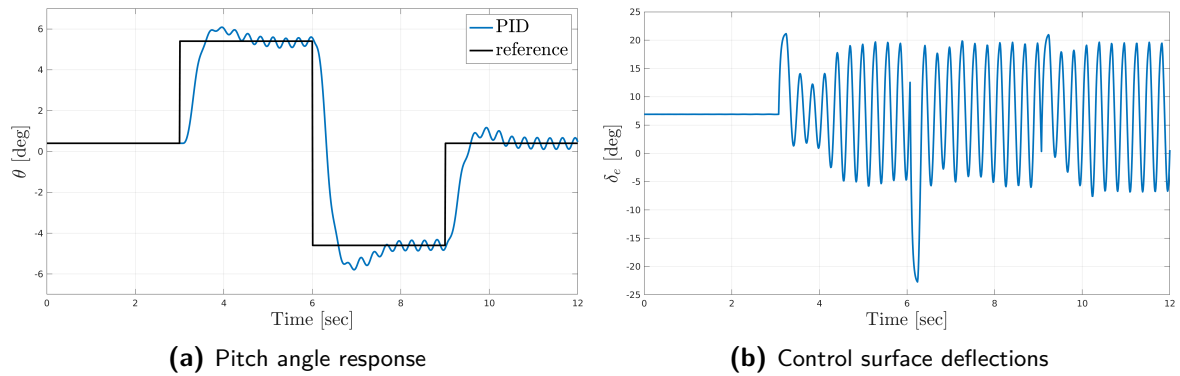


**Figure C-3:** Pitch angle response with corresponding control surface deflections of the baseline PID controller.

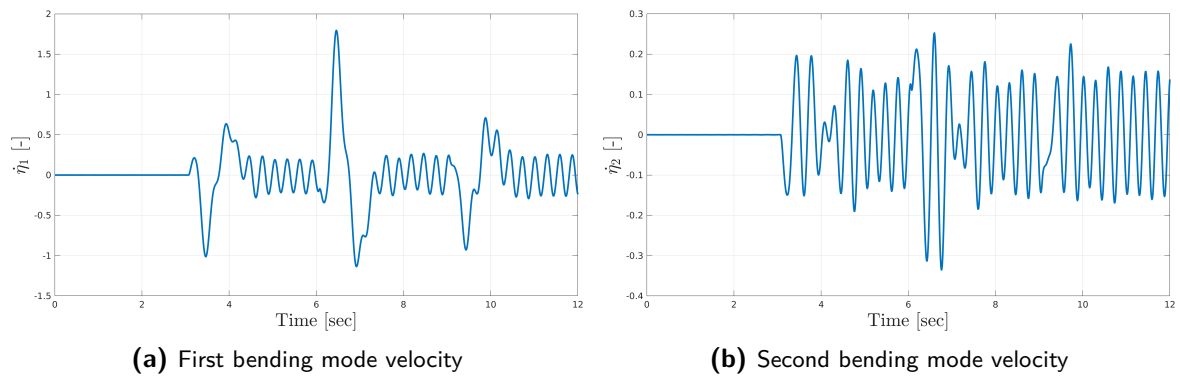


**Figure C-4:** Structural motion response, depicted by the first and second modal velocities, of the baseline PID controller

---

## Appendix D

---

# Actuator dynamics and time delay identification

To identify the time delays between the additional sensor messages and the Pixhawk, the received sensor messages on the Teensy, the Raspberry PI and Pixhawk are given an individual time-stamp. By evaluating the difference between the timestamps on each computing unit, the time delays proposed in Section 5-1-2 can be identified. First, the identification of the actuator model with corresponding time delays will be discussed. Thereafter the identification of the time delays on the additional sensor messages is investigated.

### D-0-1 Actuator identification

As already stated in Section 3-3-2, the second-order actuator models are identified using an input signal that contains three pulses and a chirp signal, at 20 % of the maximum PWM values. The measured and simulated response of these input signals is for the left outboard aileron illustrated in Figure D-1. Note that the measured inputs and outputs are logged on

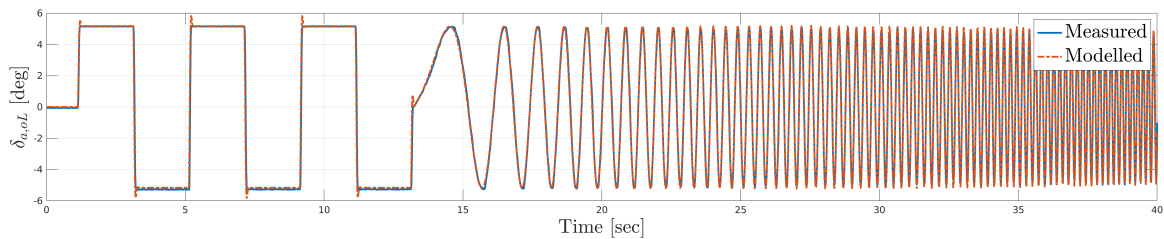


**Figure D-1:** The resulting fit of the identified second-order actuator model for the left outer aileron. Here, the measured control surface deflection is indicated in blue while the modelled response is marked in red.

the Raspberry PI and that they are synchronized to remove the effect of time delays in the system identification procedure. The resulting actuator bandwidth and damping is presented

**Table D-1:** Identified second-order actuator dynamics of the control surfaces installed on the Diana-2 demonstrator

	$\delta_{a_oL}$	$\delta_{a_mL}$	$\delta_{a_iL}$	$\delta_{a_oR}$	$\delta_{a_mR}$	$\delta_{a_iR}$	$\delta_r$	$\delta_e$
$\omega_a$ [rad/s]	56.46	51.85	49.75	59.56	52.58	55.88	32.81	34.83
$\zeta$ [-]	0.65	0.69	0.73	0.63	0.71	0.64	0.88	0.99
Model fit [%]	88.45	88.34	90.14	89.11	90.83	85.94	88.95	89.1

in Table D-1. Although the second-order actuator model can simulate the control surface deflections at higher frequencies quite well, a little overshoot can be seen at the sharp doublet responses in Figure D-1. To eliminate this overshoot, a first-order actuator model with rate limits can be considered instead:

$$\dot{\delta}(t) = S_R\{-\omega_a\delta(t) + \omega_a u(t)\} \quad (\text{D-1})$$

With  $S_R$  being a saturation function with rate limits  $R$

$$S_R(x) = \begin{cases} R & \text{if } x > M \\ x & \text{if } |x| \leq M \\ -R & \text{if } x < -M \end{cases} \quad (\text{D-2})$$

## D-0-2 Time delay identification

For the identification of the time delays, the different hardware components are often mentioned. Note that these components are discussed in Section 5-2-1 together with their interconnections and functionalities. The obtained measurement delay, process delay and transport delay, obtained in this subsection, solely provides representative reference considered time delays in Section 5-1-2.

### Measurement delay

Note that in the PX4 firmware, IMU sensor data is fed through the EKF to filter and synchronize the angular rate and attitude angles estimates. For the additional measurements that come from the data acquisition system on the Raspberry PI, this synchronization is not performed and corresponding time delays have to be identified. These time delays are referred to as measurement delays. To obtain an estimate of these time delays, the received sensor messages on the Teensy are given their own timestamp using ROS. This timestamp is then sent to the Raspberry PI and stamped with a new timestamp. By evaluating the difference between the two timestamps and adding half the round trip time between the Raspberry and the Pixhawk, a mean and standard deviation estimates of the measurement delay are obtained. These results are shown in Table D-3.

Note that these time delays are small and that the effect of not synchronizing these delays with the angular rates on the Pixhawk can be neglected. In addition, it should be noted that the data acquisition system on the Raspberry is not yet stable enough and that the implemented INDI controller on the Diana-2 does not rely on these measurements. Instead, the actuator feedback measurements are modelled inside the control loop using the identified actuator model and the estimated transport delay.

**Table D-2:** Identified (mean) time delays of the additional measurements with corresponding standard deviations

	$\delta_{a_oL}$	$\delta_{a_mL}$	$\delta_{a_iL}$	$\delta_{a_oR}$	$\delta_{a_mR}$	$\delta_{a_iR}$	$\delta_r$	$\delta_e$
$\mu_{\tau_p}$ [ms]	1.34	1.19	1.18	1.18	1.23	1.22	1.08	1.06
$\sigma_{\tau_p}$ [%]	0.013	0.017	0.018	0.018	0.015	0.016	0.020	0.019

### Transport delay

The transport delay can be computed by subtracting the measurement delay from the latency between sending the PWM signal and receiving the control surface deflection measurement. This latter time difference can be obtained by logging both signals on the same Pixhawk flight computer. Accordingly, by evaluating this time difference at the start of the 7 steps in the doublets of Figure D-1, the transport delays are obtained. These resulting time delays, for all the control surface deflection measurements, are presented in Table D-3. Note that the

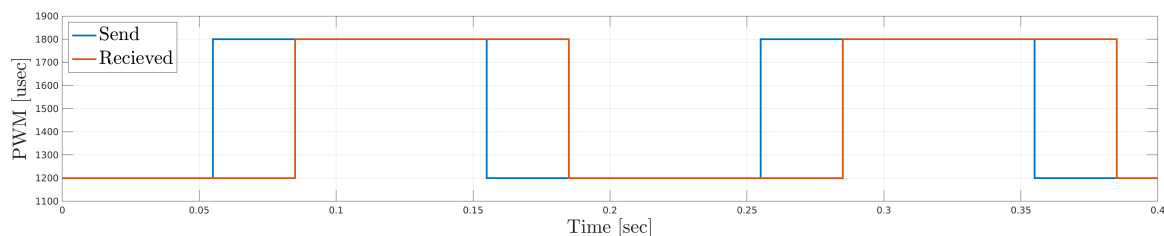
**Table D-3:** Identified time delays of the additional measurements with corresponding standard deviations (sampled at 50 Hz)

	$\delta_{a_oL}$	$\delta_{a_mL}$	$\delta_{a_iL}$	$\delta_{a_oR}$	$\delta_{a_mR}$	$\delta_{a_iR}$	$\delta_r$	$\delta_e$
$\mu_{\tau_p}$ [ms]	32.42	24.57	25.9	28.71	27.4	24.7	29.82	31.6
$\sigma_{\tau_p}$ [ms]	0.24	0.16	0.018	0.18	0.32	0.21	0.26	0.27

measurements are sampled at 50 Hz and that a smaller time delay is expected. As such, by subtracting the 20 ms sampling rate from the values in Table D-3, a more realistic estimate of the transport delay should be obtained. By increasing the sampling rate at which the Teensy microprocessors are sending their measurements and by increasing the sampling rate at which these are imported in the controller, this time delay can be reduced.

### Process delay

The process delay determination procedure is inspired from [5] and was tested in HIL by sending a square signal through the controller and receiving it back. The time shift between the two square signals shows the approximate time of processing the flight control algorithm. The delay measurement is illustrated in Figure D-2 and shows a time shift of 30 ms. Note that

**Figure D-2:** Process delay test using the HIL simulation. Blue line is the signal out, red line is the echoed signal from the Pixhawk

this process delay is only approximate as it also includes the delay of the simulation running

on the computer. Nevertheless, by considering the 10 ms sampling time of the controller, one can state that the process delay is close to 20 ms.

---

# Bibliography

- [1] J. Theis, “Robust and Linear Parameter-Varying Control of Aeroservoelastic Systems,” *PhD’s Thesis, Technische Universität Hamburg*, no. January, 2018.
- [2] F. J. Silvestre and R. Luckner, “Experimental validation of a flight simulation model for slightly flexible aircraft,” *AIAA Journal*, vol. 53, no. 12, pp. 3620–3636, 2015.
- [3] F. Afonso, J. Vale, É. Oliveira, F. Lau, and A. Suleman, “A review on non-linear aeroelasticity of high aspect-ratio wings,” *Progress in Aerospace Sciences*, vol. 89, pp. 40–57, 2017.
- [4] A. Collar, “The first fifty years of aeroelasticity,” *Aerospace (Royal Aeronautical Society Journal)*, vol. 5, pp. 12–20, 1978.
- [5] B. Takarics, B. Patartics, T. Luspay, B. Vanek, C. Roessler, J. Bartasevicius, S. J. Koeberle, M. Hornung, D. Teubl, M. Pusch, M. Wustenhagen, T. M. Kier, G. Looye, P. Bauer, Y. M. Meddaikar, S. Waitman, and A. Marcos, “Active Flutter Mitigation Testing on the FLEXOP Demonstrator Aircraft,” no. January, 2020.
- [6] J. A. Grauer and M. Boucher, “System Identification of Flexible Aircraft: Lessons Learned from the X-56A Phase 1 Flight Tests,” *AIAA SciTech Forum*, pp. 1017–1043, 2020.
- [7] T. Luspay, T. Baár, D. Teubl, B. Vanek, D. Ossmann, M. Wüstenhagen, M. Pusch, T. Kier, S. Waitman, A. Iannelli, A. Marcos, and M. Lowenberg, “Flight control design for a highly flexible flutter demonstrator,” *AIAA Scitech Forum*, no. January, pp. 1817–1846, 2019.
- [8] S. Waitman and A. Marcos, “ $H_\infty$  control design for active flutter suppression of flexible-wing unmanned aerial vehicle demonstrator,” *Journal of Guidance, Control, and Dynamics*, vol. 43, no. 4, pp. 656–672, 2020.
- [9] X. K. Zheng, W. Tang, L. B. Wang, and B. Wang, “LPV control design for active flutter suppression,” *Zhendong Gongcheng Xuebao/Journal of Vibration Engineering*, vol. 31, no. 3, pp. 411–416, 2018.

- [10] C. Westermayer, A. Schirrer, M. Hemedi, and M. Kozek, “An  $\mathcal{H}_\infty$  full information approach for the feedforward controller design of a large blended wing body flexible aircraft,” *Progress in flight dynamics, guidance, navigation, control, fault detection, and avionics*, vol. 6, pp. 685–706, 2013.
- [11] R. G. Cook, R. Palacios, and P. Goulart, “Robust gust alleviation and stabilization of very flexible aircraft,” *AIAA Journal*, vol. 51, no. 2, pp. 330–340, 2013.
- [12] N. D. Tantaroudas, K. J. Badcock, A. Da.Ronch, and R. Palacios, “Model order reduction for control design of flexible free-flying aircraft,” *AIAA Atmospheric Flight Mechanics Conference*, no. January, pp. 1–25, 2015.
- [13] C. Weiser, D. Ossmann, R. O. Kuchar, R. Müller, D. M. Milz, and G. Looye, “Flight Testing a Linear Parameter Varying Control Law on a Passenger Aircraft,” *AIAA Scitech Forum*, pp. 1618–1632, 2020.
- [14] A. Hjartarson, P. J. Seiler, and G. J. Balas, “LPV Aeroservoelastic Control using the LPVTools Toolbox,” *AIAA Atmospheric Flight Mechanics (AFM) Conference*, pp. 4742–4767, 2013.
- [15] K. E. Hashemi, C.-g. Pak, and M. R. Akella, “Delta Adaptive Flexible Motion Control for the X-56A Aircraft,” *AIAA Atmospheric Flight Mechanics Conference*, no. June, pp. 2244–2260, 2015.
- [16] Z. Qu, A. Annaswamy, T. B. Company, and H. Beach, “An Adaptive Controller for Very Flexible Aircraft,” *AIAA Guidance, Navigation, and Control Conference*, pp. 4854–4865, 2013.
- [17] R. J. Caverly, A. R. Girard, I. V. Kolmanovsky, and J. R. Forbes, “Nonlinear Dynamic Inversion of a Flexible Aircraft,” *IFAC-PapersOnLine*, vol. 49, no. 17, pp. 338–342, 2016.
- [18] X. Wang, E. Van Kampen, Q. P. Chu, and R. De Breuker, “Flexible aircraft gust load alleviation with incremental nonlinear dynamic inversion,” *Journal of Guidance, Control, and Dynamics*, vol. 42, no. 7, pp. 1519–1536, 2019.
- [19] X. Wang, T. Mkhoyan, and R. de Breuker, “Nonlinear incremental control for flexible aircraft trajectory tracking and load alleviation,” *AIAA Scitech 2021 Forum*, pp. 1–19, 2021.
- [20] F. Grondman, G. H. Looye, R. O. Kuchar, Q. P. Chu, and E. J. van Kampen, “Design and flight testing of incremental nonlinear dynamic inversion based control laws for a passenger aircraft,” *AIAA Guidance, Navigation, and Control Conference, 2018*, pp. 385–409, 2018.
- [21] E. J. Smeur, Q. Chu, and G. C. De Croon, “Adaptive incremental nonlinear dynamic inversion for attitude control of micro air vehicles,” *Journal of Guidance, Control, and Dynamics*, vol. 39, no. 3, pp. 450–461, 2016.
- [22] W. Van Ekeren, G. Looye, R. Kuchar, Q. Chu, and E. J. Van Kampen, “Design, implementation and flight-test of incremental backstepping flight control laws,” *AIAA Guidance, Navigation, and Control Conference*, pp. 384–404, 2018.

- 
- [23] J.-J. E. Slotine, W. Li, *et al.*, *Applied nonlinear control*. No. 1, Prentice hall, Englewood Cliffs, NJ, 199 ed., 1991.
- [24] S. Sieberling, Q. P. Chu, and J. A. Mulder, “Robust flight control using incremental nonlinear dynamic inversion and angular acceleration prediction,” *Journal of Guidance, Control, and Dynamics*, vol. 33, no. 6, pp. 1732–1742, 2010.
- [25] P. Simplício, M. D. Pavel, E. van Kampen, and Q. P. Chu, “An acceleration measurements-based approach for helicopter nonlinear flight control using incremental nonlinear dynamic inversion,” *Control Engineering Practice*, vol. 21, no. 8, pp. 1065–1077, 2013.
- [26] T. J. Lombaerts, G. H. Looye, Q. P. Chu, and J. A. Mulder, “Pseudo control hedging and its application for safe flight envelope protection,” *AIAA Guidance, Navigation, and Control Conference*, pp. 8280–8296, 2010.
- [27] R. C. van’t Veld, E. Van Kampen, and Q. P. Chu, “Stability and robustness analysis and improvements for incremental nonlinear dynamic inversion control,” *AIAA Guidance, Navigation, and Control Conference*, pp. 1127–1144, 2018.
- [28] P. Acquatella, W. van Ekeren, and Q. P. Chu, “Pi(d) tuning for flight control systems via incremental nonlinear dynamic inversion,” *IFAC-PapersOnLine*, vol. 50, no. 1, pp. 8175–8180, 2017.
- [29] S. Skogestad and I. Postlethwaite, *Multivariable feedback control: analysis and design*. John Wiley & Sons, 2 ed., 2001.
- [30] E. Mooij, “Robust control of a conventional aeroelastic launch vehicle,” in *AIAA Scitech 2020 Forum*, pp. 1103–1128, 2020.
- [31] C. D. Heise, M. Leitão, and F. Holzapfel, “Performance and robustness metrics for adaptive flight control - Available approaches,” *AIAA Guidance, Navigation, and Control (GNC) Conference*, pp. 5090–5114.
- [32] Y. Wang, A. Wynn, and R. Palacios, “Nonlinear modal aeroservoelastic analysis framework for flexible aircraft,” *AIAA Journal*, vol. 54, no. 10, pp. 3075–3090, 2016.
- [33] M. R. Waszak and D. K. Schmidt, “Flight dynamics of aeroelastic vehicles,” *Journal of Aircraft*, vol. 25, no. 6, pp. 563–571, 1988.
- [34] B. G. de Oliveira Silva and W. Mönnich, “System identification of flexible aircraft in time domain,” *AIAA Atmospheric Flight Mechanics Conference*, pp. 4412–4438, 2012.
- [35] I. ZONA Technology, *ZAERO User’s Manual ZAERO User’s Manual*.
- [36] J. A. Grauer and M. J. Boucher, “Real-time parameter estimation for flexible aircraft,” *AIAA Atmospheric Flight Mechanics Conference*, pp. 3155–3180, 2018.
- [37] N. T. Nguyen, “Model-reference adaptive control: A primer,” in *Advanced Textbooks in Control and Signal Processing*. Springer International Publishing, Springer, 2018.
- [38] P. Apkarian and D. Noll, “Erratum to " nonsmooth  $h_\infty$  synthesis",” *IEEE Transactions on Automatic Control*, vol. 51, no. 2, pp. 382–382, 2006.

- 
- [39] P. Apkarian, P. Gahinet, and C. Buhr, “Multi-model, multi-objective tuning of fixed-structure controllers,” in *2014 European Control Conference (ECC)*, no. June, pp. 856–861, 2014.
- [40] D. K. Schmidt, “MATLAB-based flight-dynamics and flutter modeling of a flexible flying-wing research drone,” *Journal of Aircraft*, vol. 53, no. 4, pp. 1045–1055, 2016.

---

# Glossary

## List of Acronyms

<b>HALE</b>	High Altitude Long Endurance
<b>UAS</b>	Unmanned Aerial Systems
<b>NLR</b>	Netherlands Aerospace Centre
<b>PID</b>	Proportional-Integral-Derivative
<b>LPV</b>	Linear Parameter Varying
<b>MRAC</b>	Model Reference Adaptive Control
<b>MIMO</b>	Multi-Input-Multi-Output
<b>NDI</b>	Nonlinear Dynamic Inversion
<b>FBL</b>	Feedback Linearization
<b>INDI</b>	Incremental Nonlinear Dynamic Inversion
<b>UAV</b>	Unmanned Aerial Vehicle
<b>HIL</b>	Hardware-in-the-loop
<b>MOPS</b>	Multi Objective Parameter Optimization
<b>PCH</b>	Pseudo Control Hedging
<b>RMS</b>	Root Mean Square
<b>CMSD</b>	Cumulative Moving Standard Deviation
<b>TDM</b>	Time Delay Margin
<b>NED</b>	North East Down
<b>IMU</b>	Inertial Measurement Unit
<b>ICA</b>	Incremental Control Allocation
<b>AICA</b>	Adaptive Incremental Control Allocation
<b>BC</b>	Best-case
<b>MC</b>	Mid-case
<b>WC</b>	Worst-case
<b>GPS</b>	Global Positioning System
<b>ROS</b>	Robotic Operating System
<b>EKF</b>	Extended Kalman Filter
<b>API</b>	Application Programming Interface
<b>PWM</b>	Pulse-width modulation
<b>RC</b>	Remote Control

## List of Symbols

$\alpha$	Angle of attack
$\beta$	Sideslip angle
$\delta_a$	Aileron angle
$\delta_e$	Elevator angle
$\delta_f$	Flap angle
$\delta_r$	Rudder angle
$\Delta$	Incremental time step
$\nabla$	Gradient or Jacobian
$\nu$	Virtual input
$\epsilon$	Strain
$\gamma$	Flight path angle
$\phi$	Roll angle around x-axis
$\omega$	Angular rate
$\rho$	Air density
$\theta$	Pitch angle around y-axis
$\phi$	Roll angle around x-axis
$\psi$	Yaw angle around z-axis
$\tau$	Time delay or time constant
$\omega_a$	Actuator bandwidth
$\omega_f$	Filter bandwidth
$\omega_i$	Natural frequency of the $i$ -th structural mode
$\xi_i$	Damping ratio of the $i$ -th structural mode
$\eta_i$	Modal amplitude of the $i$ -th structural mode
$\Phi$	Modeshape
$\mu$	Modal mass
$\mathcal{X}$	Course angle
$\bar{c}$	Mean chord
$\bar{q}$	Dynamic pressure
$\mathcal{O}$	Reference frame origin
$\mathbb{T}$	Transformation matrix
$\mathcal{Z}$	Zero order hold notation
$A$	State space matrix
$A(\cdot)$	Actuator dynamics
$A_s$	Aspect ratio
$A_M$	Coefficient matrix
$a$	Acceleration
$b$	Wing span
$B$	Input matrix

---

$B_0$	Control effectiveness
$C_D$	Non-dimensional drag coefficient
$C_L$	Non-dimensional lift coefficient
$C_Y$	Non-dimensional lift coefficient
$C_{\mathcal{L}}$	Non-dimensional pitch moment coefficient
$C_{\mathcal{M}}$	Non-dimensional pitch moment coefficient
$C_{\mathcal{N}}$	Non-dimensional yaw moment coefficient
$D$	Drag force
$d_s$	Disturbance channel
$D(\cdot)$	Discrete-time derivative operator
$e_o$	Oswald factor
$e_{ac}$	Distance between elastic axis and aerodynamic centre
$f$	State dynamics
$F$	Aerodynamic forces
$F(\cdot)$	Linear state dynamics
$g$	Gravitational constant
$G_s$	Scaling matrix
$h$	Output dynamics
$H(\cdot)$	Filter dynamics
$I$	Identity matrix of moment of inertia
$i_s$	Incidence angle
$J$	Moment of inertia matrix
$k$	Sampling instance
$K(\cdot)$	State space controller
$K$	Gain
$L$	Lift force
$\mathcal{L}$	Rolling moment
$L_f h$	Lie derivative
$\mathcal{M}$	Pitching moment
$m$	Mass of aircraft
$m$	Number of outputs
$N$	Loop transfer functions
$\mathcal{N}$	Yawing moment
$n$	Number of states
$O$	Origin
$P$	Generalized plant
$p$	Roll rate
$P_d$	Linear displacement
$q$	Pitch rate
$Q$	Generalized load
$r$	Yaw rate
$r^d$	Relative degree
$R(\cdot)$	Reference model
$S$	Scaling matrix

---

$S$	Wing area
$s$	Laplace transform variable
$T_s$	Sampling time
$u$	Control input
$u$	Velocity body x-axis
$v$	Velocity body y-axis
$W$	Control preference weighting matrix
$w$	Exogenous input
$X$	Force in x-axis
$x$	State or control variable
$Y$	Force in y-axis
$y$	Measured output variable
$Z$	Force in z-axis
$z$	Exogenous performance outputs
$z$	Transformed discrete state